Chapter 7

Quantum Nuclear Effects

In Chapter 5, we have introduced the principles underlying standard MD simulations nowadays. It was clearly pointed out in the introduction that to be pediatric the nuclei are treated as classical point-like particles in that chapter. This classical treatment of the nuclei is normally a good approximation since the nuclear masses are much larger than that of the electron. However, it needs to be pointed out that these values are still far from being large enough so that the classical treatment is rigorous, especially for the lightest element hydrogen, where it is only ∼1836 times of that of the electron. The quantum nuclear effects (QNEs) still might be important in reality. As a matter of fact, it has long been realized that the statistical properties of hydrogen-bonded systems such as water heavily depend on the isotope of hydrogen. Taking the melting/boiling temperature of normal water (composed by H_2O) and heavy water (composed by D_2O) as an example, this value in heavy water is ∼3.8°C/1.4°C higher than that of the normal water under the ambient pressure. In statistical mechanics, it is well-known that the classical thermal effects of different isotopes are rigorously the same at the same temperature. Therefore, the difference between this statistical property in these two materials must originate from the QNEs.

Another example where the quantum feature of the nuclei plays an important role resides on studies of proton tunneling, which has been well-characterized in both hydrogen diffusion on metal surface [314, 315] and proton-transfer in biosystems [316]. The phenomena in the latter system have an important influence on enzyme catalysis [316, 317, 318]. In order to be able to account for such QNEs at the atomic level in the simulations, it is highly desired that one can have a scheme in statistical mechanics where in addition to the thermal effects, the QNEs can be equally addressed. As a matter of fact, due to the development of the path-integral representation of the quantum mechanics starting from the late 1940s, the foundation of such a scheme has been rigorously and systematically presented by R. P. Feynman and A. R. Hibbs in Ref. [67]. Based on this foundation, the MD simu-

lation technique as introduced in Chapter 5 was combined with the framework of this path-integral representation of the statistical mechanics and a series of path-integral molecular dynamics (PIMD) simulations had been performed in the 1980s (see e.g. Chandler and Wolynes' work in Ref. [68], Parrinello and Rahman's work in Ref. [69], or Berne and Thirumalai's work in Ref. [74]). Parallel to these PIMD simulations, the Monte-Carlo (MC) sampling technique was also used and properties of liquid helium including its superfluidity were systematically studied using this path-integral Monte-Carlo (PIMC) method (see e.g. Ceperley and Pollock's work in Refs. [70, 71, 72, 73]). In these PIMD/PIMC simulations, the QNEs are addressed on the same footing as the thermal ones when the statistical properties of the system to be simulated is evaluated, as will be explained in detail soon in this chapter. Therefore, when comparing their results with the ones when the nuclei are treated as classical particles, such as the MD simulation method we have introduced in Chapter 5, the differences account for the impact of the QNEs on the statistical properties in a very clean manner.

This comparison sets up a rigorous framework for the QNEs to be analyzed, which is still used nowadays. However, it needs to be pointed out that in both these early PIMD and PIMC simulations the empirical potentials were used to account for the inter-atomic interactions in the simulation. These potentials are simple and very good on describing the statistical property of many solids and liquids. However, they can easily fail when chemical reaction happens, due to a serious reconstruction of the electronic structures, which needs to be addressed "on the fly" as the dynamics of the system evolves. To address problems like this, where the impact of the QNEs is often more interesting, people started trying a combination between the PIMD/PIMC simulation technique with the *ab initio* method for the description of the electronic structures after the 1990s, first within the framework of Car-Parrinello (CP) MD (see e.g. Tuckerman, Marx, and Parrinello's work in Refs. [319, 320, 321]) and then directly on the Born-Oppenheimer (BO) MD or MC schemes [282, 286, 322, 323]. These methods really allow the bond making and bond breaking events to happen, as well as the thermal and quantum nuclear effects to be accounted for in a seamless manner based on the forces computed "on the fly" as the dynamics of the system evolves. Now, it is fair to say that they have come to such a mature stage that not only different functionals with the density functional theory can be used in descriptions of the electronic structures (see e.g. Morales, McMahon, Pierleoni, and Ceperley's work in Refs. [324, 325]), but also traditional quantum chemistry methods such as the MP2 method can be used (see e.g. Tachikawa and Shiga's work in Ref. [326] or Kaczmarek, Shiga, and Marx's work in Ref. [327]). With these choices of the electronic structures, when the inter-atomic interactions are accurate enough and the sampling over the high dimensional phase space is complete (ergodicity is satisfied in the language of statistics), one can safely rely on results obtained from such simulations, even under low temperatures

when the classical description of the nuclei fails. Therefore, on the statistical level, a scheme in which the thermal and quantum nuclear effects are accounted for on the same footing in the atomic simulations is already there. The only thing we need to take care on using it is the choice of the electronic structures for the description of the inter-atomic interactions and the ergodicity issue in the PIMD/PIMC sampling (which, however, is non-trivial at all).

Besides these statistical properties, another kind of the properties where the QNEs may also play an important role resides on the dynamics, especially when the chemical reaction rate is evaluated. This chemical reaction rate is a key parameter in chemistry and very hard to be simulated rigorously. One theory underlying descriptions of this quantity is the so-called transition state theory (TST) [328, 329, 330, 331]. Since the probability of finding the system close to the transition state is much smaller than that of the reactant or product state, this theory is intrinsically both statistical and dynamical. The term statistical means that this chemical reaction rate is proportional to the ratio of the equilibrium density of the system at the transition state to its value at the reaction state, which is a statistical property. While the term dynamical indicates that since the transition state is defined by a dividing surface separating the reaction and product states, after the system at the transition state falls into either the reactant or the product region, it stays at this state for a time long energy than it spends at the transition state. Therefore, what happens dynamically at the transition state is of crucial importance to its behavior in the future and theories underlying descriptions of such processes should be dynamical. Following the principles of scientific research, *i.e.* from the easy and idealized models to the more difficult and realistic ones, the earliest methods within the TST usually assumes a classical treatment of the nuclei. Later, when events like quantum tunneling were found to be crucial on describing the chemical reaction behaviors, a quantum version of the transition state theory was also proposed. This development is also associated with development of the purely statistical PIMD method to the dynamical regime. Two of the most often used schemes in descriptions of this dynamics within the scheme of path-integral molecular dynamics are the centroid molecular dynamics (CMD) and the ring-polymer molecular dynamics (RPMD). This extension of the statistical PIMD method to the dynamical regime will also be discussed.

In chapter 6, a scheme in which the free-energy with anharmonic contributions from the nuclei is calculated using the sampling method of MD was introduced. In our discussions there, the assumption that the nuclei are classical particles results in the fact that although the anharmonic contribution from the thermal fluctuations of the nuclei are accounted for in the thermodynamic integrations with MD sampling, the anharmonic effect associated with the quantum feature of the nuclei are completely neglected. This anharmonic contribution originating from the QNEs is often believed to be unimportant at moderate and high temperatures. However, when the

mass of the particle is small, this assumption might fail, starting from the moderate temperature regime to low temperatures. As a matter of fact, this anharmonic correction is recently found to be very important in describing the phase diagram of hydrogen and neon (see e.g. Ramírez, Herrero, Antonelli, Hernández's work in Ref. [332] or Habershon and Manolopoulos' work in Ref. [333]). Therefore, from both the methodology and the practical simulation's point of view, it is highly desired that a scheme in which the thermodynamic integration is combined with the *ab initio* PIMD method to address such problems. This treatment of the anharmonic quantum nuclear correction to the free-energy will also be discussed [333].

The chapter is organized as follows. In Sec. 7.1, we introduce the PIMD and related methods for statistics, where it is rigorously justified. Then, some extensions beyond these statistical studies will be briefly discussed in Sec. 7.2. After these, an introduction to how this PIMD method is combined the thermodynamic integration method for the calculation of the free-energy will be presented in Sec. 7.3. We end this chapter with some examples in Sec. 7.4 and a brief summary of the book in Sec. 7.5.

7.1 Path-Integral Molecular Simulations

7.1.1 Path-Integral Representation of the Propagator

For a theoretical description of the QNEs, it is crucial to start our discussions from their origin, *i.e.* the intrinsic quantum nature of the nuclei. The development of quantum mechanics in the last century tells us that the fundamental difference between the classical world and the quantum world lies on the point that in the quantum world things must be described in terms of "probability". In understanding this principle, we can make use of a scene maybe many of us have experienced during our primary school time. At least in the authors', we both remember that when a naughty boy is making a big noise during the class which irritates his teacher, this teacher will throw the tail of a chalk he is holding toward this guy to remind him being quiet. In most cases, it works. In the language of the classical/quantum mechanics, we would like to say that it works because the tail of this chalk is heavy enough so that it behaves as a classical particle. And the classical particles move according to their trajectories. Therefore, as long as you control the trajectory, you control the consequence.

Now mentally imagine that this chalk is a particle small enough so that its quantum feature is important in descriptions of the phenomena related to it, what happens after the chalk is thrown out will then be completely out of control due to

the principle of quantum mechanics. Every people in the classroom might be hit at a later time. From our textbook of the quantum mechanics, we know that in order to quantitatively describe behaviors like this, a propagator needs to be used. This propagator is a function of two events, with each event representing something happening at a certain time and a certain position. Still taking the classroom with a naughty boy and his teacher as an example, we can label the event when the teacher throw the tail of a chalk on the stage (position labeled as $\mathbf{x}_a$) at a certain time t_a as event a, while the event when "someone" got hit by the chalk at his/her position (labeled as $\mathbf{x}_b$) at a later time t_b as event b.

If we forget about the person who did this and only focus on the particle, these two events can be rephrased as: "the generation of a particle (tail of the chalk) at a and the annihilation of this particle at b". As mentioned in Chapter 4, in a many-body quantum entity, the correlation between these two events should be described using the propagator, which is also known as the Green's function. After event a happens, the probability of event b happening equals the square of the propagator's absolute value. In the Schrödinger representation of the quantum mechanics, this propagator is written as:

$$G\left(\mathbf{x}_b, t_b; \mathbf{x}_a, t_a\right) = \sum_j \psi_j(\mathbf{x}_b)\psi_j^*(\mathbf{x}_a)e^{(-i/\hbar)E_j(t_b-t_a)}, \tag{7.1}$$

where j runs over all eigenstates of the quantum system. This equation indicates that if one knows the eigenstate wave-functions and eigenvalues of this quantum system, this propagator can be expressed analytically and consequently the correlation between any two events is accurately described. However, it is well-known that the many-body Schrödinger equation is difficult to solve and it has a notorious scaling problem. Nowadays, many studies on the QNEs still resort to such a recipe, where the high-dimensional *ab initio* potential energy surfaces (PESs) are mapped out first and then the Schrödinger equation is solved directly [59, 60, 61, 62]. This method is rigorous because not only nuclear exchange, but also real-time propagation can be described rigorously in this framework [60]. But due to the scaling problem associated with both mapping the *ab initio* high-dimensional PESs and solving the Schrödinger equation, its application is seriously limited to systems less than ∼6 atoms. When the system gets bigger, a practical scheme for descriptions of this quantity must be used.

Thanks to the development of the path-integral representation of the quantum mechanics starting from the late 1940s by R. P. Feynman [63, 64, 65, 66, 67], a framework where this propagator is calculated using a manner we would like to use in this chapter was systematically presented by R. P. Feynman and A. R. Hibbs in their seminal book in 1965 (Ref. [67]). In this book, it was clearly explained that this propagator can be calculated not only from Eq. 7.1, but also in terms of a numerical path-integral, in which contributions from all paths in between events

a and b are taken into account. The trick is to divide the time interval between these two events, *i.e.* $t_b - t_a$, into P slides. Draw a line between t_a and t_b which intersects with t_i on $\mathbf{x}_i$. Then, on each time slide t_i, move the spatial coordinates $\mathbf{x}_i$ through the whole Cartesian space. When P equals infinity, all paths in between these two events will be taken into account. The propagator is calculated by adding contributions from all these paths into one quantity, through:

$$G\left(\mathbf{x}_b, t_b; \mathbf{x}_a, t_a\right) = \lim_{P\to\infty} \frac{1}{A} \int_V \int_V \cdots \int_V e^{(i/\hbar)S[b,a]} \frac{d\mathbf{x}_1}{A} \frac{d\mathbf{x}_2}{A} \cdots \frac{d\mathbf{x}_{P-1}}{A}. \tag{7.2}$$

Here, A is a re-normalization factor which equals $(2\pi i\hbar(t_b - t_a)/(Pm))^{\frac{1}{2}}$. $S[b,a]$ is the action of the path linking events a and b, defined by the spatial coordinates $\mathbf{x}_1$, $\mathbf{x}_2$, $\cdots$, and $\mathbf{x}_{P-1}$ on t_1, t_2, $\cdots$, t_{P-1}. For one specific path, as shown in Eq. 7.2, its contribution to the propagator is determined by the action of this path, which is calculated from:

$$S[b,a] = \int_{t_a}^{t_b} L(\dot{\mathbf{x}}, \mathbf{x}, t) dt. \tag{7.3}$$

To be more precise, taking the choice of path $\mathbf{x}_1$, $\mathbf{x}_2$, $\cdots$, $\mathbf{x}_{P-1}$ happening at times t_1, t_2, $\cdots$, t_{P-1}, as an example, the action of this path as defined by Eq. 7.3 can be written as:

$$\begin{aligned} S[b,a] = & \left[\frac{m}{2}\left(\frac{\mathbf{x}_1 - \mathbf{x}_a}{t_1 - t_a}\right)^2 - \frac{1}{2}\left(V(\mathbf{x}_1) + V(\mathbf{x}_a)\right)\right](t_1 - t_a) \\ & + \sum_{i=2}^{P-1}\left[\frac{m}{2}\left(\frac{\mathbf{x}_i - \mathbf{x}_{i-1}}{t_i - t_{i-1}}\right)^2 - \frac{1}{2}\left(V(\mathbf{x}_i) + V(\mathbf{x}_{i-1})\right)\right](t_i - t_{i-1}) \\ & + \left[\frac{m}{2}\left(\frac{\mathbf{x}_b - \mathbf{x}_{P-1}}{t_b - t_{P-1}}\right)^2 - \frac{1}{2}\left(V(\mathbf{x}_b) + V(\mathbf{x}_{P-1})\right)\right](t_b - t_{P-1}). \end{aligned} \tag{7.4}$$

With this definition, it is clear that the integration in Eq. 7.2 can be calculated numerically through such a procedure, as shown in Fig. 7.1 for the one-dimensional (1D) case. In practice, a finite number of time intervals must be chosen, one often tests the convergence of the quantity to be calculated with respect to this number of slides, till a reasonable accuracy can be obtained.

With this, we hope that we have made our point clear. In the simplest sentence, for the same quantity, *i.e.* the propagator, we can obtain it by using either i) all eigenstate wave-functions of the quantum system, or ii) a sum over contributions from all paths in between the events to be investigated. The first option looks elegant but it is difficult to handle for large many-body systems. In cases when it is not feasible, the path integral approach provides a numerically simple alternative, which we will make use of in studies of QNEs to be discussed in the following sections.

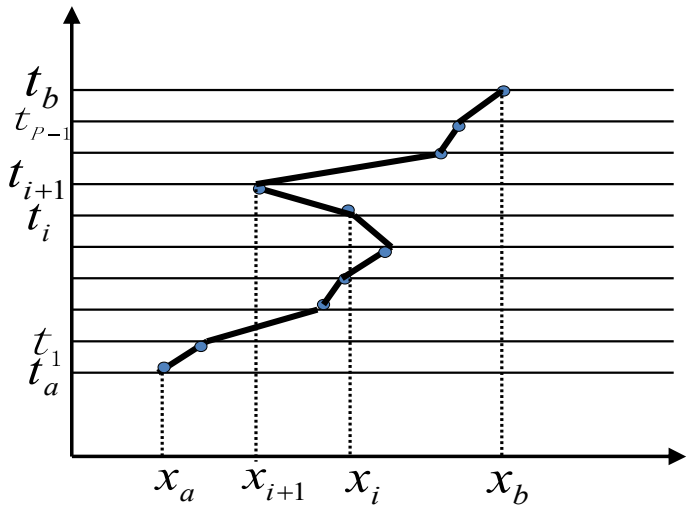

Figure 7.1: Illustration on how a propagator can be calculated using path-integral. The first step is to divide the time interval into some slides. At the starting and ending points (t_a and t_b), the spatial coordinates (x_a and x_b in this 1D case) must be fixed since they represent the events whose correlation is to be investigated. With the spatial coordinates on the time slices in between t_a and t_b chosen, we have one specific "path". Contribution from this path to the propagator is then calculated using Eq. 7.4. Then one further moves the spatial coordinates on each time slide in between t_a and t_b through the whole space (x axis in this 1D case). In so doing, we can take into account of contributions from all paths in between a and b. If all these contributions are calculated numerically using Eq. 7.4 and the time interval number approaches infinity, we have the propagator rigorously defined which equals the number it gives through Eq. 7.1. Calculations of the eigenstate wave-function are avoided accordingly.

7.1.2 Path-Integral Representation of the Density Matrix

So far about the propagator, in statistical mechanics, the key quantity we are interested in is actually not this propagator, but the density matrix. Therefore, in order to understand how the concept of the path-integral is used in studies on statistical mechanics, the key point is to understand how this quantity (density matrix) is expressed in terms of path-integral. As the basis, the first thing we explain here is how this key quantity is expressed in quantum mechanics in general.

Imagine that the quantum system we want to study has exact eigenstate wave-functions ψ_i, eigenvalues E_i, and a Hamiltonian $\hat{H}$. In the operator notation, the density operator is $e^{-\beta\hat{H}}$, where $\beta = 1/(k_{\mathrm{B}}T)$ and T is the temperature. The trace of this operator is the so-called partition function Z^{Q}. The expectation value of any

physical observable $\hat{O}$ equals:

$$\langle \hat{O} \rangle = (Z^{\mathrm{Q}})^{-1} \mathrm{Tr} \left[\hat{O} e^{-\beta \hat{H}} \right]. \tag{7.5}$$

Now we discuss how these quantities are represented in two spaces, *i.e.* the system's eigenstate wave-functions' Hilbert spaces and the position space. Such a comparison can help us to set up a link between the density matrix and the propagator we have discussed in Sec. 7.1.1, which you will see soon. We first look at the system's eigenstate wave-functions' Hilbert space, where the probability of finding the quantum system at its i^{th} eigenstate equals $e^{-\beta E_i}$ at thermal equilibrium. From this probability, it is clear that for an operator $\hat{O}$ its expectation value at the thermal equilibrium equals:

$$\langle \hat{O} \rangle = (Z^{\mathrm{Q}})^{-1} \sum_i \langle \psi_i | \hat{O} | \psi_i \rangle e^{-\beta E_i}. \tag{7.6}$$

The partition function Z^{Q} itself, has the simple form:

$$Z^{\mathrm{Q}} = \sum_i e^{-\beta E_i}. \tag{7.7}$$

Then we come to the position space. In this space, the density matrix is written as:

$$\rho(\mathbf{x}_a, \mathbf{x}_b, \beta) = \langle \mathbf{x}_b | e^{-\beta \hat{H}} | \mathbf{x}_a \rangle, \tag{7.8}$$

whose diagonal part is the so-called density function. To arrive at the wave-function based expression of this density matrix, one can insert an identity matrix $\hat{I} = \sum_j |\psi_j\rangle\langle\psi_j|$ into the right-hand side of this equation. In so doing, we have

$$\begin{aligned} \rho(\mathbf{x}_a, \mathbf{x}_b, \beta) &= \langle \mathbf{x}_b | e^{-\beta \hat{H}} (\sum_j |\psi_j\rangle\langle\psi_j|) | \mathbf{x}_a \rangle \\ &= \sum_j \langle \mathbf{x}_b | \psi_j \rangle e^{-\beta E_j} \langle \psi_j | \mathbf{x}_a \rangle \\ &= \sum_j \psi_j(\mathbf{x}_b) \psi_j^*(\mathbf{x}_a) e^{-\beta E_j}. \end{aligned} \tag{7.9}$$

Similar to the propagator, to obtain this quantity, in the Schrödinger representation of the quantum mechanics, we need to know the eigenstate wave-functions. However, as mentioned, calculating the wave-function of nuclei is not feasible for systems with more than ∼6 atoms. An alternative approach must be adopted.

Now we apply the concept of the path-integral as introduced in Sec. 7.1.1 to the description of this density matrix, the non-local function as shown in Eq. 7.9. The trick is to compare it with Eq. 7.1 for the propagator. From this comparison, it is easy to see that these two equations for the propagator and the density matrix share

very strong similarity. The only difference is that in Eq. 7.1 for the propagator, the index of the exponential function is imaginary and it is determined by the time interval $t_b - t_a$, while in Eq. 7.9 for the density matrix, the index of the exponential function is real and it is determined by the temperature T. In Sec. 7.1.1, we have shown that for the propagator in Eq. 7.1, we can avoid using the wave-functions by resorting to integrations over paths between the events to be described. Similarly, with this tiny difference between Eq. 7.9 and Eq. 7.1 in mind, we can also resort to the path-integral representation of the quantum mechanics and rewrite the density matrix as shown in Eq. 7.9 in terms of the path-integral. The only thing we need to do is to treat the temperature dependent factor β as an imaginary time interval and replace the $i(t_b - t_a)/\hbar$ term in Eq. 7.1 by this temperature dependent imaginary time interval. To be more precise, we should replace the time interval $t_b - t_a$ as used in Eq. 7.1 by $-i\hbar\beta$. Then, using the same trick as what we have mentioned for the numerical representation of the propagator in Eqs. 7.2, 7.3, and 7.4, we can rewrite the density matrix in terms of path-integral without resorting to the nuclear wave-functions.

Following this routine, the first thing we need to do is to divide the time interval $-i\hbar\beta$ into P slices. Such a treatment results in a time step of $-i\hbar\beta/P$ along the imaginary-time path to be integrated in the density matrix. Now, imagine that one path is defined by a certain choice of $\mathbf{x}_1, \mathbf{x}_2, \cdots, \mathbf{x}_{P-1}$ between $\mathbf{x}_a$ and $\mathbf{x}_b$, the action which determines the weight of this path in the path-integral scheme then equals:

$$\begin{aligned} S[b,a] = &- \left[\frac{mP^2}{2\beta^2\hbar^2}\left(\mathbf{x}_1 - \mathbf{x}_a\right)^2 + \frac{1}{2}\left(V(\mathbf{x}_1) + V(\mathbf{x}_a)\right)\right]\frac{-\hbar i\beta}{P} \\ &- \sum_{i=2}^{P-1}\left[\frac{mP^2}{2\beta^2\hbar^2}\left(\mathbf{x}_i - \mathbf{x}_{i-1}\right)^2 + \frac{1}{2}\left(V(\mathbf{x}_i) + V(\mathbf{x}_{i-1})\right)\right]\frac{-\hbar i\beta}{P} \\ &- \left[\frac{mP^2}{2\beta^2\hbar^2}\left(\mathbf{x}_b - \mathbf{x}_{P-1}\right)^2 + \frac{1}{2}\left(V(\mathbf{x}_b) + V(\mathbf{x}_{P-1})\right)\right]\frac{-\hbar i\beta}{P} \end{aligned} \tag{7.10}$$

from Eq. 7.4. We note that because imaginary time is used, the positive sign of the kinetic energy becomes negative, resulting in the action (which is originally defined as an integral over the Lagrangin) as a term above which looks like an integral over a minus Hamiltonian. The $(i/\hbar)S[b,a]$ term on the index of the exponential functional in Eq. 7.2 consequently becomes:

$$\begin{aligned} (i/\hbar)S[b,a] = &- \left[\frac{mP}{2\beta\hbar^2}\left(\mathbf{x}_1 - \mathbf{x}_a\right)^2 + \frac{\beta}{2P}\left(V(\mathbf{x}_1) + V(\mathbf{x}_a)\right)\right] \\ &- \sum_{i=2}^{P-1}\left[\frac{mP}{2\beta\hbar^2}\left(\mathbf{x}_i - \mathbf{x}_{i-1}\right)^2 + \frac{\beta}{2P}\left(V(\mathbf{x}_i) + V(\mathbf{x}_{i-1})\right)\right] \\ &- \left[\frac{mP}{2\beta\hbar^2}\left(\mathbf{x}_b - \mathbf{x}_{P-1}\right)^2 + \frac{\beta}{2P}\left(V(\mathbf{x}_b) + V(\mathbf{x}_{P-1})\right)\right]. \end{aligned} \tag{7.11}$$

To clean up a bit of the labelling in the above equations, we can relabel the $\mathbf{x}_a$ and $\mathbf{x}_b$ in the density matrix as $\mathbf{x}_0$ and $\mathbf{x}_P$ respectively. The imaginary time interval is still divided into P slices and the path is determined by a consequence of spatial coordinates from $\mathbf{x}_1$ to $\mathbf{x}_{P-1}$, with $\mathbf{x}_0$ and $\mathbf{x}_P$ keeping fixed. Then, Eq. 7.11 can be rewritten in a simple form as:

$$\begin{aligned}(i/\hbar)S[b,a] &= -\sum_{i=1}^{P}\left[\frac{mP}{2\beta\hbar^2}\left(\mathbf{x}_i-\mathbf{x}_{i-1}\right)^2+\frac{\beta}{2P}\left(V(\mathbf{x}_i)+V(\mathbf{x}_{i-1})\right)\right] \\ &= -\beta\sum_{i=1}^{P}\left[\frac{1}{2}m\omega_P^2\left(\mathbf{x}_i-\mathbf{x}_{i-1}\right)^2+\frac{1}{2P}\left(V(\mathbf{x}_i)+V(\mathbf{x}_{i-1})\right)\right],\end{aligned} \tag{7.12}$$

where $\omega_P=\sqrt{P}/(\beta\hbar)$. If we put this exponential index to the path-integral representation of propagator as shown in Eq. 7.2, but using the imaginary time for the density matrix, the equation this density matrix ends up with will be:

$$\begin{aligned}\rho\left(\mathbf{x}_0,\mathbf{x}_P,\beta\right)=\lim_{P\to\infty}\frac{1}{A}\int_V\int_V\cdots\int_V & e^{-\beta\sum_{i=1}^{P}\left[\frac{1}{2}m\omega_P^2(\mathbf{x}_i-\mathbf{x}_{i-1})^2+\frac{1}{2P}(V(\mathbf{x}_i)+V(\mathbf{x}_{i-1}))\right]} \\ & \frac{d\mathbf{x}_1}{A}\frac{d\mathbf{x}_2}{A}\cdots\frac{d\mathbf{x}_{P-1}}{A}.\end{aligned} \tag{7.13}$$

In the case of the real time propagator, we have mentioned that A is a re-normalization factor which equals $(2\pi i\hbar(t_b-t_a)/(Pm))^{\frac{1}{2}}$. Here, for the imaginary time density matrix, t_b-t_a should be replaced by $-i\hbar\beta$. Accordingly, A becomes $\left(2\pi\beta\hbar^2/(Pm)\right)^{1/2}$. Replacing the A in Eq. 7.13 with this value, we finally arrive at:

$$\begin{aligned}\rho\left(\mathbf{x}_0,\mathbf{x}_P,\beta\right)=\lim_{P\to\infty}\left(\frac{mP}{2\beta\pi\hbar^2}\right)^{\frac{P}{2}}&\int_V\int_V\cdots\int_V \\ & e^{-\beta\sum_{i=1}^{P}\left[\frac{1}{2}m\omega_P^2(\mathbf{x}_i-\mathbf{x}_{i-1})^2+\frac{1}{2P}(V(\mathbf{x}_i)+V(\mathbf{x}_{i-1}))\right]}d\mathbf{x}_1d\mathbf{x}_2\cdots d\mathbf{x}_{P-1}.\end{aligned} \tag{7.14}$$

Till now, the numerical representation of the density matrix in terms of the path-integral is already clear. However, there is still a key concept whose physical meaning needs some further explanation. In the above discussions, the variables $\mathbf{x}_0$ to $\mathbf{x}_P$ are defined as points in the Cartesian space for the nucleus to be studied for simplicity. However, we note that they can also be used to represent a poly-atomic system's spatial configuration of the nuclei under investigation. Suppose that this poly-atomic system is a molecule containing N nuclei, this $\mathbf{x}_i$ is then a $3N$-dimensional vector, representing a spatial configuration of this molecule's nuclei. To understand this, one just need to imagine that the wave-functions as used in Eqs. 7.1 and 7.9 are many-body wave-functions of this N-nuclei system whose square magnitude represents the probability of finding the poly-atomic system at this specific spatial configuration.

Accordingly, the path from $\mathbf{x}_0$, through $\mathbf{x}_1, \cdots, \mathbf{x}_{P-1}$, to $\mathbf{x}_P$ represents a path in the $3N$-dimensional configuration-space linking $\mathbf{x}_0$ and $\mathbf{x}_P$, two spatial configurations of the nuclei. And all discussions above about the position space extend to this $3N$-dimensional configuration-space. The only impact on the equations above is that in Eq. 7.14 an extra iteration over the atoms needs be in included. With this extra iteration included, Eq. 7.14 becomes:

$$\rho\left(\mathbf{x}_0, \mathbf{x}_P, \beta\right) = \lim_{P\to\infty} \left[\prod_{j=1}^{N} \left(\frac{m_j P}{2\beta\pi\hbar^2}\right)^{\frac{P}{2}}\right] \int_V \int_V \cdots \int_V e^{-\beta\sum_{i=1}^{P}\left[\sum_{j=1}^{N}\frac{1}{2}m_j\omega_P^2\left(\mathbf{x}_i^j-\mathbf{x}_{i-1}^j\right)^2+\frac{1}{2P}\left(V(\mathbf{x}_i^1,\cdots,\mathbf{x}_i^N)+V(\mathbf{x}_{i-1}^1,\cdots,\mathbf{x}_{i-1}^N)\right)\right]} d\mathbf{x}_1 d\mathbf{x}_2 \cdots d\mathbf{x}_{P-1}. \tag{7.15}$$

Here $\mathbf{x}_i^j$ means the 3-dimensional vector in the position space associated with the j^{th} atom's i^{th} bead. We note that this understanding of $\mathbf{x}_i$ and associated Eq. 7.15 are the often used theoretical foundations for discussions of the density matrix in the path-integral molecular simulations. Again, P is a parameter which represents the number of slices sampled along the path, the convergence of the property under investigation with respect to this parameter must be tested in practical simulations.

7.1.3 Statistical Mechanics: Path-Integral Molecular Simulations

Eq. 7.15 gives an expression for the density matrix in terms of the path-integral in the $3N$-dimensional configuration-space, where N is the number of nuclei in the poly-atomic system. The diagonal part of this density matrix is the density function, which describes the probability of finding the poly-atomic system under investigation at a certain spatial configuration. This function can be obtained from Eq. 7.15 by setting $\mathbf{x}_0 = \mathbf{x}_P$, as:

$$\rho\left(\mathbf{x}_P, \mathbf{x}_P, \beta\right) = \lim_{P\to\infty} \left[\prod_{j=1}^{N} \left(\frac{m_j P}{2\beta\pi\hbar^2}\right)^{\frac{P}{2}}\right] \int_V \int_V \cdots \int_V e^{-\beta\sum_{i=1}^{P}\left[\sum_{j=1}^{N}\frac{1}{2}m_j\omega_P^2\left(\mathbf{x}_i^j-\mathbf{x}_{i-1}^j\right)^2+\frac{1}{2P}\left(V(\mathbf{x}_i^1,\cdots,\mathbf{x}_i^N)+V(\mathbf{x}_{i-1}^1,\cdots,\mathbf{x}_{i-1}^N)\right)\right]} d\mathbf{x}_1 d\mathbf{x}_2 \cdots d\mathbf{x}_{P-1}. \tag{7.16}$$

In Sec. 7.1.2, we said that the density matrix is $e^{-\beta\hat{H}}$ in the operator notation, whose trace gives us the partition function. Therefore, in the configuration-space, this partition function is easily obtainable from the density matrix. What we need to do is to perform an extra integration on $\mathbf{x}_P$ over the configuration-space in Eq. 7.16. This integration gives us the partition function Z^{Q} for the quantum canonical system

in the limit of P approaches infinity, through

$$Z^{\mathrm{Q}} = \lim_{P\to\infty}\left[\prod_{j=1}^{N}\left(\frac{m_j P}{2\beta\pi\hbar^2}\right)^{\frac{P}{2}}\right]\int_V\int_V\cdots\int_V e^{-\beta\sum_{i=1}^{P}\left[\sum_{j=1}^{N}\frac{1}{2}m_j\omega_P^2\left(\mathbf{x}_i^j-\mathbf{x}_{i-1}^j\right)^2+\frac{1}{2P}\left(V(\mathbf{x}_i^1,\cdots,\mathbf{x}_i^N)+V(\mathbf{x}_{i-1}^1,\cdots,\mathbf{x}_{i-1}^N)\right)\right]}d\mathbf{x}_1 d\mathbf{x}_2\cdots d\mathbf{x}_P. \tag{7.17}$$

This quantum canonical partition function is a function of temperature. When it is known, in principle, all thermodynamic quantities of the quantum system under investigation are obtainable.

Now we look at the partition function in Eq. 7.17. In practice, a finite P is always used. We label the partition function represented in Eq. 7.17 for a finite P as Z_P. We note that this Z_P can be understood as the "configurational" partition function for a fictitious $3N\times P$-particle system in an effective potential V^{eff}, in the form of

$$V^{\mathrm{eff}}(\mathbf{x}_1,\mathbf{x}_2,\cdots,\mathbf{x}_P) = \sum_{i=1}^{P}\left[\sum_{j=1}^{N}\frac{1}{2}m_j\omega_P^2\left(\mathbf{x}_i^j-\mathbf{x}_{i-1}^j\right)^2+\frac{1}{2P}\left(V(\mathbf{x}_i^1,\cdots,\mathbf{x}_i^N)+V(\mathbf{x}_{i-1}^1,\cdots,\mathbf{x}_{i-1}^N)\right)\right], \tag{7.18}$$

where $\mathbf{x}_0=\mathbf{x}_P$. Again, $\mathbf{x}_i$ is a $3N$-dimensional vector representing the spatial configuration of the nuclei in the i^{th} image and $\mathbf{x}_i^j$ is a 3-dimensional vector representing the position of the j^{th} nucleus in this image. P is the number of slices we have chosen for the sampling of the path-integral along the imaginary-time interval. Because of the similarity between the cyclic path and a necklace, these sampling points are also called "beads", "images", or "replicas" in literature. In terms of this V^{eff}, Z_P in Eq. 7.17 can be rewritten as

$$Z_P = \left[\prod_{j=1}^{N}\left(\frac{m_j P}{2\beta\pi\hbar^2}\right)^{\frac{P}{2}}\right]\int_V\int_V\cdots\int_V e^{-\beta V^{\mathrm{eff}}(\mathbf{x}_1,\mathbf{x}_2,\cdots,\mathbf{x}_P)}d\mathbf{x}_1 d\mathbf{x}_2\cdots d\mathbf{x}_P. \tag{7.19}$$

The relationship between this configuration partition function (Z_P) over a $3N\times P$ configuration-space and the quantum canonical partition function (Z^{Q}) of the real poly-atomic system is that Z_P equals Z^{Q} when P goes to infinity.

Pictorially, this relationship can be understand from the comparison as shown in Fig. 7.2. We use H_2, the simplest molecule, as an example. The canonical partition function of the quantum system is what we want to simulate. From Eq. 7.9, we know that one needs the eigenstate wave-functions and the eigenvalues of the nuclei, which is not feasible in studies of most poly-atomic systems, expect for descriptions of some simple gas-phase small molecules [59, 60, 61, 62]. As an alternative, one can resort to

Eq. 7.17 and construct a fictitious polymer for the real system under investigation. This polymer is composed by P replicas of the real poly-atomic system. In between the replicas, the same atoms are linked by spring interactions, whose spring constant (defined as $m_j\omega_P^2$) is determined by m_j and ω_P, with $\omega_P = \sqrt{P}/(\beta\hbar)$. Within one replica, the inter-atomic potential is calculated by either force-fields or *ab initio* methods upon which the molecular simulation is based. These two terms, *i.e.* the spring interaction and the intra-replica potential, correspond to the kinetic and the potential energies of the path-integral respectively. From the form of the spring constant as shown Eq. 7.17, it is clear that as the temperature and m_j go to infinity, the spring constant becomes so large that all the replicas overlap in configuration-space, resulting in a simulation in the classical limit. When the temperature is low and m_j is reasonably small, it is reasonable to expect that a molecular simulation based on this polymer gives results very different from the one with $P = 1$, *i.e.* the classical simulation. In other words, from P=1 (the classical simulation), when P approaches infinity, one approaches the quantum limit of this canonical ensemble. In practice, a finite P must be taken. The statistical results obtained from these simulations with a finite P should always be converged with respect to this P. The difference between results obtained from the $P = 1$ simulation and this path-integral converged simulation tells us the impact of QNEs on the statistical results.

For a more vivid explanation of how this artificial polymer in path-integral simulation looks like (with electronic structures calculated "on-the-fly" in an *ab initio* manner as the dynamics of the system evolves), we take a real system, *i.e.* a layer of squaric acid, a hydrogen-bonded molecular crystal, as an example and show a schematic scheme in Fig. 7.3. P is set as 16 and the temperature is 100 K. 16 images of the real system is generated and the same atom of the neighboring images is connected by artificial spring interactions. As said, for the electronic structures of the system in each image, they are calculated quantum mechanically using the *ab initio* method. This is shown by blue contours designating the density distribution of the electrons. Since the mass of the hydrogen is small, the spring interaction with which the hydrogen nuclei is connected is weak and consequently the images of the hydrogen nuclei are delocalized in real space. The mass of the oxygen nucleus is larger and consequently their dispersions are smaller but still observable. If we compare results of simulations using this polymer and the classical system (P=1), it is obvious that the QNEs are small for O and large for H. With the increase of the temperature, it is also easy to expect that the difference between simulations with P=1 and larger P decreases. For more details on this path-integral simulation, please refer to Li, Walker, and Michaelides' work in Ref. [322].

Then we come back to the mathematics. With this relationship between the "configurational" partition function of the polymer and the quantum partition function as introduced in the early paragraphs in mind, we now transfer all our attentions to this "configurational" partition function. Eq. 7.19 for this "configurational" par-

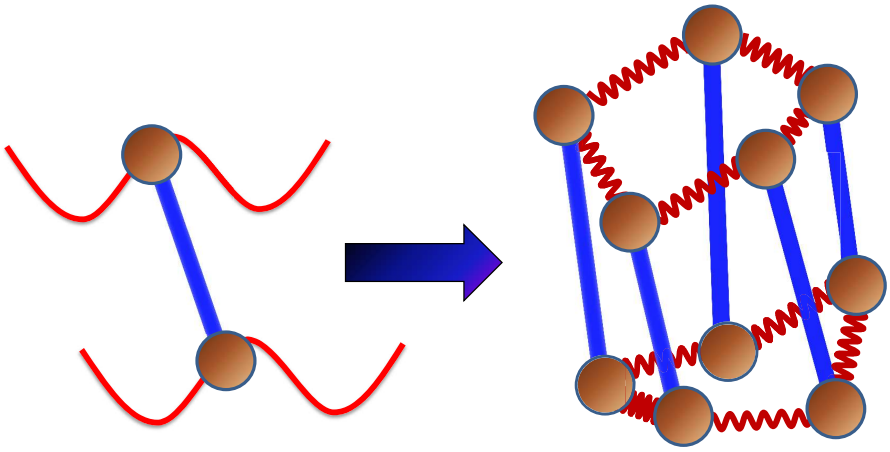

Figure 7.2: Illustration on how the mapping from the canonical quantum system to a classical polymer is done in path-integral statistical mechanics. The simplest molecule, H_2 is taken as an example. In principle, one needs to calculate the nuclear wave-functions, as shown on the left. Using path-integral, this calculation of the wave-function can be avoided. What one needs to do is to set up a fictitious polymer. This polymer is composed by P replicas of the real molecule. In each replica, the potential is determined by the real potential of the system at the specific spatial configuration of this replica. In between the replicas, the neighboring images (beads) of the same atoms are linked by springs. The spring constant is determined by m_j and ω_P as $m_j\omega_P^2$, where $\omega_P = \sqrt{P}/(\beta\hbar)$. Therefore, the higher the temperature, the heavier the nucleus, the stronger the interaction between the beads. In the limit of $T \to \infty$ and $m_j \to \infty$, one arrives at the classical limit when all images overlap with each other. The partition function of the quantum system as shown on the left equals the configurational partition function of the polymer on the right as $P \to \infty$.

tition function of a polymer may look a little complicated to be handled numerically from the first sight. However, for people working on molecular simulations, this is an equation which can't be more friendly. To understand what we mean by this statement, one just need to rewrite Z_P using a proper partition function in a fictitious phase space, composed by variables $\mathbf{x}_1, \cdots, \mathbf{x}_P, \mathbf{p}_1, \cdots, \mathbf{p}_P$, as

$$Z_P = C \int \int \cdots \int e^{-\beta H(\mathbf{x}_1, \cdots, \mathbf{x}_P, \mathbf{p}_1, \cdots, \mathbf{p}_P)} d\mathbf{x}_1 \cdots d\mathbf{x}_P d\mathbf{p}_1 \cdots \mathbf{p}_P. \tag{7.20}$$

The Hamiltonian in this equation is designed using the effective potential V^{eff}

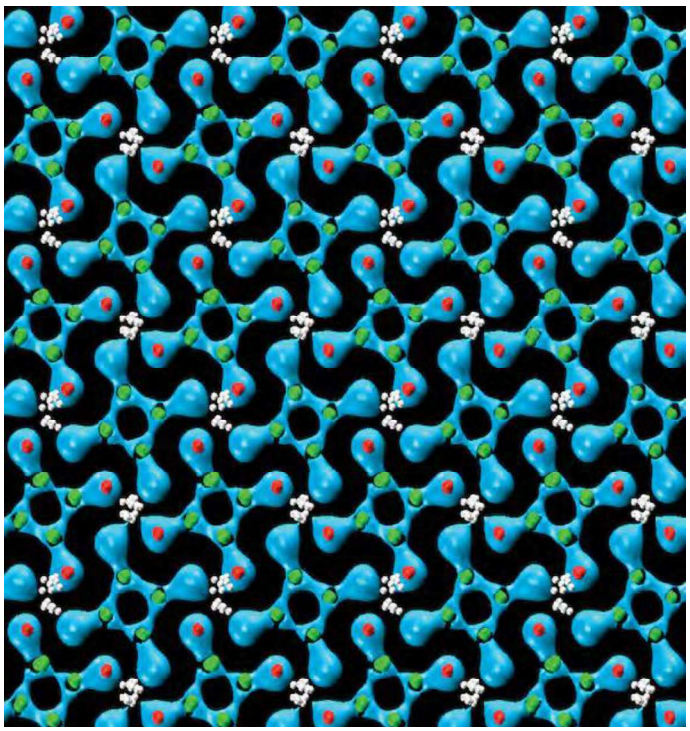

Figure 7.3: An example of the artificial polymer in a real path-integral molecular simulation, courtesy to Dr. Brent Walker for our joint paper (PNAS **108**, 6369 (2011)). The system is a layer of squaric acid, a molecular crystal held together with inter-molecular hydrogen bonds. The quantum nature of the nuclei is addressed using the path-integral treatment by generating a series of images for the real poly-atomic system and connecting the same atom in neighboring images with spring potential. The electronic structures are calculated quantum mechanically for each image. And the blue contour denotes the density distribution of the electrons in one image. More details please refer to Ref. [322].

through:

$$H(\mathbf{x}_1, \cdots, \mathbf{x}_P, \mathbf{p}_1, \cdots, \mathbf{p}_P) = \sum_{i=1}^{P} \sum_{j=1}^{N} \frac{(\mathbf{p}_i^j)^2}{2M_i^j} + V^{\text{eff}}(\mathbf{x}_1, \mathbf{x}_2, \cdots, \mathbf{x}_P). \tag{7.21}$$

Since the kinetic energy and the potential energy terms are separable in this Hamiltonian, one can easily replace the P-dependent constant $\left[\prod_{j=1}^{N} \left(\frac{m_j P}{2\beta\pi\hbar^2}\right)^{\frac{P}{2}}\right]$ in Eq. 7.19 by a product of $N \times P$ uncoupled Gaussian integrals, which originate from the integrals over momentum $\mathbf{p}_i^j$, as done in Eq. 7.20. The constant C in front of the integration over configurational and momentum space in Eq. 7.20 ensures that Z_P

is unchanged compared to Eq. 7.19. It is determined by the choice of the artificial mass M_i^j associated with the beads of each nucleus.

We note that such an equality means that for a finite P, the path-integral of a quantum system is isomorphic to a classical polymer composed by P replicas of the real poly-atomic system under investigation, subjecting to a classical Hamiltonian given by Eq. 7.21 [68]. In so doing, the molecular simulation techniques as introduced in the earlier chapters can be directly used. These molecular simulation techniques include both MD and MC methods, with which partition function as given in Eq. 7.20 can be evaluated. In the following, we discuss how these path-integral based molecular simulation techniques are used taking the MD based implementations as the guiding example. The only thing we need to take care is to design the fictitious polymer in a proper way, so that the contributions from the quantum nature of the nuclei to the statistical properties of the system are not miscounted. For people interested in the PIMC method, please refer to Ceperley *et al.*'s work in Refs. [70, 71, 72, 73].

Besides the partition function and the density matrix, other quantities, such as the expectation values of any physical observable $\hat{O}$, can also be described using this path-integral. The definition of such an expectation value is already given in Eq. 7.5. From this definition, one can obtain a path-integral based representation for the expectation value of this observable using the Trotter factorization. To understand this statement, we first go back to the path-integral representation of the propagator as shown in Eq. 7.2. As a matter of fact, its form originates and is equivalent to a Trotter factorization based equation. What one does in such a Trotter factorization is to insert $P-1$ identity matrices $\int d\mathbf{x}_i |\mathbf{x}_i\rangle\langle\mathbf{x}_i| = \mathrm{I}$ on the time slices between t_a and t_b. With this treatment, one arrives at such an equation for the propagator

$$G\left(\mathbf{x}_b, t_b; \mathbf{x}_a, t_a\right) = \lim_{P\to\infty} \frac{1}{A} \int_V \int_V \cdots \int_V \langle \mathbf{x}_a | e^{(i/\hbar)\hat{L}\Delta t} | \mathbf{x}_1 \rangle \langle \mathbf{x}_1 | e^{(i/\hbar)\hat{L}\Delta t} | \mathbf{x}_2 \rangle \cdots \\ \langle \mathbf{x}_{P-1} | e^{(i/\hbar)\hat{L}\Delta t} | \mathbf{x}_b \rangle \frac{d\mathbf{x}_1}{A} \frac{d\mathbf{x}_2}{A} \cdots \frac{d\mathbf{x}_{P-1}}{A}. \tag{7.22}$$

We note that this equation is equivalent to the path-integral treatment in terms of action in Eqs. 7.2, 7.3, and 7.4.

With this equality in mind, one can rewrite the expectation value of $\hat{O}$ in the

configuration-space as

$$\begin{aligned}\langle\hat{O}\rangle =&(Z^{\mathrm{Q}})^{-1}\mathrm{Tr}\left[\hat{O}e^{-\beta\hat{H}}\right]\\ =&\lim_{P\to\infty}\frac{1}{Z_P}\int_V\int_V\cdots\int_V \langle\mathbf{x}_0|\hat{O}e^{-\frac{1}{P\beta}\hat{H}}|\mathbf{x}_1\rangle\langle\mathbf{x}_1|e^{-\frac{1}{P\beta}\hat{H}}|\mathbf{x}_2\rangle\cdots\\ &\langle\mathbf{x}_{P-1}|e^{-\frac{1}{P\beta}\hat{H}}|\mathbf{x}_P\rangle d\mathbf{x}_1 d\mathbf{x}_2\cdots d\mathbf{x}_P\\ =&\lim_{P\to\infty}\frac{1}{Z_P}\int_V\int_V\cdots\int_V O(\mathbf{x}_1)\langle\mathbf{x}_0|e^{-\frac{1}{P\beta}\hat{H}}|\mathbf{x}_1\rangle\langle\mathbf{x}_1|e^{-\frac{1}{P\beta}\hat{H}}|\mathbf{x}_2\rangle\cdots\\ &\langle\mathbf{x}_{P-1}|e^{-\frac{1}{P\beta}\hat{H}}|\mathbf{x}_P\rangle d\mathbf{x}_1 d\mathbf{x}_2\cdots d\mathbf{x}_P,\end{aligned} \tag{7.23}$$

where $\mathbf{x}_0=\mathbf{x}_P$ and $O(\mathbf{x}_1)$ means the expectation value of $\hat{O}$ at $\mathbf{x}_1$. Due to the fact that $\hat{H}/(P\beta)$ is a infinitely small Trotter factor, the same treatment also applies to $\mathbf{x}_2$, as:

$$\begin{aligned}\langle\hat{O}\rangle =&\lim_{P\to\infty}\frac{1}{Z_P}\int_V\int_V\cdots\int_V \langle\mathbf{x}_0|e^{-\frac{1}{P\beta}\hat{H}}|\mathbf{x}_1\rangle\langle\mathbf{x}_1|\hat{O}e^{-\frac{1}{P\beta}\hat{H}}|\mathbf{x}_2\rangle\cdots\\ &\langle\mathbf{x}_{P-1}|e^{-\frac{1}{P\beta}\hat{H}}|\mathbf{x}_P\rangle d\mathbf{x}_1 d\mathbf{x}_2\cdots d\mathbf{x}_P\\ =&\lim_{P\to\infty}\frac{1}{Z_P}\int_V\int_V\cdots\int_V O(\mathbf{x}_2)\langle\mathbf{x}_0|e^{-\frac{1}{P\beta}\hat{H}}|\mathbf{x}_1\rangle\langle\mathbf{x}_1|e^{-\frac{1}{P\beta}\hat{H}}|\mathbf{x}_2\rangle\cdots\\ &\langle\mathbf{x}_{P-1}|e^{-\frac{1}{P\beta}\hat{H}}|\mathbf{x}_P\rangle d\mathbf{x}_1 d\mathbf{x}_2\cdots d\mathbf{x}_P.\end{aligned} \tag{7.24}$$

Then we can continue such a cycling to $\mathbf{x}_P$ and make an average over all the images. Such a treatment gives us an expression for the expectation value of $\hat{O}$ as:

$$\begin{aligned}\langle\hat{O}\rangle =\lim_{P\to\infty}\frac{1}{Z_P}\int_V\int_V\cdots\int_V &\left[\frac{1}{P}\sum_{i=1}^{P}O(\mathbf{x}_i)\right]\langle\mathbf{x}_0|e^{-\frac{1}{P\beta}\hat{H}}|\mathbf{x}_1\rangle\langle\mathbf{x}_1|e^{-\frac{1}{P\beta}\hat{H}}|\mathbf{x}_2\rangle\cdots\\ &\langle\mathbf{x}_{P-1}|e^{-\frac{1}{P\beta}\hat{H}}|\mathbf{x}_P\rangle d\mathbf{x}_1 d\mathbf{x}_2\cdots d\mathbf{x}_P.\end{aligned} \tag{7.25}$$

In so doing, the equation from which the expectation value of any physical observable is calculated in the often used path-integral scheme is arrived at.

We note that most of the studies in this field focus on the expectation value of local physical quantities [282, 286, 321, 322], such as the density function. In recent years, however, simulations for some non-local physical quantities such as the momentum distribution of proton in water have also attracted many attentions from the theoretical perspective, especially after the deep inelastic neutron scattering (DINS) experiment becomes available [334, 335, 336]. In these cases, rigorously speaking, the so-called open-path integral molecular dynamics method should be resorted to (see e.g. Morrone, Lin and Car's work in Refs. [337, 338, 339]), where

the constraint $\mathbf{x}_0 = \mathbf{x}_P$ is released. This open path allows the density matrix itself to be simulated. However, we note that compared with the normal PIMD simulations with close path, special care must be taken in the open-path simulations concerning its stability. To deal with problem, some new methods on simulating the momentum distribution using the conventional close-path PIMD method were also proposed, see e.g. Refs. [340, 341, 342]. For people interested in theoretical simulations concerning this quantity, please refer to Morrone, Lin, Car, and Parrinello's work in Refs. [337, 338, 339, 340, 341] or Ceriotti and Manolopoulos' work in Ref. [342].

7.1.4 Staging and Normal-Mode Transformations

In terms of molecular dynamics, the canonical sampling associated with the partition function in Eq. 7.20, the density function in Eq. 7.15, and the expectation value of a physical observable in Eq. 7.25 can be obtained using the equations of motion of the fictitious polymer resulting from the Hamiltonian in Eq. 7.21.

A number of well-known numerical difficulties, however, exist in such a straightforward implementation of the PIMD method. These difficulties mainly arise from three aspects. First, from the definition of ω_P, which equals $\sqrt{P}/(\beta\hbar)$, it is clear that the stiffness of the spring constant increases with P. Therefore, with the increase of the number of beads, if the masses of the beads are independent on it, the spring interaction requires smaller and smaller time-steps for the PIMD simulations to be carried out in order to characterize the inter-bead vibrations. Second, the stiffness of this spring interaction results in the external potential generated from the *ab initio* (or force-field) calculations within each image serving only as a small perturbation to the spring interaction. Consequently, the trajectories for the beads of the artificial polymer will remain close to "invariant tori" in the Cartesian space and efficient sampling of its entire configuration-space is serious hindered. Third, even if this multi time-scale and the "invariant tori" problems are solved, a sufficient number of thermostats should still be incorporated into the dynamical scheme to ensure ergodicity of a simple polymer in the PIMD simulations. Therefore, the ergodicity for the configuration-space sampling of the fictitious polymer in the PIMD simulation is technically much more tricky than a simple implementation of the equation of motion generated from Eq. 7.21. To the best of our knowledge, this non-ergodic sampling in direct implementations of the PIMD method was first pointed out by Hall and Berne in 1984 [343], using water and liquid neon as examples. To a certain extend, this is also why the Monte-Carlo methods are preferentially used in the path-integral molecular simulations in the 1980s [70, 71, 72, 73]. A MD-based method, in which an efficient sampling over the configuration-space of the artificial polymer was guaranteed, was highly desired.

These difficulties had been largely solved in the late 1980s and the early 1990s. In order for such these efficient sampling methods to be explained in a clean manner,

we first rewrite the Hamiltonian in Eq. 7.21 in the following form

$$\begin{aligned} &H(\mathbf{x}_1, \cdots, \mathbf{x}_P, \mathbf{p}_1, \cdots, \mathbf{p}_P) \\ &\quad = \sum_{j=1}^{N} \sum_{i=1}^{P} \frac{(\mathbf{p}_i^j)^2}{2M_i^j} + \sum_{j=1}^{N} \sum_{i=1}^{P} \frac{1}{2} m_j \omega_P^2 \left(\mathbf{x}_i^j - \mathbf{x}_{i-1}^j\right)^2 + \sum_{i=1}^{P} \frac{1}{P} V(\mathbf{x}_i^1, \cdots, \mathbf{x}_i^N), \end{aligned} \tag{7.26}$$

where the close-path feature $\mathbf{x}_0 = \mathbf{x}_P$ is used to simplify the $V(\mathbf{x}_i^1, \cdots, \mathbf{x}_i^N)$ term, as compared to Eqs. 7.21 and 7.18. For a transparent nomenclature in the following discussions, in between the summation over beads and nuclei, we take the sum over nuclei (N) as the outer loop since the form of coordinate transformation, which serves as the key step in solving this ergodicity problem, doesn't depend on the nuclei. In addition to this simplification of the potential energy term, since the first term in Eqs. 7.21 and 7.26 is just introduced in the molecular dynamics simulations to sample the configuration space, the mass M_i^j in this term, in principle, is arbitrary for calculations of the statistical properties. And, it is allowed to have one value for each artificial particle in the polymer (in total $N \times P$ artificial particles), as long as the spring constant is physical. With this in mind, Eq. 7.26 can be further reformed into

$$\begin{aligned} &H(\mathbf{x}_1, \cdots, \mathbf{x}_P, \mathbf{p}_1, \cdots, \mathbf{p}_P) \\ &\quad = \sum_{j=1}^{N} \sum_{i=1}^{P} \frac{(\mathbf{p}_i^j)^2}{2M_i^j} + \sum_{j=1}^{N} \frac{1}{2} m_j \omega_P^2 \mathbf{x}^j \mathbf{A} \mathbf{x}^j + \frac{1}{P} \sum_{i=1}^{P} V(\mathbf{x}_i^1, \cdots, \mathbf{x}_i^N), \end{aligned} \tag{7.27}$$

where

$$\mathbf{A} = \begin{Bmatrix} 2 & -1 & 0 & 0 & \cdots & 0 & 0 & 0 & -1 \\ -1 & 2 & -1 & 0 & \cdots & 0 & 0 & 0 & 0 \\ 0 & -1 & 2 & -1 & \cdots & 0 & 0 & 0 & 0 \\ \vdots & \vdots & \vdots & \vdots & \vdots & \vdots & \vdots & \vdots & \vdots \\ 0 & 0 & 0 & 0 & \cdots & -1 & 2 & -1 & 0 \\ 0 & 0 & 0 & 0 & \cdots & 0 & -1 & 2 & -1 \\ -1 & 0 & 0 & 0 & \cdots & 0 & 0 & -1 & 2 \end{Bmatrix}. \tag{7.28}$$

Here, $\mathbf{A}$ is a $P \times P$ matrix. For the matrix multiplication term $(1/2) m_j \omega_P^2 \mathbf{x}^j \mathbf{A} \mathbf{x}^j$ in Eq. 7.27, $\mathbf{x}^j$ can be viewed as a P-dimensional vector composed by $(\mathbf{x}_1^j, \mathbf{x}_2^j, \cdots, \mathbf{x}_P^j)$, with $\mathbf{x}_i^j$ representing the position of the i^{th} image of the j^{th} nucleus. When this position is a 3-dimensional vector in the Cartesian space, this matrix multiplication term goes through the coordinate of x, y, and z one-by-one. We note that M_i^j is the artificial mass we set for the i^{th} image of the j^{th} nucleus, while m_j is the physical mass of the j^{th} nucleus.

From Eq. 7.27, it is clear that the smallest time-step required in the PIMD simulations to describe the motion of the polymer, which originates from the spring interaction between neighboring beads, is associated with the largest eigenvalue of the matrix **A**. However, we note that an artificial mass can be attributed to each fictitious particle in the polymer. Based on this advantage which is intrinsic in the principles of the PIMD method, a coordinate transformation can be employed to solve the infamous multi time-scale problem originating from the inter-bead vibrations. This coordinate transformation first decouples the harmonic interactions between neighboring beads in Eq. 7.27. Then, the mass associated with the different re-normalized degrees of freedoms (after coordinate transformation) can be artificially chosen so that the spring interaction results in vibrations of the same frequency. And it is advisable to choose those masses so that the resulting frequency doesn't depend on P. In so doing, the problems associated with the inter-image vibrations can be avoided so that an efficient sampling of the polymer's configuration space can be carried out in a much easier manner.

In order for such a decoupling of the spring interactions between neighboring beads to be carried out, there are currently two popular schemes for the PIMD simulations to follow. The first one is the so-called "staging" method. It was originally proposed in a PIMC algorithm [71] and then employed in the PIMD simulations [319]. In this method, taking the j^{th} nucleus as an example, the coordinate transformation from the original ones $(\mathbf{x}_1^j, \mathbf{x}_2^j, \cdots, \mathbf{x}_P^j)$ to the transformed ones $(\mathbf{u}_1^j, \mathbf{u}_2^j, \cdots, \mathbf{u}_P^j)$ is

$$\begin{aligned} \mathbf{u}_1^j &= \mathbf{x}_1^j \\ \mathbf{u}_i^j &= \mathbf{x}_i^j - \frac{(i-1)\mathbf{x}_{i+1}^j + \mathbf{x}_1^j}{i}, \text{ for } i \geq 2, \end{aligned} \tag{7.29}$$

whose form doesn't depend on the nuclear index j. The inverse of this relation is

$$\begin{aligned} \mathbf{x}_1^j &= \mathbf{u}_1^j \\ \mathbf{x}_i^j &= \mathbf{u}_1^j + \sum_{l=i}^{P} \frac{(i-1)}{l-1}\mathbf{u}_l^j, \text{ for } i \geq 2, \end{aligned} \tag{7.30}$$

which can also be obtained recursively by

$$\begin{aligned} \mathbf{x}_1^j &= \mathbf{u}_1^j \\ \mathbf{x}_i^j &= \mathbf{u}_i^j + \frac{(i-1)}{i}\mathbf{x}_{i+1}^j + \frac{1}{i}\mathbf{x}_1^j, \text{ for } i \geq 2. \end{aligned} \tag{7.31}$$

Since $\mathbf{x}_{P+1}^j = \mathbf{x}_1^j$, one often carries out the recursion in Eq. 7.31 in order of $\mathbf{x}_1^j, \mathbf{x}_P^j$, $\mathbf{x}_{P-1}^j, \cdots, \mathbf{x}_2^j$.

One advantage of such a transformed coordinates is that the inter-bead spring interaction can be normalized through

$$\sum_{i=1}^{P}(\mathbf{x}_i^j - \mathbf{x}_{i+1}^j)^2 = \sum_{i=2}^{P}\frac{i}{i-1}(\mathbf{u}_i^j)^2. \tag{7.32}$$

To understand such a relationship from a practical perspective, we take the $P = 4$ case as an example. The relationship between the original coordinates and the transformed ones in Eq. 7.29 indicates

$$\begin{aligned}
\mathbf{u}_1^j &= \mathbf{x}_1^j \\
\mathbf{u}_4^j &= \mathbf{x}_4^j - \frac{3\mathbf{x}_1^j + \mathbf{x}_1^j}{4} = \mathbf{x}_4^j - \mathbf{x}_1^j \\
\mathbf{u}_3^j &= \mathbf{x}_3^j - \frac{2\mathbf{x}_4^j + \mathbf{x}_1^j}{3} \\
\mathbf{u}_2^j &= \mathbf{x}_2^j - \frac{\mathbf{x}_3^j + \mathbf{x}_1^j}{2}.
\end{aligned} \tag{7.33}$$

Putting this relation into $\sum_{i=2}^{4}\frac{i}{i-1}(\mathbf{u}_i^j)^2$, one easily obtains

$$\begin{aligned}
\sum_{i=2}^{4}\frac{i}{i-1}(\mathbf{u}_i^j)^2 =& 2(\mathbf{u}_2^j)^2 + \frac{3}{2}(\mathbf{u}_3^j)^2 + \frac{4}{3}(\mathbf{u}_4^j)^2 \\
=& 2(\mathbf{x}_2^j - \frac{\mathbf{x}_3^j + \mathbf{x}_1^j}{2})^2 + \frac{3}{2}(\mathbf{x}_3^j - \frac{2\mathbf{x}_4^j + \mathbf{x}_1^j}{3})^2 + \frac{4}{3}(\mathbf{x}_4^j - \mathbf{x}_1^j)^2 \\
=& 2(\mathbf{x}_1^j)^2 + 2(\mathbf{x}_2^j)^2 + 2(\mathbf{x}_3^j)^2 + 2(\mathbf{x}_1^j)^2 - 2\mathbf{x}_1^j\mathbf{x}_2^j - 2\mathbf{x}_2^j\mathbf{x}_3^j - 2\mathbf{x}_3^j\mathbf{x}_4^j - 2\mathbf{x}_4^j\mathbf{x}_1^j \\
=& \sum_{i=1}^{4}(\mathbf{x}_i^j - \mathbf{x}_{i+1}^j)^2
\end{aligned} \tag{7.34}$$

Therefore, the coordinate transformation decouples the relative motion of the beads in the position space.

Another point which is implied in Eqs. 7.29 and 7.30 is that there is a one-to-one correspondence between $(\mathbf{x}_1^j, \mathbf{x}_2^j, \cdots, \mathbf{x}_P^j)$ and $(\mathbf{u}_1^j, \mathbf{u}_2^j, \cdots, \mathbf{u}_P^j)$. Therefore, by setting

$$\begin{aligned}
m_1^j &= 0 \\
m_i^j &= \frac{i}{i-1}m_j, \text{for } i \geq 2,
\end{aligned} \tag{7.35}$$

Eq. 7.27 can be rewritten as

$$\begin{aligned} H(\mathbf{x}_1,\cdots,\mathbf{x}_P,\mathbf{p}_1,\cdots,\mathbf{p}_P) =& H(\mathbf{u}_1,\cdots,\mathbf{u}_P,\mathbf{P}_1,\cdots,\mathbf{P}_P) \\ =& \sum_{j=1}^{N}\sum_{i=1}^{P}\left[\frac{(\mathbf{P}_i^j)^2}{2M'^j_i}+\frac{1}{2}m_i^j\omega_P^2(\mathbf{u}_i^j)^2\right]+\sum_{i=1}^{P}\frac{1}{P}V(\mathbf{u}_i^1,\cdots,\mathbf{u}_i^N). \end{aligned} \tag{7.36}$$

Here $\mathbf{P}_i$ is assumed to be conjugate to $\mathbf{u}_i$ in the transformed coordinates, and M'^j_i is the associated mass which is related to the M_i^j in Eq. 7.26 by the coordinate transition in Eq. 7.29. We don't need to care about the specific form of this relation. There is no potential originating from the harmonic spring interaction for the first artificial particle in the transformed coordinate of the polymer ($m_1^j = 0$). For the artificial particles associated with the other degrees of freedom, this potential is determined by m_i^j ($i \geq 2$) in Eq. 7.35. Therefore, as long as we keep M'^j_i ($i \geq 2$) as a constant multiple of m_i^j, the vibrations originating from the spring interactions associated with the other re-normalized degrees of freedom will share the same time-scale. In practice, these M'^j_is are often chosen as $M'^j_1 = m_j$ (physical mass of the j^{th} nucleus) and $M'^j_i = m_i^j$ for $i \geq 2$. The equations of motion in the transformed coordinates obtained from the Hamiltonian in Eq. 7.36 is

$$\begin{aligned} \dot{\mathbf{u}}_i^j &= \frac{\mathbf{P}_i^j}{M'^j_i} \\ \dot{\mathbf{P}}_i^j &= -m_i^j\omega_P^2\mathbf{u}_i^j-\frac{1}{P}\frac{\partial V}{\partial \mathbf{u}_i^j}, \end{aligned} \tag{7.37}$$

where the only term which needs to be obtained from calculations in the original Cartesian space is $\partial V/\partial \mathbf{u}_i^j$.

In order for such forces in the transformed coordinate space to be obtained, one needs to go back to the original Cartesian space and calculate the Hellmann-Feynman forces of the corresponding nuclear configuration, namely, $\partial V/\partial \mathbf{x}_i^j$. Then a transformation must be made to link these $\partial V/\partial \mathbf{x}_i^j$s with the $\partial V/\partial \mathbf{u}_i^j$s to be used for the simulation of the propagation in Eq. 7.37. Such a transformation is defined from Eqs. 7.29 and 7.30. The starting point is the following equation

$$\begin{aligned} \frac{1}{P}\frac{\partial V}{\partial \mathbf{u}_k^j} =& \frac{1}{P}\sum_{i=1}^{P}\frac{\partial V}{\partial \mathbf{x}_i^j}\frac{\partial \mathbf{x}_i^j}{\partial \mathbf{u}_k^j}, \\ \frac{1}{P}\frac{\partial V}{\partial \mathbf{x}_k^j} =& \frac{1}{P}\sum_{i=1}^{P}\frac{\partial V}{\partial \mathbf{u}_i^j}\frac{\partial \mathbf{u}_i^j}{\partial \mathbf{x}_k^j} \end{aligned} \tag{7.38}$$

for a certain k. When $k = 1$, from Eq. 7.30, it is clear that $\partial \mathbf{x}_i^j/\partial \mathbf{u}_k^j$ equals one for

any i. Therefore, using the first equation in Eq. 7.38, one easily obtains

$$\frac{1}{P}\frac{\partial V}{\partial \mathbf{u}_1^j} = \frac{1}{P}\sum_{i=1}^{P}\frac{\partial V}{\partial \mathbf{x}_i^j}. \tag{7.39}$$

When $k \geq 2$, from Eq. 7.29, it is clear that $\partial \mathbf{u}_1^j / \partial \mathbf{x}_k^j = 0$ and $\partial \mathbf{u}_i^j / \partial \mathbf{x}_k^j \neq 0$ for $i \geq 2$. Therefore, the second equation in Eq. 7.38 becomes

$$\begin{aligned}\frac{1}{P}\frac{\partial V}{\partial \mathbf{x}_k^j} =& \frac{1}{P}\sum_{i=1}^{P}\frac{\partial V}{\partial \mathbf{u}_i^j}\frac{\partial \mathbf{u}_i^j}{\partial \mathbf{x}_k^j} \\ =& \frac{1}{P}\sum_{i=2}^{P}\frac{\partial V}{\partial \mathbf{u}_i^j}\frac{\partial \mathbf{u}_i^j}{\partial \mathbf{x}_k^j}.\end{aligned} \tag{7.40}$$

Then, we can make use of the second equation in Eq. 7.29 and rewrite it into

$$\begin{aligned}\frac{1}{P}\frac{\partial V}{\partial \mathbf{x}_k^j} =& \frac{1}{P}\sum_{i=2}^{P}\frac{\partial V}{\partial \mathbf{u}_i^j}\frac{\partial \mathbf{u}_i^j}{\mathbf{x}_k^j} \\ =& \frac{1}{P}\sum_{i=2}^{P}\frac{\partial V}{\partial \mathbf{u}_i^j}\left[\frac{\partial \mathbf{x}_i^j}{\partial \mathbf{x}_k^j} - \frac{i-1}{i}\frac{\partial \mathbf{x}_{i+1}^j}{\partial \mathbf{x}_k^j}\right] \\ =& \frac{1}{P}\sum_{i=2}^{P}\frac{\partial V}{\partial \mathbf{u}_i^j}\left[\delta_{i,k} - \frac{i-1}{i}\delta_{i+1,k}\right] \\ =& \frac{1}{P}\frac{\partial V}{\partial \mathbf{u}_k^j} - \frac{1}{P}\frac{k-2}{k-1}\frac{\partial V}{\partial \mathbf{u}_{k-1}^j}.\end{aligned} \tag{7.41}$$

Therefore, the $\partial V / \partial \mathbf{u}_k^j$ can be calculated recursively from:

$$\frac{1}{P}\frac{\partial V}{\partial \mathbf{u}_k^j} = \frac{1}{P}\frac{\partial V}{\partial \mathbf{x}_k^j} + \frac{1}{P}\frac{k-2}{k-1}\frac{\partial V}{\partial \mathbf{u}_{k-1}^j}. \tag{7.42}$$

Combining Eq. 7.39 and 7.42, the $\partial V / \partial \mathbf{u}_k^j$s to be used in the numerical simulation of the propagation in Eq. 7.37 should be calculated recursively from

$$\begin{aligned}\frac{1}{P}\frac{\partial V}{\partial \mathbf{u}_1^j} =& \frac{1}{P}\sum_{i=1}^{P}\frac{\partial V}{\partial \mathbf{x}_i^j} \\ \frac{1}{P}\frac{\partial V}{\partial \mathbf{u}_k^j} =& \frac{1}{P}\frac{\partial V}{\partial \mathbf{x}_k^j} + \frac{1}{P}\frac{k-2}{k-1}\frac{\partial V}{\partial \mathbf{u}_{k-1}^j}, \text{ for } k \geq 2.\end{aligned} \tag{7.43}$$

It is worth noting that different from the recursion for the transformation of the coordinates between $\mathbf{x}_i^j$ and $\mathbf{u}_i^j$ in Eq. 7.31, the force transformation here starts from $k = 2$, after $\partial V / \partial \mathbf{u}_1^j$ is obtained using the first expression in Eq. 7.43.

With these, the coordinate transformation which decouples the movement of the neighboring images and imposes one single frequency for all these inter-bead vibrations has been introduced. The next thing one needs to do in order for an ergodic sampling of the polymer to be carried out naturally locates at a massive thermostat sampling for all the degrees of freedom for the artificial polymer in the transformed coordinates. This thermostat sampling can be performed using the thermostats as introduced in Chapter 5. Taking the Andersen thermostat an example, in this case, the momentum $\mathbf{P}_i^j$ for $1 \leq i \leq P$ and $1 \leq j \leq N$ should be re-scaled for the desired temperature during each collision between the artificial particle and the thermostat. While in the case when Nosé-Hoover chain thermostat of a certain length is used, the equation of motion in Eq. 7.37 for the i^{th} bead of the j^{th} nucleus should be linked with this Nosé-Hoover chain according to Eq. 5.52. One notes that the computational cost of these thermostats is much smaller than the force calculation in real poly-atomic systems, especially when *ab initio* methods for the electronic structures are used. Therefore, picking up a thermostat which is efficient in pushing the polymer into its equilibrium state is essential in practical PIMD simulations.

So far about the "staging" transformation. As mentioned, the coordinate transformation aims at decoupling the relative motion between neighboring beads in the transformed coordinates. Therefore, as an alternative to the "staging" method, the most direct way to fulfill such a task is to diagonalize the matrix $\mathbf{A}$ in Eq. 7.28 and then use its eigenvectors to perform the coordinate transformation. In so doing, the Hamiltonian in Eq. 7.27 will have diagonal spring interactions in its second term in the transformed coordinates, with the constant of these diagonal spring interactions determined by the eigenvalues of the matrix $\mathbf{A}$. This method is the so-called "normal-mode" method in literature [81, 319]. Parallel to the "staging" method, it is the other often used coordinate transformation method in practical PIMD simulations.

Now we go into the details on how such a "normal-mode" transformation is performed. Since the matrix $\mathbf{A}$ is the same for all the nuclei, a single unitary orthogonal matrix $\mathbf{U}$ can be used to transform coordinates of all nuclei from the Cartesian to the normal-mode ones. This transformation reads

$$\mathbf{u}^j = \frac{1}{\sqrt{P}}\mathbf{U}\mathbf{x}^j \text{ and } \mathbf{x}^j = \sqrt{P}\mathbf{U}^{\mathrm{T}}\mathbf{u}^j, \tag{7.44}$$

where j goes through all the nuclear index from 1 to N. From our knowledge on linear algebra, we know that the matrix $\mathbf{U}$ can also be used to diagonalize the matrix $\mathbf{A}$ through $P\mathbf{U}\mathbf{A}\mathbf{U}^T$, and the resulting matrix Γ is diagonal. If we choose

the number of P as even (which equals $2n+2$) and align Γ as:

$$\Gamma = \begin{Bmatrix} \lambda_{-n} & 0 & 0 & 0 & 0 & 0 \\ 0 & \lambda_{-n+1} & 0 & 0 & 0 & 0 \\ 0 & 0 & \cdots & 0 & 0 & 0 \\ 0 & 0 & 0 & \lambda_0 & 0 & 0 \\ 0 & 0 & 0 & 0 & \cdots & 0 \\ 0 & 0 & 0 & 0 & 0 & \lambda_{n+1} \end{Bmatrix}, \tag{7.45}$$

the unitary orthogonal matrix $\mathbf{U}$ will have the following simple form:

$$U_{k,i} = \begin{cases} \sqrt{2/P}\sin\left(\frac{2\pi ki}{2n+2}\right), & -n \leq k < 0 \\ \sqrt{1/P}, & k = 0 \\ \sqrt{2/P}\cos\left(\frac{2\pi ki}{2n+2}\right), & 0 < k \leq n \\ (-1)^i/\sqrt{P}, & k = n+1 \end{cases} \tag{7.46}$$

Here, the row index k goes from $-n$ to $n+1$ and the column index l goes from 1 to P [344]. In other words, we label the beads from 1 to P in the Cartesian coordinates and from $-n$ to $n+1$ in the normal mode coordinates. The diagonal elements of Γ are: $\lambda_0 = 0$, $\lambda_{\pm i} = 4P\sin^2(i\pi/P)$ for $0 < i \leq n$, and $\lambda_{n+1} = 4P$. In the transformed "normal-mode" coordinates, the Hamiltonian in Eq. 7.27 then reads

$$\begin{aligned} &H(\mathbf{u}_{-n}, \cdots, \mathbf{u}_{n+1}, \mathbf{P}_{-n}, \cdots, \mathbf{P}_{n+1}) \\ &= \sum_{j=1}^{N} \sum_{i=-n}^{n+1} \left[\frac{(\mathbf{p}_i^j)^2}{2M'^j_i} + \frac{1}{2} m_j \omega_P^2 \lambda_i (\mathbf{u}_i^j)^2 \right] + \sum_{i=-n}^{n+1} \frac{1}{P} V(\mathbf{u}_i^1, \cdots, \mathbf{u}_i^N). \end{aligned} \tag{7.47}$$

From the expression of the transformation matrix $\mathbf{U}$ in Eq. 7.46, it is clear that in principle it is equivalent to a Fourier transform of a periodic path. For the eigenvector associated with the eigenvalue $\lambda_0 = 0$, from Eqs. 7.44 and 7.46 we see that the transformed coordinate should be

$$\mathbf{u}_0^j = \frac{1}{\sqrt{P}} \sum_{i=1}^{P} \mathbf{U}_{0,i} \mathbf{x}_i^j = \frac{1}{P} \sum_{i=1}^{P} \mathbf{x}_i^j, \tag{7.48}$$

which represents the centroid of the path of the j^{th} nucleus. Therefore, in the normal-mode coordinate, the propagation of this specific mode naturally describes the evolution of the centroid. Analogous to the "staging" method, from the other eigenvalues of the matrix Γ and the fact that an artificial mass M'^j_i can be set for each artificial particle, one can easily choose

$$\begin{aligned} M_0^j &= m_j \\ M_i^j &= c\lambda_i m_j, \text{for } -n \leq i \leq -1 \text{and } 1 \leq i \leq n+1, \end{aligned} \tag{7.49}$$

with c representing a constant. With these, the different modes corresponding to the inter-bead vibrations naturally move on the same time scale.

From the Hamiltonian in Eq. 7.48, the equation of motion is easily obtainable from

$$\begin{aligned}\dot{\mathbf{u}}_i^j &= \frac{\mathbf{P}_i^j}{M'^j_i} \\ \dot{\mathbf{P}}_i^j &= -m_i^j \omega_P^2 \lambda_i \mathbf{u}_i^j - \frac{1}{P}\frac{\partial V}{\partial \mathbf{u}_i^j}.\end{aligned} \tag{7.50}$$

The next thing one needs to do is the same as above descriptions for the "staging" method, *i.e.* calculating $\partial V/\partial \mathbf{u}_i^j$ from $\partial V/\partial \mathbf{x}_i^j$. Compared with the "staging" method, here, due to the fact that the coordinate transformation is performed with a constant matrix determined by P only, from Eqs. 7.38 and 7.44, this transformation between $\partial V/\partial \mathbf{u}_i^j$ from $\partial V/\partial \mathbf{x}_i^j$ can be carried out in a much simpler manner.

In Eq. 7.44, we can see that the transformation between the Cartesian and the normal-mode coordinate can be carried out as follows. For a specific nucleus, e.g, the j^{th}, we go through the indices x, y, and z one-by-one. For each index, e.g. the x index, the Cartesian coordinates of the P images were organized as a P-dimensional vector. Then the coordinate transformation to $\mathbf{u}^j$ is carried out using Eq. 7.44. In the force transformations, we follow the same routine. For the j^{th} nucleus, we go through the indices x, y, and z one-by-one. For each index, e.g. x, the forces along the x axis on the P images of the j^{th} nucleus were organized as a P-dimensional vector, which we label as F^j. It is composed by $(\frac{\partial V}{\partial \mathbf{x}_1^j}|_x, \cdots, \frac{\partial V}{\partial \mathbf{x}_P^j}|_x)$, where $\frac{\partial V}{\partial \mathbf{x}_i^j}|_x$ means the Hellmann-Feynman force on the i^{th} image of the j^{th} nucleus along the x axis. We label F'^j as the vector which represents the transformed forces, composed by $(\frac{\partial V}{\partial \mathbf{u}_{-n}^j}|_x, \cdots, \frac{\partial V}{\partial \mathbf{u}_{n+1}^j}|_x)$. Then, from Eqs. 7.38 and 7.44, one easily obtains

$$\frac{1}{P}F'^j = \frac{1}{\sqrt{P}}\mathbf{U}^T F^j. \tag{7.51}$$

These forces are then used to propagate the equation of motion in Eq. 7.50. Analogous to what we say in the "staging" method, again, massive thermostats must be used, with an efficient imposed on each degree of freedom. With these, an ergodic sampling can also be realized using this "normal-mode" method. We note that due to the advantage that the 0^{th} (according to our labeling from $-n$ to $n+1$) normal-mode naturally describes the propagation of the centroid, which does have a physical meaning, the "normal-mode" method is getting more and more popular nowadays, especially when extensions to real-time propagation is concerned. We will give a brief discussion to this extension in Sec. 7.2.

7.1.5 Evaluation of the Zero-Point Energy

In above discussions, we have introduced how the PIMD method should be implemented. From the corresponding PIMD simulations, one can estimate the statistical expectation value of a physical quantity at a finite temperature using Eq. 7.25. The result of such an evaluation is the expectation value of this quantity in the poly-atomic system at a finite T, with the QNEs rigorously addressed on the same footing as the thermal ones. From our discussions in Chapter 5, we know that the expectation value of the same physical quantity can also be calculated in a MD simulation, with only the thermal nuclear effects taken into account. Therefore, by comparing the results obtained from these two simulations, one can evaluate the impact of QNEs on this physical quantity in a very clean manner.

Besides these quantities which can be evaluated using Eq. 7.25, e.g. the radial distribution function [323, 338, 345], the intra- and inter-molecular bond length distributions [286, 321] etc., there are also some physical quantities in which the evaluation of their expectation values from the PIMD simulations contains some subtleties. The internal energy is such an example. As a matter of fact, this internal energy at finite temperatures is among the most concerned quantities in molecular simulations. A comparison between this quantity from the PIMD and MD simulations at different temperatures and then an extrapolation of their differences toward 0 K can give us the nuclear zero-point energy in a real poly-atomic system, beyond the often used harmonic approximation. This zero-point energy is of primary concern in studies of many problems, whose value otherwise must be calculated from very expensive quantum Monte-Carlo simulations (normally with a force-field treatment of the inter-atomic nuclear interactions, see e.g. Refs. [346, 347, 348, 349]). As mentioned before, for large poly-atomic systems, such quantum Monte-Carlo simulations might not be applicable. Therefore, the PIMD simulation in principle gives us a useful estimator for this key physical quantity in practical calculations of poly-atomic systems.

To understand how this purpose is fulfilled, we first go back to the original definition of the internal energy in statistical mechanics, which is

$$\langle E \rangle = -\frac{1}{Z^{\mathrm{Q}}} \frac{\partial Z^{\mathrm{Q}}}{\partial \beta}. \tag{7.52}$$

Here, Z^{Q} is the partition function of the quantum poly-atomic system, whose expression can be given in different ways, e.g. Eq. 7.20 in the limit of $P \to \infty$ and

Eq. 7.17, etc. We take its expression in Eq. 7.20 and rewrite it as:

$$\begin{aligned} Z^{\mathrm{Q}} &= \lim_{P\to\infty} C \int\cdots\int e^{-\beta\left\{\sum_{j=1}^{N}\sum_{i=1}^{P}\left[\frac{(\mathbf{p}_i^j)^2}{2M_i^j}+\frac{1}{2}m_j\omega_P^2\left(\mathbf{x}_i^j-\mathbf{x}_{i-1}^j\right)^2\right]+\sum_{i=1}^{P}\frac{1}{P}V(\mathbf{x}_i^1,\cdots,\mathbf{x}_i^N)\right\}} \\ &\qquad d\mathbf{x}_1\cdots d\mathbf{x}_P d\mathbf{p}_1\cdots\mathbf{p}_P \\ &= \lim_{P\to\infty} C \int\cdots\int e^{\sum_{j=1}^{N}\sum_{i=1}^{P}\left[-\beta\frac{(\mathbf{p}_i^j)^2}{2M_i^j}-\frac{1}{\beta}\frac{P}{2\hbar^2}m_j\left(\mathbf{x}_i^j-\mathbf{x}_{i-1}^j\right)^2\right]-\sum_{i=1}^{P}\beta\frac{1}{P}V(\mathbf{x}_i^1,\cdots,\mathbf{x}_i^N)} \\ &\qquad d\mathbf{x}_1\cdots d\mathbf{x}_P d\mathbf{p}_1\cdots\mathbf{p}_P \end{aligned} \tag{7.53}$$

Using this expression of the quantum partition function, an expansion of Eq. 7.52 easily gives us:

$$\begin{aligned} \langle E\rangle &= \lim_{P\to\infty}\frac{C}{Z^{\mathrm{Q}}}\int\cdots\int\left\{\sum_{j=1}^{N}\sum_{i=1}^{P}\left[\frac{(\mathbf{p}_i^j)^2}{2M_i^j}-\frac{1}{\beta^2}\frac{P}{2\hbar^2}m_j\left(\mathbf{x}_i^j-\mathbf{x}_{i-1}^j\right)^2\right]+\sum_{i=1}^{P}\frac{1}{P}V(\mathbf{x}_i^1,\cdots,\mathbf{x}_i^N)\right\} \\ &\qquad e^{-\beta\sum_{j=1}^{N}\sum_{i=1}^{P}\left[\frac{(\mathbf{p}_i^j)^2}{2M_i^j}+\frac{1}{2}m_j\omega_P^2\left(\mathbf{x}_i^j-\mathbf{x}_{i-1}^j\right)^2\right]-\sum_{i=1}^{P}\beta\frac{1}{P}V(\mathbf{x}_i^1,\cdots,\mathbf{x}_i^N)} d\mathbf{x}_1\cdots d\mathbf{x}_P d\mathbf{p}_1\cdots\mathbf{p}_P \\ &= \lim_{P\to\infty}\frac{C}{Z^{\mathrm{Q}}}\int\cdots\int\left\{\sum_{j=1}^{N}\sum_{i=1}^{P}\left[\frac{(\mathbf{p}_i^j)^2}{2M_i^j}-\frac{1}{2}m_j\omega_P^2\left(\mathbf{x}_i^j-\mathbf{x}_{i-1}^j\right)^2\right]+\sum_{i=1}^{P}\frac{1}{P}V(\mathbf{x}_i^1,\cdots,\mathbf{x}_i^N)\right\} \\ &\qquad e^{-\beta\sum_{j=1}^{N}\sum_{i=1}^{P}\left[\frac{(\mathbf{p}_i^j)^2}{2M_i^j}+\frac{1}{2}m_j\omega_P^2\left(\mathbf{x}_i^j-\mathbf{x}_{i-1}^j\right)^2\right]-\sum_{i=1}^{P}\beta\frac{1}{P}V(\mathbf{x}_i^1,\cdots,\mathbf{x}_i^N)} d\mathbf{x}_1\cdots d\mathbf{x}_P d\mathbf{p}_1\cdots\mathbf{p}_P. \end{aligned} \tag{7.54}$$

Now, if we define

$$E=\sum_{j=1}^{N}\sum_{i=1}^{P}\left[\frac{(\mathbf{p}_i^j)^2}{2M_i^j}-\frac{1}{2}m_j\omega_P^2\left(\mathbf{x}_i^j-\mathbf{x}_{i-1}^j\right)^2\right]+\sum_{i=1}^{P}\frac{1}{P}V(\mathbf{x}_i^1,\cdots,\mathbf{x}_i^N), \tag{7.55}$$

Eq. 7.54 can be further rewritten as:

$$\langle E\rangle = \lim_{P\to\infty}\frac{\int\cdots\int E e^{-\beta\sum_{j=1}^{N}\sum_{i=1}^{P}\left[\frac{(\mathbf{p}_i^j)^2}{2M_i^j}+\frac{1}{2}m_j\omega_P^2\left(\mathbf{x}_i^j-\mathbf{x}_{i-1}^j\right)^2\right]-\sum_{i=1}^{P}\beta\frac{1}{P}V(\mathbf{x}_i^1,\cdots,\mathbf{x}_i^N)} d\mathbf{x}_1\cdots d\mathbf{x}_P d\mathbf{p}_1\cdots\mathbf{p}_P}{\int\cdots\int e^{-\beta\sum_{j=1}^{N}\sum_{i=1}^{P}\left[\frac{(\mathbf{p}_i^j)^2}{2M_i^j}+\frac{1}{2}m_j\omega_P^2\left(\mathbf{x}_i^j-\mathbf{x}_{i-1}^j\right)^2\right]-\sum_{i=1}^{P}\beta\frac{1}{P}V(\mathbf{x}_i^1,\cdots,\mathbf{x}_i^N)} d\mathbf{x}_1\cdots d\mathbf{x}_P d\mathbf{p}_1\cdots\mathbf{p}_P}. \tag{7.56}$$

Therefore, the instantaneous quantity E as defined in Eq. 7.55 becomes the quantity whose ensemble average should be evaluated in the PIMD simulation. From Eq. 7.56, we see that this ensemble average gives the internal energy of the poly-atomic system, in which all QNEs are included. The minus sign in front of the second term in the quantity in Eq. 7.55 to be averaged during the simulation originates from the

temperature dependent of the spring constant in the Hamiltonian of the fictitious polymer. In a simpler form of the ensemble averages at a finite T in molecular dynamics, the expectation value of the internal energy can be further reformed as:

$$\langle E\rangle = \frac{3NP}{2\beta} - \langle\sum_{j=1}^{N}\sum_{i=1}^{P}\frac{1}{2}m_j\omega_P^2\left(\mathbf{x}_i^j - \mathbf{x}_{i-1}^j\right)^2\rangle + \langle\sum_{i=1}^{P}\frac{1}{P}V(\mathbf{x}_i^1,\cdots,\mathbf{x}_i^N)\rangle. \quad (7.57)$$

From this estimator, it is easy to see that the kinetic energy (first term) and the spring potential (second term) both scale linearly with the number of beads P in a finite temperature PIMD simulation. Therefore, with the increase of P, these two quantities go to large values. Fortunately, due to the minus sign in front of the second term, the difference between them converges with P and the zero-point energy of a poly-atomic system can be evaluated with Eq. 7.57 in practical PIMD simulations. However, we note that large fluctuations on these two quantities still remain at large P. As a consequence, for highly quantum systems in which a large P must be used in order for an accurate simulation of the QNEs, a loss of precision might exist [97, 350]. An alternative estimator, in which all terms involved converge with P, is highly desired.

To circumvent this problem, a path-integral version of the virial theorem had been introduced by Herman *et al.* in 1982, where an estimator of the internal energy which suffers much less from these fluctuations was proposed [350, 351]. For a clear explanation of how this works, we first go back to the original quantum partition function in Eq. 7.17, where no artificial kinetic energy for the molecular dynamics simulations is introduced and the integration goes only through the configuration-space (composed by the $\mathbf{x}_i^j$s) instead of the phase space (composed by the $\mathbf{x}_i^j$s and $\mathbf{p}_i^j$s). Using the periodic boundary condition of the path-integral sampling, this equation can be rewritten as:

$$Z^{\mathrm{Q}} = \lim_{P\to\infty}\left(\frac{mP}{2\beta\pi\hbar^2}\right)^{\frac{P}{2}}\int_V\int_V\cdots\int_V e^{-\beta V^{\mathrm{eff}}(\mathbf{x}_1,\mathbf{x}_2,\cdots,\mathbf{x}_P)}d\mathbf{x}_1 d\mathbf{x}_2\cdots d\mathbf{x}_P, \quad (7.58)$$

where

$$V^{\mathrm{eff}}(\mathbf{x}_1,\mathbf{x}_2,\cdots,\mathbf{x}_P) = \sum_{i=1}^{P}\sum_{j=1}^{N}\left[\frac{1}{2}m_j\omega_P^2\left(\mathbf{x}_i^j - \mathbf{x}_{i-1}^j\right)^2\right] + \sum_{i=1}^{P}\frac{1}{P}V(\mathbf{x}_i^1,\cdots,\mathbf{x}_i^N). \quad (7.59)$$

Same as what we have used for the nomenclature before, $(\mathbf{x}_1,\mathbf{x}_2,\cdots,\mathbf{x}_P)$ all together represents the spatial configuration of the artificial polymer. $\mathbf{x}_i$ is composed by $(\mathbf{x}_i^1,\cdots,\mathbf{x}_i^N)$. It means the spatial configuration of the poly-atomic system at its i^{th} image. The key point of the virial internal energy estimator is that the first two

terms in Eq. 7.57 is replaced by the mean kinetic energy of the quantum system, as:

$$\frac{3NP}{2\beta} - \langle \sum_{j=1}^{N}\sum_{i=1}^{P} \frac{1}{2} m_j \omega_P^2 \left(\mathbf{x}_i^j - \mathbf{x}_{i-1}^j\right)^2 \rangle = \langle \frac{1}{2P} \sum_{j=1}^{N}\sum_{i=1}^{P} \mathbf{x}_i^j \cdot \frac{\partial V(\mathbf{x}_i^1, \cdots, \mathbf{x}_i^N)}{\partial \mathbf{x}_i^j} \rangle, \quad (7.60)$$

With this treatment, the expectation value of the internal energy in Eq. 7.57 reforms into:

$$\langle E \rangle = \langle \frac{1}{2P} \sum_{j=1}^{N}\sum_{i=1}^{P} \mathbf{x}_i^j \cdot \frac{\partial V(\mathbf{x}_i^1, \cdots, \mathbf{x}_i^N)}{\partial \mathbf{x}_i^j} \rangle + \langle \sum_{i=1}^{P} \frac{1}{P} V(\mathbf{x}_i^1, \cdots, \mathbf{x}_i^N) \rangle. \quad (7.61)$$

Here, you can see that neither of the two terms being evaluated in the PIMD simulation scales with P. Therefore, a smaller fluctuation of the internal energy to be evaluated in the PIMD simulations should be expected.

To understand how the equality in Eq. 7.60 exists, we use the partition function in Eq. 7.58 to evaluate the quantity on the right hand side Eq. 7.60. From this partition function, the ensemble average of this quantity equals:

$$\begin{aligned} &\langle \frac{1}{2P} \sum_{j=1}^{N}\sum_{i=1}^{P} \mathbf{x}_i^j \cdot \frac{\partial V(\mathbf{x}_i^1, \cdots, \mathbf{x}_i^N)}{\partial \mathbf{x}_i^j} \rangle \\ &= \frac{\int_V \cdots \int_V \left[\frac{1}{2} \sum_{j=1}^{N} \sum_{i=1}^{P} \mathbf{x}_i^j \cdot \frac{\partial \frac{1}{P} V(\mathbf{x}_i^1, \cdots, \mathbf{x}_i^N)}{\partial \mathbf{x}_i^j} \right] e^{-\beta V^{\text{eff}}(\mathbf{x}_1, \mathbf{x}_2, \cdots, \mathbf{x}_P)} d\mathbf{x}_1 d\mathbf{x}_2 \cdots d\mathbf{x}_P}{\int_V \cdots \int_V e^{-\beta V^{\text{eff}}(\mathbf{x}_1, \mathbf{x}_2, \cdots, \mathbf{x}_P)} d\mathbf{x}_1 d\mathbf{x}_2 \cdots d\mathbf{x}_P}. \end{aligned} \quad (7.62)$$

Here, the relation between $\frac{1}{P} V(\mathbf{x}_i^1, \cdots, \mathbf{x}_i^N)$ and $V^{\text{eff}}(\mathbf{x}_1, \cdots, \mathbf{x}_P)$ is given by Eq. 7.59. Now, if we label

$$\alpha(\mathbf{x}_1, \mathbf{x}_2, \cdots, \mathbf{x}_P) = \sum_{i=1}^{P}\sum_{j=1}^{N} \frac{1}{2} m_j \omega_P^2 \left(\mathbf{x}_i^j - \mathbf{x}_{i-1}^j\right)^2, \quad (7.63)$$

and

$$\lambda(\mathbf{x}_1, \mathbf{x}_2, \cdots, \mathbf{x}_P) = \sum_{i=1}^{P} \frac{1}{P} V(\mathbf{x}_i^1, \mathbf{x}_i^2, \cdots, \mathbf{x}_i^N), \quad (7.64)$$

then Eq. 7.59 will be reformed into:

$$V^{\text{eff}}(\mathbf{x}_1, \mathbf{x}_2, \cdots, \mathbf{x}_P) = \alpha(\mathbf{x}_1, \mathbf{x}_2, \cdots, \mathbf{x}_P) + \lambda(\mathbf{x}_1, \mathbf{x}_2, \cdots, \mathbf{x}_P). \quad (7.65)$$

And Eq. 7.62 reforms to:

$$\begin{aligned}
&\langle \frac{1}{2P}\sum_{j=1}^{N}\sum_{i=1}^{P}\mathbf{x}_i^j\cdot\frac{\partial V(\mathbf{x}_i^1,\cdots,\mathbf{x}_i^N)}{\partial \mathbf{x}_i^j}\rangle \\
&=\frac{\int_V\cdots\int_V\left[\frac{1}{2}\sum_{j=1}^{N}\sum_{i=1}^{P}\mathbf{x}_i^j\cdot\frac{\partial V^{\text{eff}}(\mathbf{x}_1,\cdots,\mathbf{x}_P)}{\partial \mathbf{x}_i^j}\right]e^{-\beta V^{\text{eff}}(\mathbf{x}_1,\mathbf{x}_2,\cdots,\mathbf{x}_P)}d\mathbf{x}_1d\mathbf{x}_2\cdots d\mathbf{x}_P}{\int_V\cdots\int_V e^{-\beta V^{\text{eff}}(\mathbf{x}_1,\mathbf{x}_2,\cdots,\mathbf{x}_P)}d\mathbf{x}_1d\mathbf{x}_2\cdots d\mathbf{x}_P} \\
&\quad-\frac{\int_V\cdots\int_V\left[\frac{1}{2}\sum_{j=1}^{N}\sum_{i=1}^{P}\mathbf{x}_i^j\cdot\frac{\partial \alpha(\mathbf{x}_1,\cdots,\mathbf{x}_P)}{\partial \mathbf{x}_i^j}\right]e^{-\beta V^{\text{eff}}(\mathbf{x}_1,\mathbf{x}_2,\cdots,\mathbf{x}_P)}d\mathbf{x}_1d\mathbf{x}_2\cdots d\mathbf{x}_P}{\int_V\cdots\int_V e^{-\beta V^{\text{eff}}(\mathbf{x}_1,\mathbf{x}_2,\cdots,\mathbf{x}_P)}d\mathbf{x}_1d\mathbf{x}_2\cdots d\mathbf{x}_P}.
\end{aligned} \tag{7.66}$$

For a further evaluation of this quantity, we first make use of an important property of $\alpha(\mathbf{x}_1,\cdots,\mathbf{x}_P)$ that it is a homogeneous function of $(\mathbf{x}_1,\cdots,\mathbf{x}_P)$ of degree 2, so that the following equation exists:

$$\sum_{j=1}^{N}\sum_{i=1}^{P}\mathbf{x}_i^j\cdot\frac{\partial \alpha(\mathbf{x}_1,\cdots,\mathbf{x}_P)}{\partial \mathbf{x}_i^j}=2\alpha(\mathbf{x}_1,\cdots,\mathbf{x}_P). \tag{7.67}$$

Therefore, the second term on the right hand side of Eq. 7.66 equals

$$\begin{aligned}
&-\frac{\int_V\cdots\int_V\left[\frac{1}{2}\sum_{j=1}^{N}\sum_{i=1}^{P}\mathbf{x}_i^j\cdot\frac{\partial \alpha(\mathbf{x}_1,\cdots,\mathbf{x}_P)}{\partial \mathbf{x}_i^j}\right]e^{-\beta V^{\text{eff}}(\mathbf{x}_1,\mathbf{x}_2,\cdots,\mathbf{x}_P)}d\mathbf{x}_1d\mathbf{x}_2\cdots d\mathbf{x}_P}{\int_V\cdots\int_V e^{-\beta V^{\text{eff}}(\mathbf{x}_1,\mathbf{x}_2,\cdots,\mathbf{x}_P)}d\mathbf{x}_1d\mathbf{x}_2\cdots d\mathbf{x}_P} \\
&=-\frac{\int_V\cdots\int_V\alpha(\mathbf{x}_1,\cdots,\mathbf{x}_P)e^{-\beta V^{\text{eff}}(\mathbf{x}_1,\mathbf{x}_2,\cdots,\mathbf{x}_P)}d\mathbf{x}_1d\mathbf{x}_2\cdots d\mathbf{x}_P}{\int_V\cdots\int_V e^{-\beta V^{\text{eff}}(\mathbf{x}_1,\mathbf{x}_2,\cdots,\mathbf{x}_P)}d\mathbf{x}_1d\mathbf{x}_2\cdots d\mathbf{x}_P}=\langle\alpha(\mathbf{x}_1,\cdots,\mathbf{x}_P)\rangle \\
&=-\langle\sum_{j=1}^{N}\sum_{i=1}^{P}\frac{1}{2}m_j\omega_P^2\left(\mathbf{x}_i^j-\mathbf{x}_{i-1}^j\right)^2\rangle.
\end{aligned} \tag{7.68}$$

And Eq. 7.66 further evolves to

$$\begin{aligned}
&\langle \frac{1}{2P}\sum_{j=1}^{N}\sum_{i=1}^{P}\mathbf{x}_i^j\cdot\frac{\partial V(\mathbf{x}_i^1,\cdots,\mathbf{x}_i^N)}{\partial \mathbf{x}_i^j}\rangle \\
&=\frac{\int_V\cdots\int_V\left[\frac{1}{2}\sum_{j=1}^{N}\sum_{i=1}^{P}\mathbf{x}_i^j\cdot\frac{\partial V^{\text{eff}}(\mathbf{x}_1,\cdots,\mathbf{x}_P)}{\partial \mathbf{x}_i^j}\right]e^{-\beta V^{\text{eff}}(\mathbf{x}_1,\mathbf{x}_2,\cdots,\mathbf{x}_P)}d\mathbf{x}_1d\mathbf{x}_2\cdots d\mathbf{x}_P}{\int_V\cdots\int_V e^{-\beta V^{\text{eff}}(\mathbf{x}_1,\mathbf{x}_2,\cdots,\mathbf{x}_P)}d\mathbf{x}_1d\mathbf{x}_2\cdots d\mathbf{x}_P} \\
&\quad-\langle\sum_{j=1}^{N}\sum_{i=1}^{P}\frac{1}{2}m_j\omega_P^2\left(\mathbf{x}_i^j-\mathbf{x}_{i-1}^j\right)^2\rangle.
\end{aligned} \tag{7.69}$$

Comparing Eq. 7.69 with Eq. 7.60, the only equality we need to prove becomes:

$$\frac{\int_V \cdots \int_V \left[\frac{1}{2}\sum_{j=1}^{N}\sum_{i=1}^{P} \mathbf{x}_i^j \cdot \frac{\partial V^{\text{eff}}(\mathbf{x}_1,\cdots,\mathbf{x}_P)}{\partial \mathbf{x}_i^j}\right] e^{-\beta V^{\text{eff}}(\mathbf{x}_1,\mathbf{x}_2,\cdots,\mathbf{x}_P)} d\mathbf{x}_1 d\mathbf{x}_2 \cdots d\mathbf{x}_P}{\int_V \cdots \int_V e^{-\beta V^{\text{eff}}(\mathbf{x}_1,\mathbf{x}_2,\cdots,\mathbf{x}_P)} d\mathbf{x}_1 d\mathbf{x}_2 \cdots d\mathbf{x}_P} = \frac{3NP}{2\beta}. \tag{7.70}$$

This proof is doable if we reform the left hand side of Eq. 7.70 in the following matter:

$$\begin{aligned} &\frac{\int_V \cdots \int_V \left[\frac{1}{2}\sum_{j=1}^{N}\sum_{i=1}^{P} \mathbf{x}_i^j \cdot \frac{\partial V^{\text{eff}}(\mathbf{x}_1,\cdots,\mathbf{x}_P)}{\partial \mathbf{x}_i^j}\right] e^{-\beta V^{\text{eff}}(\mathbf{x}_1,\mathbf{x}_2,\cdots,\mathbf{x}_P)} d\mathbf{x}_1 d\mathbf{x}_2 \cdots d\mathbf{x}_P}{\int_V \cdots \int_V e^{-\beta V^{\text{eff}}(\mathbf{x}_1,\mathbf{x}_2,\cdots,\mathbf{x}_P)} d\mathbf{x}_1 d\mathbf{x}_2 \cdots d\mathbf{x}_P} \\ =& -\frac{1}{\beta}\frac{\int_V \cdots \int_V \frac{1}{2}\sum_{j=1}^{N}\sum_{i=1}^{P} \mathbf{x}_i^j \cdot \left[\frac{\partial}{\partial \mathbf{x}_i^j} e^{-\beta V^{\text{eff}}(\mathbf{x}_1,\mathbf{x}_2,\cdots,\mathbf{x}_P)}\right] d\mathbf{x}_1 d\mathbf{x}_2 \cdots d\mathbf{x}_P}{\int_V \cdots \int_V e^{-\beta V^{\text{eff}}(\mathbf{x}_1,\mathbf{x}_2,\cdots,\mathbf{x}_P)} d\mathbf{x}_1 d\mathbf{x}_2 \cdots d\mathbf{x}_P}. \end{aligned} \tag{7.71}$$

Then, making use of an integration by parts, this quantity further evolves into:

$$\begin{aligned} &-\frac{1}{\beta}\frac{\int_V \cdots \int_V \frac{1}{2}\sum_{j=1}^{N}\sum_{i=1}^{P} \mathbf{x}_i^j \cdot \left[\frac{\partial}{\partial \mathbf{x}_i^j} e^{-\beta V^{\text{eff}}(\mathbf{x}_1,\mathbf{x}_2,\cdots,\mathbf{x}_P)}\right] d\mathbf{x}_1 d\mathbf{x}_2 \cdots d\mathbf{x}_P}{\int_V \cdots \int_V e^{-\beta V^{\text{eff}}(\mathbf{x}_1,\mathbf{x}_2,\cdots,\mathbf{x}_P)} d\mathbf{x}_1 d\mathbf{x}_2 \cdots d\mathbf{x}_P} \\ =&\frac{1}{\beta}\frac{\int_V \cdots \int_V \frac{1}{2}\sum_{j=1}^{N}\sum_{i=1}^{P} e^{-\beta V^{\text{eff}}(\mathbf{x}_1,\mathbf{x}_2,\cdots,\mathbf{x}_P)} \left[\frac{\partial}{\partial \mathbf{x}_i^j} \cdot \mathbf{x}_i^j\right] d\mathbf{x}_1 d\mathbf{x}_2 \cdots d\mathbf{x}_P}{\int_V \cdots \int_V e^{-\beta V^{\text{eff}}(\mathbf{x}_1,\mathbf{x}_2,\cdots,\mathbf{x}_P)} d\mathbf{x}_1 d\mathbf{x}_2 \cdots d\mathbf{x}_P} = \frac{1}{\beta}\frac{3NP}{2}. \end{aligned} \tag{7.72}$$

With these, the equality in Eq. 7.60 is proven and one can use the virial estimator as given in Eq. 7.61 to calculate the finite-temperature internal energy of the polyatomic system under investigation. In practice, a slight variation of Eq. 7.61 is often used. This variation is based on the following equation:

$$\begin{aligned} &\langle \frac{1}{2P}\sum_{j=1}^{N}\sum_{i=1}^{P} \mathbf{x}_i^j \cdot \frac{\partial V(\mathbf{x}_i^1,\cdots,\mathbf{x}_i^N)}{\partial \mathbf{x}_i^j} \rangle \\ &= \langle \frac{1}{2P}\sum_{j=1}^{N}\sum_{i=1}^{P} \mathbf{x}_{\text{c}}^j \cdot \frac{\partial V(\mathbf{x}_i^1,\cdots,\mathbf{x}_i^N)}{\partial \mathbf{x}_i^j} \rangle + \langle \frac{1}{2P}\sum_{j=1}^{N}\sum_{i=1}^{P} (\mathbf{x}_i^j - \mathbf{x}_{\text{c}}^j) \cdot \frac{\partial V(\mathbf{x}_i^1,\cdots,\mathbf{x}_i^N)}{\partial \mathbf{x}_i^j} \rangle \\ &= \langle \frac{1}{2}\sum_{j=1}^{N} \mathbf{x}_{\text{c}}^j \cdot \mathbf{F}_{\text{c}}^j \rangle + \langle \frac{1}{2P}\sum_{j=1}^{N}\sum_{i=1}^{P} (\mathbf{x}_i^j - \mathbf{x}_{\text{c}}^j) \cdot \frac{\partial V(\mathbf{x}_i^1,\cdots,\mathbf{x}_i^N)}{\partial \mathbf{x}_i^j} \rangle \\ &= \frac{3N}{2\beta} + \langle \frac{1}{2P}\sum_{j=1}^{N}\sum_{i=1}^{P} (\mathbf{x}_i^j - \mathbf{x}_{\text{c}}^j) \cdot \frac{\partial V(\mathbf{x}_i^1,\cdots,\mathbf{x}_i^N)}{\partial \mathbf{x}_i^j} \rangle, \end{aligned} \tag{7.73}$$

where $\mathbf{F}_{\mathrm{c}}^{j}$ stands for the effective force imposed on the centroid of the j^{th} atom and $\mathbf{x}_{\mathrm{c}}^{j}$ stands for its centroid position. And the estimator in Eq. 7.61 further changes into:

$$\langle E\rangle = \frac{3N}{2\beta} + \langle\frac{1}{2P}\sum_{j=1}^{N}\sum_{i=1}^{P}(\mathbf{x}_i^j - \mathbf{x}_{\mathrm{c}}^j)\cdot\frac{\partial V(\mathbf{x}_i^1,\cdots,\mathbf{x}_i^N)}{\partial\mathbf{x}_i^j}\rangle + \langle\sum_{i=1}^{P}\frac{1}{P}V\left(\mathbf{x}_i^1,\cdots,\mathbf{x}_i^N\right)\rangle. \tag{7.74}$$

One can use either the estimator in Eq. 7.74 or the one in Eq. 7.57 to evaluate the internal energy in real poly-atomic systems.

We note that the internal energy calculated this way includes contribution from the QNEs. As mentioned above, a MD simulation, in which only the thermal nuclear effects are included, can also give us an expectation value of this quantity. Therefore, a comparison between results obtained from these two simulations in principle can give us the zero-point energy of a real poly-atomic system. To understand how this works in practice, we show a sketch for the evolution of the internal energy in the MD and PIMD (using different P) simulations as a function of temperature in Fig. 7.4. At 0 K, the internal energy equals the static geometry optimized total energy in the MD simulaiton. With the increase of the temperature, it increases linearly due to the classical virial theorem. In the PIMD simulations, this internal energy evolves different from the one obtained from the MD simulations, and this difference originates from the QNEs. Its value increases with the number of beads P till convergence. At higher Ts, a small value of P is good energy to describe this difference. At lower Ts, larger P is needed. At zero K, since a infinite P is needed for the path-integral sampling, the PIMD simulation lost its precision too. However, an extrapolation of the QNEs from finite T still presents a good estimator for the zero-point energy.

7.2 Extensions beyond the Statistical Studies

So far, all our discussions have been restricted to the statistics. The associated time-averaged quantities can be used to study the impact of the QNEs on the equilibrium statistical properties of a poly-atomic system under investigation at finite temperatures. Another aspect of the real quantum world, *i.e.* the dynamics, however, has never been touched. We note that descriptions of such nuclear dynamics, with relevant electronic structures computed accurately "on-the-fly", poses a "grand challenge" to both theoretical physics and chemistry. As a matter of fact, illustrations of many key physical/chemical properties in the real world, e.g. the transport properties, the chemical reaction rates, and the neutron or light scattering spectra etc., require descriptions of it. In a many-body (poly-atomic) system, we know that the key quantity in describing such dynamics is the so-called time-correlation func-

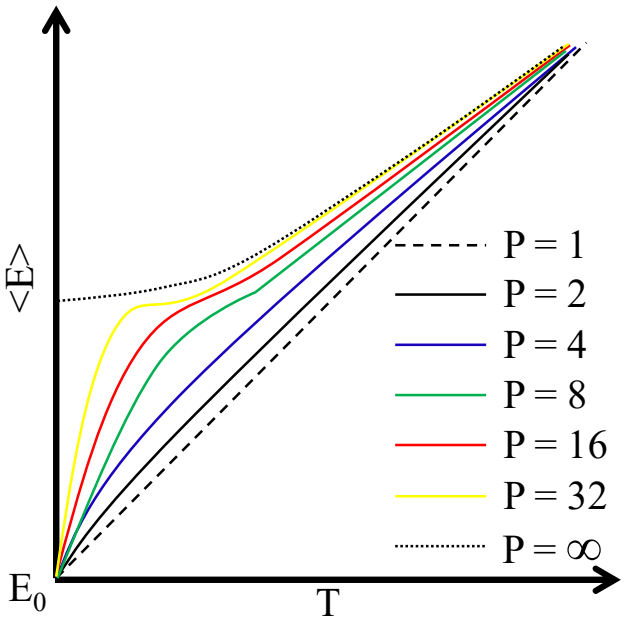

Figure 7.4: Illustration on how the internal energy's expectation value changes with temperature in the MD and PIMD simulations. In the MD simulation, as T approaches 0 K, the internal energy approaches the static geometry optimized total energy E_0. With the increase of T, it increases linearly because of thermal fluctuations. In the PIMD simulations, since the QNEs are included, at finite T, there is a difference on this value from its classical result. This difference increases with the number of beads P till convergence. At higher temperatures, a small P is already good energy to describe this difference. At lower temperatures, larger Ps are needed. At 0 K, due to the fact that a infinite P is needed for the path-integral sampling, the PIMD method also loses its power. However, an extrapolation of the difference between the internal energy obtained from the converged PIMD simulations and MD simulations at finite T still presents a good estimator for the zero-point-energy.

tion. Taking the infrared absorption spectrum as an example, it is directly related to the dipole-dipole time-correlation function of the system. The translational diffusion coefficient, on the other hand, can be understood using the velocity autocorrelation function, etc.. Because of these, inclusion of the QNEs in descriptions of such time-correlation functions becomes an issue of considerable interest in present studies in both theoretical physics and chemistry [74, 79, 91, 352, 353, 354, 355, 356, 357].

A natural choice for the calculation of such time-correlation functions resides in solving the time-dependent Schrödinger equation of the nuclei in real poly-atomic systems. This implies propagating the nuclear quantum dynamics on the Born-

Oppenheimer potential energy surfaces (BO-PES) which are pre-computed with very accurate electronic structure theories. The multi-configuration time-dependent Hartree method (MCTDH) is such an example [358, 359]. In the past years, it has been very successful in describing some gas phase chemical reactions and the dynamical properties of small molecules [60, 61, 360, 361, 362]. However, one notes that the scaling of their computational cost with system size makes it unfeasible to many practical systems quickly as the nuclear degree of freedom increases. Alternative methods in describing such nuclear dynamics, where scaling behavior is much better so that simulations can be performed in systems of relevance in practical studies, must be resorted to.

7.2.1 Different Semiclassical Dynamical Methods

Similar to the route we have chosen in studies of the statistical mechanics, now we resort to the path-integral representation of the quantum mechanics. Within this picture, the most rigorous method in quantifying such a time-correlation function naturally resides in using a complex-time path-integral sampling technique [67, 74]. In this method, the thermal effects are treated as imaginary time in the complex-time space and the real-time axis takes care of the dynamics. Extension of the path-integral equations from statistics to dynamics is straightforward [74]. However, different from the success of PIMD/PIMC techniques in addressing the statistical properties in simulations of real poly-atomic systems, practical simulations based on such extension of the path-integral sampling methods to the complex-time space has continued to be problematic, due to an extensive phase cancellation originating from the paths with weight that are non-positive in character [78, 79]. In spite of these difficulties, by defining a symmetrized time-correlation function that lends itself to PIMD/PIMC simulations, significant progress has still been made over the last 30 years within this complex-time path-integral scheme [75, 76, 77]. As a prominent example, in a recent development of this method by Nakayama and Makri for studies of the subcritical liquid para-hydrogen, the authors have shown that accurate quantum mechanical results for the initial 0.2 ps segment of the symmetrized velocity autocorrelation function, as well as the incoherent dynamic structure factor at certain momentum transfer values at moderate temperatures and densities, can be obtained [352]. But for more general problems involving longer time dynamics and more complicated systems with higher density, which is clearly of more practical use, this method becomes less practical and one needs to resort to less accurate quantum dynamical methods.

Following the summary by Braams and Manolopoulos [91], here we categorize these less accurate quantum dynamical methods that have been applied to condensed matter systems essentially into three classes, noting that each method has its own strengths and weaknesses. The first class of methods simulate the system using

imaginary time propagator only. Then, an inverse Wick rotation is used to infer the thermodynamically averaged real time-correlation function from the imaginary-time one based on the Baym-Mermin theorem [363]. This trick is similar to the analytical continuation of the self-energy from the imaginary frequency axis to the real frequency one for the calculation of the quasi-particle energies as introduced in Sec. 4.4.5. There are two practical schemes for the time-correlation function to be calculated, *i.e.* the numerical analytic continuation (NAC) [75, 76, 77, 364, 365, 366, 367] and the quantum mode-coupling theory (QMCT) [368, 369, 370, 371, 372, 373]. The advantage of these methods is that the short-time behavior of the time-correlation function can normally be described accurately and the imaginary-time treatment makes the correlation function easy to compute. However, we note that the numerical stability of the analytical continuation is much worse than its counterparts in the calculation of the self-energies. Some standard methods, such as the Padé technique, are of limited use in practice [374, 375]. Plus, these methods are not exact at the classical limit.

The second class of methods combine an exact treatment of the quantum Boltzmann operator with an approximate treatment of the real-time evolution based on classical dynamics. These methods include the linearized semiclassical initial value representation (LSC-IVR) method (see e.g. Refs. [376, 377] by Wang, Sun, Miller, Refs. [355, 356] by Shi and Geva, and Refs. [378, 379] by Liu and Miller, etc.), the Feynman-Kleinert linearized path-integral (FK-LPT) method (see e.g. Refs. [380, 381, 382, 383] by Poulsen, Nyman, and Rossky, etc.), and the forward-backward semiclassical dynamics (FB-SD) (see e.g. Refs. [353, 354] by Shao and Makri, and Ref. [357] by Liu and Makri, etc.). Their main advantage is that they are exact in three important limits, *i.e.*, the short-time limit, the limit of a harmonic potential, and the classical limit. While a main disadvantage is that the classical trajectories don't in general conserve the quantum mechanical equilibrium distribution functions [91].

The third class of methods, which normally combine an exact treatment of the quantum Boltzmann operator with an approximate treatment of the real-time evolution based on a "modified" version of the classical mechanics, include the so-called centroid molecular dynamics (CMD) by Cao and Voth [80, 81, 82, 83, 84, 384] and the ring-polymer molecular dynamics (RPMD) by Manolopoulos and his coworkers [85, 86, 87, 88, 89, 90, 91, 92, 93]. A key difference between these two methods and those in the earlier two classes is that mathematically they are only slight modifications on the standard PIMD method as we have introduced in Sec. 7.1, although conceptually these differences are fundamental. And they all originate from generalizations of the physical concepts implied in the PIMD simulations, with the CMD method appears earlier. Therefore, in the following we will give a detailed explanation of these two methods in a chronological order with a special focus on their similarities and differences with the normal statistical PIMD simulations, starting

from a precursor of the CMD method, *i.e.* Gillan's generalization of Feynman's path centroid concept to its applications in the transition state theory (TST).

7.2.2 Centroid Molecular Dynamics and Ring-Polymer Molecular Dynamics

In the seminal book by Feynman and Hibbs [67], it has been shown that the concept of path centroid can be used to interpret the impact of quantum effects on the effective potential the particle under investigation feels. Later, this concept was extended by Feynman and Kleinert so that we have an effective centroid potential [385], which is of practical use in molecular simulations. As one example, Gillan has employed it in calculating the probability of finding a quantum particle at its transition state during a rare-event transition process, which could be used later to describe the transition rate between two stable states at the quantum mechanical level, see e.g. Refs. [386, 387]. We note that theories behind characterizing such transition rates of slow processes, such as the chemical reactions and the diffusion events, are the so-called TSTs. It is both statistical and dynamical in the sense that a statistical property (the probability of finding the system at its transition state) is assumed to be proportional to a dynamical property (the transition rate). Due to this fundamental assumption, theories behind characterizing this probability of finding the system in its transition state lies at the heart the TST.

Already at the static level, searching for this transition state is non-trivial in a poly-atomic system, due to the high-dimensional feature of the BO PES associated with the nuclear degrees of freedom. Currently, there are several schemes in which such a hunting can be carried out, including the Constrained Optimization (CO) [19], Nudged Elastic Band (NEB) [20, 21, 22], Dewar, Healy and Stewart (DHS) [23], Dimer [24, 25, 26], Activation-Relaxation Technique (ART) [27, 28] and One-side Growing String (OGS) [29] as well as their various combinations. Here, we suppose that a reasonable estimation of the transition state and its associated hyperplane separating the reactant and product states is already done. Our discussions only concern further thermal and quantum nuclear effects on the static energies based on this knowledge.

At the classical level, suppose that we have a well-defined reaction coordinate s, which properly separates the reactant and product states. According to the TST, the transition rate is:

$$k_{\mathrm{TST}} = \frac{\langle v_{\perp} \rangle}{2\delta} \frac{Z^{\mathrm{T}} \delta}{Z} = \frac{\langle v_{\perp} \rangle}{2} \frac{Z^{\mathrm{T}}}{Z}, \tag{7.75}$$

where δ is defined as the interval for the reaction coordinate s with which we think that the system is at the transition state. With this definition, $Z^{\mathrm{T}}\delta/Z$ stands for the probability of finding the system at the transition state while $\langle v_{\perp} \rangle/(2\delta)$ stands for the escape rate from the transition state. Putting these two factors together,

one obtains a transition rate through the transition state from the reactant to the produce, which is sensitive to the choice of the "transition state". One notes that this estimation of the transition rate with the TST in Eq. 7.75 sets the upper bound for the real transition rate [331], since moving the "transition state" used here away from the real one will clearly increase Z^{T}/Z. Therefore it is highly recommended that one searches for the transition state and its associated hyperplane dividing the reactant and product states so that the estimated rate in Eq. 7.75 reaches a minimum. In so doing, one obtains the best evaluation of the transition rate. Such a variational method is called variational transition state theory (VTST) [331, 388, 389].

Then one tries to include the QNEs. There are several extensions of this TST to its quantum version [390, 391, 392, 393, 394, 395], with the simplest ones only replacing the classical statistical averaging with the quantum one. In these simplest methods, we note that the extension of the centroid's concept from the traditional statistical PIMD method is already used in calculating the free-energy difference between the reactant and the transition states. One prominent example is the work by Gillan in the 1980s [386, 387]. In this example, the probability of finding the system in the transition state compared to that in the reactant was calculated using the reversible work. In particular, a series of locations along the transition path were selected and a PIMD simulation is carried out by fixing the centroid of the path-integral chain of the transition particle at each point. In so doing, the average over all the remaining quantum degrees of freedom at this point can be properly evaluated and one obtains an effective mean-force on the centroid of the transition particle along the transition path. By integrating this effective force along the transition path using reversible work, one gets the free-energy difference between the reactant and the transition states. The relative density of the centroid at this transition state is then calculated using this free-energy difference and by assuming that the transition rate is proportional to this relative density one finally gets the transition rate.

Following this idea that an effective forces on the centroids of the quantum particles can be calculated by fixing the centroid positions and doing statistics over all other quantum degrees of freedom, the CMD method was introduced by Cao and Voth in 1993 as an approximate method to compute the real-time quantum correlation function for the dynamical properties of a real poly-atomic system to be described [384]. The central point of this CMD method is the assumption that the real-time evolution of the centroid positions on their potential of mean force (PMF) surface can be used to generate approximate quantum dynamical properties of real poly-atomic systems. Their evolution respects the Newton equations:

$$\begin{aligned} \dot{\mathbf{x}}_{\mathrm{c}}^{j} &= \frac{\mathbf{p}_{\mathrm{c}}^{j}}{m}, \\ \dot{\mathbf{p}}_{\mathrm{c}}^{j} &= F^{j}(\mathbf{x}_{\mathrm{c}}), \end{aligned} \tag{7.76}$$

where j again runs through the atomic index, $\mathbf{x}_c$ represents a spatial configuration of the centroids and $\mathbf{x}_c^j$ means the centroid position of the j^{th} atom. $F^j(\mathbf{x}_c)$ is the derivative of potential of mean force surface with respect to $\mathbf{x}_c^j$, *i.e.* the mean field centroid force at $\mathbf{x}_c$. It is mathematically defined as:

$$F^j(\mathbf{x}_c) = \frac{\int\int d\mathbf{x}_1 \cdots d\mathbf{x}_P \delta(\mathbf{x}_0 - \mathbf{x}_c) F_0^j(\mathbf{x}_c) e^{-\beta V^{\text{eff}}(\mathbf{x}_1, \cdots, \mathbf{x}_P)}}{\int\int d\mathbf{x}_1 \cdots d\mathbf{x}_P \delta(\mathbf{x}_0 - \mathbf{x}_c) e^{-\beta V^{\text{eff}}(\mathbf{x}_1, \cdots, \mathbf{x}_P)}}. \tag{7.77}$$

Here $V^{\text{eff}}(\mathbf{x}_1, \cdots, \mathbf{x}_P)$ is the effective potential defined in Eq. 7.18 and $F_0^j(\mathbf{x}_c)$ is the instantaneous Hellmann-Feynman force imposed on the centroid, given by:

$$F_0^j(\mathbf{x}_c) = \frac{1}{P} \sum_{i=1}^{P} \frac{\partial V(\mathbf{x}_1, \cdots, \mathbf{x}_P)}{\partial \mathbf{x}_i^j}, \tag{7.78}$$

and $\mathbf{x}_0$ represents the instantaneous centroid configuration which should be restricted at $\mathbf{x}_c$. Due to this use of the Newton equations in describing the centroid propagation, this method is intrinsically a semi-classical method, with the QNEs rigorously described only at the statistical level when the mean field centroid force is calculated. However, we note that the quantum correction to the effective potential sometimes already incorporates the dominant elements of QNEs in descriptions of the nuclear dynamics and it is currently used as a standard routine to investigate the impact of QNEs on the dynamical property of real poly-atomic systems.

One point implied in the procedure described above for the CMD method is that a full statistical PIMD (or PIMC) simulation should be carried out at each centroid configuration, before it propagates to the next centroid configuration. For complex poly-atomic systems, however, this is inapplicable due to the computational cost associated. As a simplified version of this method, the adiabatic approximation can be used [396]. For a better explanation of this idea, we go back to the normal-mode coordinate as explained in Sec. 7.1.4. Mathematically, the fundamental difference between a PIMD simulation in the primitive Cartesian coordinate and in the normal-mode coordinate is that a coordinate transformation should be made at each PIMD step in order to convert the forces and the spatial configurations of the polymer, so that the forces can be calculated in the Cartesian space and the equation of motion can be propagated in the normal-mode one. The first normal-mode describes the propagation of the centroid, while the other modes describe inter-bead vibrations. When the masses used in the PIMD simulation is chosen according to Eq. 7.49, one ensures that all the "artificial" inter-bead vibrations have the same frequency, whose value is determined by the constant c. Frequency associated with the centroid vibration is determined by the inter-atomic potential which is real and physical. Therefore, intuitively, one can set this constant c to a very small value so that the masses associated with the "artificial" inter-bead vibrations are small and they can

adiabatically react to the motion of the centroid. Since the centroid mode moves much slower than the other ones, during a characteristic time for its vibration which is determined by the inter-atomic potential, the other inter-bead vibrational modes can already do a very good statistical averaging over their degrees of freedom. In so doing, the potential each centroid feel upon characterizing the physical vibrations can be calculated "on-the-fly". As a cost of not doing a PIMD simulation at each centroid configuration, a much smaller time-step should be used in order to address the fast inter-bead vibrations originating from the small masses associated with them.

We note that this "on-the-fly" simplified calculation of the mean field centroid force was first proposed in Ref. [83], where different time intervals were suggested for the propagation of the centroid and the much faster inter-beads motions. In between the centroid propagation time steps, a serious of inter-bead propagations should be made subjected to the constraint in Eq. 7.77 so that a statistical averaging over the centroid force can be obtained before propagating the centroid. Therefore, different from a rigorous implementation of the CMD method, there is only one trajectory. This simplified version of the CMD method is called the adiabatic centroid molecular dynamics (ACMD) method [83]. In 2006, it is further simplified so that a single small time interval is used for the propagation of both the centroid and inter-bead vibrations [397], and the corresponding simulation is called partially adiabatic centroid molecular dynamics (PACMD) simulations [397]. We note that nowadays this PACMD method is the often used method in practical simulations of complex systems. And in practice this distinction between PACMD, ACMD, and CMD is often obviated and one simply refer to PACMD as CMD [398]. Here we follow such a tradition and refer PACMD as CMD in later discussions.

Now we look at the differences between the statistical PIMD and the dynamical CMD simulations. For this comparison to be as simple as possible, we use the normal-mode coordinate for the PIMD simulations. In statistical normal-mode PIMD simulations, the constant c in Eq. 7.49 is set as one and the time step is determined by the frequency of real inter-atomic vibrations. While in a CMD simulation, since the inter-bead vibrations have much higher frequency due to their small artificial masses, this c takes a small value between zero and one, and a much smaller time step than that of the inter-atomic vibrations should be used to ensure the adiabatic approximation works. For the thermostating strategy, each mode should be coupled to an efficient thermostat in both cases. Therefore, mathematically these two simulations are very similar, although conceptually they are fundamentally different.

Then we compare the CMD method with the more recently proposed RPMD [85, 86, 87, 88, 89, 90, 91, 92, 93]. The differences mainly locate at three aspects. First, the RPMD method chooses the kinetic mass M_i^j in Eq. 7.26 as $M_i^j = m^j/P$, where m^j is the mass of the j^{th} nucleus, if the dynamics is done at real temperature T. Such a setting ensures that the mass of each beads associated with its potential

$V(\mathbf{x}_i^1, \cdots, \mathbf{x}_i^N)/P$ in the case of Eq. 7.26 gives the physical inter-atomic vibration frequency when inter-bead interactions are neglected. If the dynamics is performed at PT, then the potential part in Eq. 7.26 will be

$$\sum_{j=1}^{N}\sum_{i=1}^{P}\left[\frac{1}{2}Pm_j\omega_P^2(\mathbf{x}_i^j - \mathbf{x}_{i-1}^j)^2 + V(\mathbf{x}_i^1, \cdots, \mathbf{x}_i^N)\right] \tag{7.79}$$

and the mass will be chosen as $M_i^j = m^j$.

The second difference between the CMD and the RPMD method is that in CMD the centroid dynamics is used to calculate the time-correlation function. While in the RPMD method, the dynamics in each image is calculated separately and then the time-correlation function for the whole system is an average over all images. Because of this difference, in the RPMD method, the inter-bead vibrations are also accounted for when the vibrational spectrum of the quantum system is calculated. And these artificial vibrational frequencies are evenly distributed on the frequency axis, which often pollute the real physical vibrational frequencies associated with the inter-atomic motion. In the CMD method, on the other hand, the time-correlation function is calculated from the propagation of the centroid. In so doing, the vibration of the centroid won't be polluted by the inter-bread vibrations. However, at low temperatures, taking the OH stretching mode as an example, the centroid of the H atom often falls much closer to the oxygen atom compared with its physical value within each image. This induces the so-called "curvature problem" in CMD simulations, which artificially softens the covalent bond stretching frequencies [399].

The third difference between the CMD and RPMD method is that the RPMD method needs to be carried out in a Hamiltonian manner when the time-correlation function is calculated. In other words, no thermostat should be added when the trajectory under construction will be used in the calculation of the time-correlation function. The temperature effect should be included during the thermal equilibrium process when the canonical distribution of the snapshots starting from which the micro-canonical simulations are carried out is generated. In the CMD method, on the other hand, the canonical ensemble is used for the single trajectory to be generated. Because of this difference, although RPMD doesn't need a very small time step, many trajectories are needed in order for the thermal averaging on the time-correlation function to be sufficiently sampled.

In recent years, there are several studies aiming at comparing the performance of CMD and RPMD in some model and real poly-atomic systems [91, 397, 398]. In Ref. [91], Braams and Manolopoulos showed that the Kubo-transformed autocorrelation functions obtained from the RPMD simulations are accurate on the time scale up to the sixth order for the position and the forth for the velocity. While that of the CMD method leads to an accuracy of the forth order and second order for these two quantities respectively. Hone, Rossky, and Voth, on the other hand,

showed results clearly in favor of CMD [397], where simulations on *para*-hydrogen demonstrates that CMD method gives better agreement with experiments. Later, Perez, Tuckerman, and Müser pointed out that when such a comparison is made, the differences in the setting of the simulations as mentioned above must be kept in mind [398]. Furthermore, in complex systems when the accuracy of the inter-atomic potential is unclear, comparison with experimental results can't be used to judge which one is more accurate, since it is impossible to discern how much of the discrepancy with experiment is due to the accurate of quantum dynamics and how much is due to the inter-atomic potential. Rather, alternative method for such a comparison should be used. In this paper, it is suggested that one uses the same numerical treatment to infer the time-correlation function from the real time axis as obtained from the CMD and RPMD method to the imaginary time axis. Then, these results can be compared with the numerically exact results from imaginary time PIMD or PIMC simulations. In so doing, the performance of these two methods on quantum dynamics is compared solely. We highly recommend such a choice of criterion for future studies in this direction.

7.3 Free-Energy with Anharmonic QNEs

In the previous chapter, we have introduced the thermodynamic integration method. Using this method, the anharmonic contribution from the nuclear thermal fluctuations to the free-energy can be calculated in real poly-atomic systems, as long as a well-defined reference state exists. The QNEs, however, stay on the level of the harmonic approximation. In reality, we know that these QNEs also have anharmonic contributions to their vibrations/rotations and consequently the free-energy. To include such effects, one needs to extend the thermodynamic integration method as introduced in Chapter 6 so that the QNEs on the free-energy beyond the harmonic approximation are also accounted for. In practice, this can be done through an extension of the thermodynamic integration method in the framework of PIMD/PIMC, as will be introduced below.

The starting point for this discussion is the quantum partition function for the real poly-atomic system, defined as:

$$Z^{\mathrm{Q}} = \lim_{P\to\infty} Z_P = \lim_{P\to\infty} \left[\prod_{j=1}^{N} \left(\frac{m_j P}{2\beta\pi\hbar^2}\right)^{\frac{P}{2}}\right] \int_V \int_V \cdots \int_V e^{-\beta V^{\mathrm{eff}}(\mathbf{x}_1,\mathbf{x}_2,\cdots,\mathbf{x}_P)} d\mathbf{x}_1 d\mathbf{x}_2 \cdots d\mathbf{x}_P, \tag{7.80}$$

where

$$V^{\text{eff}}(\mathbf{x}_1, \mathbf{x}_2, \cdots, \mathbf{x}_P) = \sum_{i=1}^{P}\sum_{j=1}^{N}\left[\frac{1}{2}m_j\omega_P^2\left(\mathbf{x}_i^j - \mathbf{x}_{i-1}^j\right)^2\right] + \sum_{i=1}^{P}\frac{1}{P}V(\mathbf{x}_i^1, \cdots, \mathbf{x}_i^N). \tag{7.81}$$

It is clear from our earlier discussion that the free-energy associated with this partition function is the free-energy of the quantum polyatomic system, given by:

$$F^{\text{Q}} = -\frac{1}{\beta}\ln Z^{\text{Q}}. \tag{7.82}$$

Now we look at the effective potential in Eq. 7.82, we notice that we can replace the second term in it by the effective potential on the centroid, as:

$$V^{\text{eff}}(\mathbf{x}_1, \mathbf{x}_2, \cdots, \mathbf{x}_P) = \sum_{i=1}^{P}\sum_{j=1}^{N}\left[\frac{1}{2}m_j\omega_P^2\left(\mathbf{x}_i^j - \mathbf{x}_{i-1}^j\right)^2\right] + \sum_{i=1}^{P}\frac{1}{P}V(\mathbf{x}_{\text{c}}^1, \cdots, \mathbf{x}_{\text{c}}^N). \tag{7.83}$$

Here $\mathbf{x}_{\text{c}}^j$ means the centroid position of the j^{th} nucleus, which doesn't depend on the bead index i. By inputting this equation into Eq. 7.80, we can see that the partition function Z becomes:

$$Z^{\text{C}} = \lim_{P\to\infty}\left[\prod_{j=1}^{N}\left(\frac{m_jP}{2\beta\pi\hbar^2}\right)^{\frac{P}{2}}\right]\int_V\cdots\int_V e^{-\beta\sum_{j=1}^{N}V(\mathbf{x}_{\text{c}}^1,\cdots,\mathbf{x}_{\text{c}}^N)}e^{-\beta\sum_{j=1}^{N}\sum_{i=1}^{P}\frac{1}{2}m_j\omega_P^2\left(\mathbf{x}_i^j-\mathbf{x}_{i-1}^j\right)^2}d\mathbf{x}_1\cdots d\mathbf{x}_P. \tag{7.84}$$

At this time, if we resort to the normal mode coordinate as defined in Eqs. 7.47 and 7.48, Eq. 7.84 can be rewritten as:

$$\begin{aligned} Z^{\text{C}} &= \lim_{P\to\infty}\left[\prod_{j=1}^{N}\left(\frac{m_jP}{2\beta\pi\hbar^2}\right)^{\frac{P}{2}}\right]\int_V d\mathbf{u}_0 e^{-\beta V(\mathbf{u}_0^1,\cdots,\mathbf{u}_0^N)}\prod_{i=-n}^{-1}\prod_{i=1}^{n+1}\int_V e^{-\beta\sum_{j=1}^{N}\frac{1}{2}m_j\lambda_i\omega_P^2(\mathbf{u}_i^j)^2}d\mathbf{u}_i \\ &= \lim_{P\to\infty}\left[\prod_{j=1}^{N}\left(\frac{m_jP}{2\beta\pi\hbar^2}\right)^{\frac{P}{2}}\right]\int_V d\mathbf{u}_0 e^{-\beta V(\mathbf{u}_0^1,\cdots,\mathbf{u}_0^N)}\prod_{i=-n}^{-1}\prod_{i=1}^{n+1}\int_V e^{-\frac{1}{2}\sum_{j=1}^{N}\frac{m_jP}{\beta\hbar^2}(2\sin\frac{i\pi}{P})^2(\mathbf{u}_i^j)^2}d\mathbf{u}_i. \end{aligned} \tag{7.85}$$

Here the n is related to P by $P = 2n + 2$ and the normal modes are aligned as $\mathbf{u}_{-n}^j, \cdots, \mathbf{u}_{-1}^j, \mathbf{u}_0^j, \mathbf{u}_1^j, \cdots, \mathbf{u}_{n+1}^j$, as introduced in Sec. 7.1.4. Making use of the property that $\prod_{i=-n}^{-1}\prod_{i=1}^{n+1}2\sin\frac{i\pi}{P} = P$, the Z^{C} in Eq. 7.85 can be further rewritten

into:

$$
\begin{aligned}
Z^{\mathrm{C}} &= \lim_{P\to\infty}\left[\prod_{j=1}^{N}\left(\frac{m_j P}{2\beta\pi\hbar^2}\right)^{\frac{P}{2}}\right]\left\{\prod_{j=1}^{N}\left[\prod_{i=-n}^{-1}\prod_{i=1}^{n+1}\left(\frac{2\pi\beta\hbar^2}{m_j P}\right)^{-\frac{1}{2}}\left(2\sin\frac{i\pi}{P}\right)^{-1}\right]\right\}\int_V d\mathbf{u}_0 e^{-\beta V(\mathbf{u}_0^1,\cdots,\mathbf{u}_0^N)} \\
&= \lim_{P\to\infty}\left[\prod_{j=1}^{N}\left(\frac{m_j P}{2\beta\pi\hbar^2}\right)^{\frac{P}{2}}\right]\left\{\prod_{j=1}^{N}\left[\left(\frac{2\pi\beta\hbar^2}{m_j P}\right)^{-\frac{P-1}{2}}\frac{1}{P}\right]\right\}\int_V d\mathbf{u}_0 e^{-\beta V(\mathbf{u}_0^1,\cdots,\mathbf{u}_0^N)} \\
&= \left[\prod_{j=1}^{N}\left(\frac{m_j}{2\beta\pi\hbar^2}\right)^{\frac{1}{2}}\right]\int_V d\mathbf{x}_{\mathrm{c}} e^{-\beta V(\mathbf{x}_{\mathrm{c}}^1,\cdots,\mathbf{x}_{\mathrm{c}}^N)},
\end{aligned}
\tag{7.86}
$$

which is simply the classical partition function. In other words, the partition function defined by Eq. 7.80 evolves into a classical partition function if one sets the effective potential $V^{\mathrm{eff}}(\mathbf{x}_1, \mathbf{x}_2, \cdots, \mathbf{x}_P)$ as:

$$
\sum_{i=1}^{P}\sum_{j=1}^{N}\left[\frac{1}{2}m_j\omega_P^2\left(\mathbf{x}_i^j - \mathbf{x}_{i-1}^j\right)^2\right] + \sum_{i=1}^{P}\frac{1}{P}V(\mathbf{x}_{\mathrm{c}}^1,\cdots,\mathbf{x}_{\mathrm{c}}^N). \tag{7.87}
$$

From Sec. 6.4, we know that the free energies of two systems (F_1 and F_0) with potentials (U_1 and U_0) can be linked by a thermodynamic integral. In the above introductions, we also understand that the free-energies of the "artificial" polymer corresponds to the free-energies of the quantum and classical systems respectively, if one takes the effective potential as Eq. 7.81 and Eq. 7.83. Based on this analysis, one can easily introduce an artificial effective potential between the classical and quantum systems, as:

$$
\begin{aligned}
&V^{\mathrm{eff}}(\mathbf{x}_1, \mathbf{x}_2, \cdots, \mathbf{x}_P; \lambda) = \\
&\quad\sum_{i=1}^{P}\sum_{j=1}^{N}\frac{1}{2}m_j\omega_P^2\left(\mathbf{x}_i^j - \mathbf{x}_{i-1}^j\right)^2 + \sum_{i=1}^{P}\frac{1}{P}\left[\lambda V(\mathbf{x}_i^1,\cdots,\mathbf{x}_i^N) + (1-\lambda)V(\mathbf{x}_{\mathrm{c}}^1,\cdots,\mathbf{x}_{\mathrm{c}}^N)\right].
\end{aligned}
\tag{7.88}
$$

Using this effective potential, one can calculate the free-energy of the "artificial system" in between the classical and the quantum one, through:

$$
F(\lambda) = -\frac{1}{\beta}\ln\left[Z(\lambda)\right], \tag{7.89}
$$

with $F(1)$ giving the quantum free-energy and $F(0)$ giving the classical one. The difference between them, in terms of thermodynamic integration, can be calculated using:

$$
\Delta F = F(1) - F(0) = \int_0^1 d\lambda F'(\lambda), \tag{7.90}
$$

where

$$F^{'}(\lambda) = \langle \frac{1}{P} \sum_{i=1}^{P} \left[V(\mathbf{x}_i^1, \cdots, \mathbf{x}_i^N) - V(\mathbf{x}_{\mathrm{c}}^1, \cdots, \mathbf{x}_{\mathrm{c}}^N) \right] \rangle_{V^{\mathrm{eff}}(\lambda)}. \tag{7.91}$$

Similar to Sec. 6.4, the symbol $\langle \cdots \rangle_{V^{\mathrm{eff}}(\lambda)}$ means that ensemble is generated using the effective potential in Eq. 7.88. From Eqs. 7.90 and 7.91, the free-energy difference between the classical and the quantum system can be rigorously evaluated. If the free-energy of the classical system is known, the free-energy of the quantum system will be obtainable. We note that this introduction follows the algorithm by Morales and Singer in Ref. [400]. The only thing one needs to take care is the numerical stability, especially in the strong quantum case when $V(\mathbf{x}_i^1, \cdots, \mathbf{x}_i^N)$ and $V(\mathbf{x}_{\mathrm{c}}^1, \cdots, \mathbf{x}_{\mathrm{c}}^N)$ differ significantly, as pointed out in Ref. [333]. In such cases, non-linear interpolation of the effective potential can be used. For details of this extension, please refer to Ref. [333].

7.4 Examples

For a better understanding of the principles underlying the path-integral molecular simulations, similar to Chapter 5, we also use some examples to show how they work in practice.

7.4.1 Impact of QNEs on Structures of the Water-Hydroxyl Overlayers on Transition Metal Surfaces

The first example concerns the problem on how the impact of the QNEs is like on the structure of the water-metal interface. This problem was investigated by Li, Probert, Alavi, and Michaelides in Ref. [286]. Here, we use some of their results to show how the results of PIMD simulations are analyzed. The system chosen is composed by a transition metal substrate and a hexagonal water-hydroxyl overlayer.

Concerning the importance of such interfaces, it was already well-known in study of surface physics/chemistry that under ambient conditions, most surfaces are covered in a film of water [401]. These wet surfaces are of pervasive and fundamental importance in processes like corrosion, friction, and ice nucleation. On many such surfaces, it was also well-known that the first contact layer of water was not comprised of pure water but instead of a mixture of water and hydroxyl molecules [401, 402, 403, 404, 405, 406, 407, 408, 409, 410, 411]. Physically, these overlayers form because they provide the optimal balance of the hydrogen bonding within the overlayer and the bonding of these overlayers to the surface, and now they have been observed on several oxide, semiconductor, and metal surfaces.

For the characterization of such overlayer structures, from the experimental perspective, it is fair to say that these water-hydroxyl wetting layers are now most well-characterized on close-packed metal surfaces under ultrahigh vacuum (UHV) conditions [401]. In these experiments, it is widely accepted that the molecules in the overlayer are "pinned" in registry with the substrate, with the oxygen atoms sitting right above individual metal atoms in the hydrogen bonded network (see Fig. 7.5). Because of this feature, we can say that the distances between the adjacent molecules are determined mainly by the substrate, being relatively large on a metal with a large lattice constant (e.g. ∼2.83 Å on average on Pt(111)) and small on a metal with a relatively small lattice constant (e.g. ∼2.50 Å on average on Ni(111)). From earlier studies of water in other environments, e.g. certain phases of bulk ice, it was known that the behavior of the shared proton in intermolecular hydrogen bonds varies dramatically over such a large range of O-O distances. For example, under ambient pressures bulk ice is a conventional molecular crystal, with O-O separations of ∼2.8 Å. At very high pressures (≥ 70 GPa), however, the O-O separations can decrease to ∼2.3 Å. In the meantime, ice loses its integrity as a molecular crystal and the protons become delocalized between the O nuclei (see, e.g. Refs. [339, 412, 413]). Now, if we make a direct comparison between the behavior of proton in ice under pressure with that of the water-hydroxyl overlay on metal surfaces, it is reasonable to expect that in the latter system pronounce substrate dependence of QNEs might exist.

To describe the influence of the QNEs on the structure of such overlayers as well as its substrate dependence, as mentioned, one can take a series of systems and perform both *ab initio* MD and PIMD simulations. A comparison between the MD and PIMD results illustrates in a clean manner how such an influence of the QNEs will be. And analysis on the differences between the impact of QNEs on difference substrates tells us the substrate dependence. Based on this consideration, we choose three substrates, *i.e.* Pt(111), Ru(0001), and Ni(111), and performed *ab initio* MD and PIMD simulations at 160 K. These three substrates, in descending order of magnitude of the lattice constant, give a average O-O distance of ∼2.8, ∼2.7, and ∼2.5 Å. Ni was chosen here because of its relatively small lattice constant, although we acknowledge that water-hydroxyl films have not yet been characterized on it [401]. The simulation package chosen is the famous Cambridge Sequential Total Energy Package (CASTEP) [414]. The Perdew-Burke-Ernzerhof (PBE) exchange-correlation functional is used for the descriptions of the electronic interactions within the density-functional theory [129], together with a $\sqrt{3} \times \sqrt{3}$-$R30^\circ$ water-hydroxyl overlayer (see, e.g. Refs. [401, 402, 403, 404, 405, 406, 407, 415, 416]).

Our discussions start from the properties of these overlayers at the classical level. These overlayers are composed by hexagonal hydrogen bonded networks of water and hydroxyl bonded above metal atoms of the substrate in a $\sqrt{3} \times \sqrt{3}$-$R30^\circ$ periodicity. Both types of the molecules lie almost parallel to the surface, forming a perfect

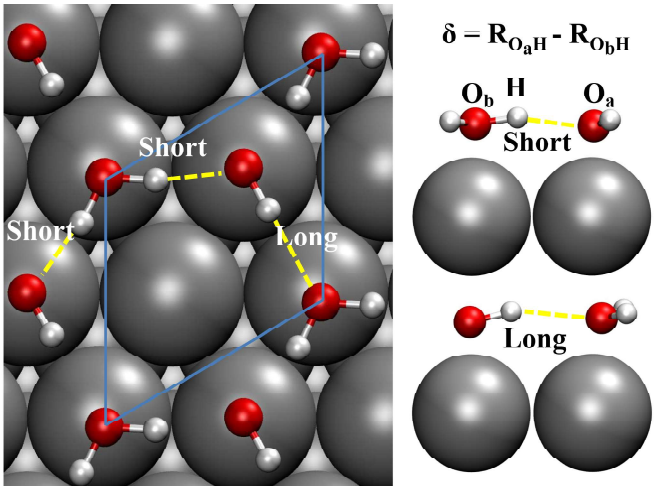

Figure 7.5: Static geometry optimized structure of the $\sqrt{3} \times \sqrt{3}$-$R30°$ overlayer (with classical nuclei) that forms on the transition metal surfaces. Side views on right show the cases when the proton is donated from water to hydroxyl (upper, labeled "short") and from hydroxyl to water (lower, labeled "long"). The short and long hydrogen bond lengths are ∼1.7 and ∼2.1 Å on Pt, ∼1.6 and ∼1.9 Å on Ru, and ∼1.4 and ∼1.6Å on Ni, respectively. The coordinate for proton transfer δ is defined as $R_{\mathrm{O_aH}} - R_{\mathrm{O_bH}}$, where $R_{\mathrm{O_aH}}$ and $R_{\mathrm{O_bH}}$ are the instantaneous O-H distances between $\mathrm{O_a}$ and H and $\mathrm{O_b}$ and H, respectively. For a proton equidistant from its two neighbors, $\delta = 0$ and upon transfer from one O to another δ changes its sign.

extended 2D network. Because OH is a better acceptor of hydrogen bonds than it is a donor, there is an asymmetry in the overlayer with each molecule involved in two short and one long hydrogen bond at the classical static ground state (Fig. 7.5). At finite temperature, *ab initio* MD simulations with classical nuclei show that this asymmetry is still kept, although thermal fluctuations cause the peaks associated with the long and short hydrogen bonds to overlap, particularly on Ni (which has the smallest lattice constant). This asymmetry is illustrated in Fig. 7.6 where we show the probability distributions of O-H and O-O distances on Pt, Ru, and Ni. In addition to this asymmetric feature, the probability distribution of O-H distances also shows that the overlayer is comprised of individual H_2O and OH molecules hydrogen bonded to each other. This is reflected by the sharp peak at ∼1.0 Å, characteristic of the covalent bonds of water and hydroxyl, and broader peaks at ∼1.7-2.1 Å, ∼1.6-1.9 Å, and ∼1.5 Å, characteristic of the hydrogen bonds on Pt, Ru, and Ni, respectively. The probability distributions of the O-H bond length in between these peaks characteristic of the covalent and hydrogen bonds are negligible.

Then we turn on the QNEs and see what happens in the PIMD simulations. A key result is that there is no longer a clear division between short covalent and

longer hydrogen bonds. This is explicitly shown in Fig. 7.6. On Pt, the population of covalent O-H bonds is reduced by one third and replaced with a clearly nonzero probability distribution over the entire range of 1-1.5 Å (Fig. 7.6 (a)). Likewise, the proportion of the short O-O distances is reduced from two thirds to one third, and the center of the peak associated with the short O-O distances moves from ∼2.7 Å to ∼2.5 Å (Fig. 7.6 (b)). These changes are associated with one third of the shared protons being delocalized between the two oxygen atom to which they are bonded. In turn, this delocalization proton further "drags" the oxygen atoms sharing it closer and in so doing creates an "H_3O_2" complex. We note that in this complex, the shared proton belongs to neither of the two oxygen atoms. A typical snapshot from the *ab initio* PIMD simulation is shown in Fig. 7.6 (g) with the H_3O_2 complex located along one particular O-O axis. This snapshot also shows that how when the two oxygen atoms on either side of the shared proton are drawn close, the distances to their other oxygen neighbors increase. It is this effect that leads to a larger proportion of the long O-O distances than that was observed in the classical simulation (Fig. 7.6 (b)).

On Ru, similarly, delocalization of the proton was observed and again the structure contained H_3O_2 complexes (Fig. 7.6 (h)). The smaller lattice constant of Ru also means that only a small variation in the proportion of the short O-O separation (∼2.5 Å) is required to enable proton delocalization (Fig. 7.6 (d)). Upon moving to Ni, the influence of the QNEs on these structural properties becomes even larger. This is shown by the larger magnitude for the distribution of the O-H distances in between the peaks characterizing the covalent and hydrogen bonds (Fig. 7.6 (e)). Because of Ni's smaller lattice constant, the quantum delocalization of the proton within the overlayer becomes possible without any major rearrangement of the oxygen nuclear "skeleton". A snapshot from the PIMD simulation on Ni, in which several protons are delocalized simultaneously and the distinction between covalent and hydrogen bonds is completely lost, is shown in Fig. 7.6 (i).

The obviously different probability distributions observed in the MD and PIMD simulations means that the QNEs significantly changes the structures of the water-hydroxyl overlayer on the transition metal surfaces studied. For a more rigorous characterization of difference from a statistical perspective, we further calculated the free-energy profiles for the protons along the intermolecular axes. This free-energy profile is calculated using $\Delta F(\delta) = -k_{\mathrm{B}}T \ln P(\delta)$, where $P(\delta)$ is the probability distribution of δ and δ is the proton transfer reaction coordinate as defined in Fig. 7.5. k_{B} is the Boltzmann constant. For an unbiased analysis, we take all inequivalent hydrogen bonds in the system into account. In other words, the free-energy profile calculated here is an average over all hydrogen bonds in the overlayer. The results are shown in Fig. 7.7. In the MD simulations with classical nuclei, the free-energy profiles are characterized by two partially overlapping valleys. On Pt (Ru), they locate at $\delta \sim 0.7$ (0.6) and $\delta \sim 1.1$ (0.9) Å. On Ni, these two valleys

almost completely overlap at $\sim$ 0.5 Å, since, as we have said, thermal broadening obscures the distinction between short and long hydrogen bonds on this surface. Concerning proton transfer, it is a rare event, as reflected by the presence of large classical free-energy barriers on all substrates, at $\delta = 0$.

Then we move to the free-energy profiles obtained from the PIMD simulation, in which the QNEs are included in the theoretical descriptions. It is clear in Fig. 7.7 that they differ significantly from the MD ones. On the Pt and Ru substrates, the minima for the long hydrogen bond remain. But we note that those associated with the short hydrogen bonds completely disappear due to the formation of the intermediate H_3O_2 complexes as mentioned before. On Ni, the single valley feature was kept. However, it was softened and its position shifted from $\delta \sim 0.5$ Å to $\delta \sim 0.4$ Å. We note that the key difference between the quantum and classical free-energy profiles is that in the quantum simulations the proton transfer energy barriers are significantly smaller than the classical ones. Upon going from Pt through Ru to Ni, the height of the barrier and the area beneath it decreases, indicating that proton transfer probability increases as the lattice constant is reduced. And a plateau appears on all there quantum free-energy profiles.

To understand how this plateau appears, we correlate the location of the proton along the intermolecular axes (δ) with the corresponding O-O distances ($R_{\mathrm{O-O}}$) and plotted the probability distribution as a function of these two variables in Fig. 7.8. In the MD simulations (Fig. 7.8 (a), (d), and (g)), these functions are characterized by negligible distributions at $\delta = 0$, consistent with the fact that the proton transfer is a rare event and the protons hop from one side of the hydrogen bond to the other. The O-O distribution has two peaks for the short and long hydrogen bonds respectively on Pt and Ru, but they merge on Ni. When the QNEs are taken into account, finite distributions at $\delta = 0$ appear on all three substrates. These distributions correspond to the delocalized protons, as shown by the snapshots in Fig. 7.6. To understand the behavior of this "delocalized" proton from a more rigorously perspective, one focus on the most active proton, *i.e.* the proton which at any given snapshot in the PIMD simulations has the smallest magnitude of δ. On Pt and Ru, this is the proton located along the hydrogen bond with smallest O-O distance. On Ni, due to the fact that the average O-O distance is only $\sim$2.5 Å, the most active proton needs not necessarily be the one with the shortest O-O distance. The results are shown in Fig. 7.6 (c), (f), and (i). The key feature is that different from the panels on the left and middle columns in Fig. 7.6, where the mean peak locates at δ with large magnitude of the absolute value, the distribution peaks on the right column clearly locates around $\delta = 0$. Therefore, the corresponding free-energy barrier for the transfer of the most active proton is zero and the classical proton transfer energy barrier is wiped out by the QNEs.

Another mean feature of the distribution functions in Fig. 7.8 is that a "horse-shoe" shape exists. On Pt and Ru, this indicates that the covalently bonded proton

requires the oxygen atoms to move close first. When this O-O distance is smaller than a certain value, the classical proton transfer energy barrier for the most active proton will become so small that it can be easily wiped out by its zero-point energy. In this case, the quantum nature of the proton results in an "adiabatic" response to the movement of the oxygen atoms and the proton quickly becomes delocalized along this short hydrogen bond. In this case, the H_3O_2 complex as shown in the earlier discussions appears and it persists till the thermal fluctuations of the oxygen cause they to move apart. When this O-O distance is larger than a certain value, the quantum zero-point energy fails to wipe out the classical proton transfer energy barrier and consequently it falls to either side and becomes covalently bonded to one of the oxygen atoms. Therefore, the mechanism for proton transfer on Pt and Ru is the so-called "adiabatic proton transfer" [417], as predicted for the diffusion of the excess proton in water and ice at certain pressures [321, 412].

For more details of these simulations, please refer to Li, Probert, Alavi, and Michaelides' work in Ref. [286].

7.4.2 Impact of Quantum Nuclear Effects on the Strength of Hydrogen Bonds

The second example we want to show here, in which the quantum nature of the nuclei is explicitly addressed, concerns a fundamental problem in physics and chemistry, *i.e.* what will the impact of QNEs be on the strength of hydrogen bonds.

We all know that hydrogen bonds are weak intermolecular interactions which hold much of soft matters together as well as the condensed phases of water, network liquids, and many ferroelectric crystals. The small mass of hydrogen, as shown already in the above example, means that they are inherently quantum mechanical in nature, and effects such as zero-point motion and tunneling must be taken into account in descriptions of the properties related to it. As a prominent example, from the statistical point of view, it is well-known that by replacing H by D the hydrogen bond strength changes. However, as direct as it looks, a simple picture in which the impact of QNEs on the strength of hydrogen bonds and consequently the structure of the hydrogen bonded systems can be rationalized has been absent for a long time.

As a matter of fact, this problem concerning the influence of QNEs on the strength of hydrogen bonds is a fundamental problem in physics and chemistry. Already in the 1950s, it was observed experimentally that in some hydrogen bonded molecular crystals, by replacing the hydrogen with deuterium, the heavy atom (e.g. O-O) distances change [418, 419]. This phenomenon is known as the Ubbelohde effect. The conventional Ubbelohde effect causes an elongation of the O-O distance upon replacing H with D, indicating that the QNEs strengthen the hydro-

gen bond, although a negative Ubbelohde effect has also been observed in several systems [418, 419]. From the molecular simulation's perspective, starting from the beginning of the 1980s, when PIMD and PIMC simulations become a conventional routine to investigate the influence of QNEs in real poly-atomic systems, computer simulations on this issue had been carried out in a wide range of sample systems. A general conclusion is that the result is strongly system-dependent. In liquid hydrogen fluoride (HF), for example, *ab initio* MD and PIMD simulations using density-functional theory for the description of the electronic structures have shown that when the QNEs are accounted for the first peak in the F-F radial distribution function (RDF) sharpens and shifts to a shorter F-F distance [420]. The implication of this increase in the structuring of the RDF in the liquid is that the hydrogen bond is strengthened upon including the QNEs. In contrast, similar simulations for liquid water show that the O-O radial distribution function is less peaked when simulations with quantum nuclei are compared with those with classical nuclei [338], suggesting a decrease of the overall hydrogen bond strength. We note, however, that although this conclusion is probably correct, it is the opposite of what was observed in an earlier *ab initio* study [345].

Besides these discussions concerning hydrogen bonded crystals and liquids, the influence of the QNEs on the hydrogen bonds has also been widely discussed in studies of gas-phase clusters [349, 421, 422]. Specifically, in water clusters up to hexamer, it is predicted that the QNEs weaken the hydrogen bonds, whereas in simulations of the HF clusters both strengthening and weakening is predicted depending on the size of the cluster [349, 421, 423]. For clusters smaller than tetramer, a weakening of intermolecular hydrogen bond is predicted upon including the QNEs. For clusters larger than it, a strengthening of the hydrogen bond is expected. In tetramer, the influence is negligible. We note that these conclusions on the influence of the QNEs on the strength of hydrogen bond differ in different systems. Clearly, it would be very useful to rationalize these various results within a single conceptual framework and identify the underlying factors that dictate the influence of the QNEs on hydrogen bond strength for a broad class of materials. In a recent study (Ref. [322]), Li, Walker, and Michaelides gave a simple picture to rationalize these different results using analysis based on *ab initio* MD and PIMD simulations. Here, we use some of their key results to show how it is done in practice.

First of all, a broad range of hydrogen bonded systems are chosen, including HF clusters (dimer to hexamer), H_2O clusters (dimer, pentamer, and octamer); charged, protonated, and hdyroxylated water and ammonia clusters ($H_9O_5^-$, $H_9O_4^+$, $H_7O_4^-$, and $N_2H_5^-$); organic dimers (formic acid and formamide); and solids (HF, HCl, and squaric acid $C_4H_2O_4$). For each system both conventional *ab initio* MD simualtions, in which the nuclei are treated as classical point-like particles, and more state-of-the-art *ab initio* PIMD simulations, in which the QNEs are accounted for, were performed. With these two complementary sets of simulations, one can identify in

a very clean manner the precise influence of the QNEs on the statistical properties we are interested in at finite temperatures.

Before we start, let us first make the following points clear. First, the quantities we focus on when characterizing H-bonds are: (i) the heavy-atom (X-X, where X is either O, Cl, C, N, or F) distances, which characterize the intermolecular separations; (ii) the H-bond angles (X-H...X), which are associated with H-bond bending (libration) modes; and (iii) the X-H covalent bond lengths, characteristic of the covalent bond stretching in the H-bond donor molecules. In later discussion, it will become clear that these quantities provide an indication of H-bond strength. However, as the main measure of H-bond strength we still use a standard estimate based on the computed red-shift (softening) in the X-H stretching frequency of the H-bond donor molecule. We note that there is no perfect measure for H-bond strength [424], however the redshift of the stretching frequency is a widely used measure [see, e.g. Refs. [425, 426]). This measure is particularly useful here because it allows us to discriminate between different types of H-bond in the same complex and can be used for both neutral and charged systems. In Fig. 7.9 (b), it is shown that this estimator correlates well with the computed binding energy per H-bond in the neutral systems we study. This binding energy is defined as the difference between the total energy of the system and the sum over its unrelaxed components, as in ref. [424]. When the redshift of the stretching frequency (measured as the ratio of the X-H stretching frequency in the H-bonded cluster to that in the free monomer) gets larger, the H-bond comes stronger.

With the definition of the above defined quantities in mind, we first look at the results for the impact of the QNEs on the strength of hydrogen bonds. Upon comparing these results for the various hydrogen bonded systems, an interesting correlation can be established between the H-bond strength and the change in intermolecular separations. This correlation is shown in Fig. 7.9 a) where we see that as the H-bond gets stronger the heavy-atom separations in the PIMD simulations with quantum nuclei go from being longer than those in the MD simulations with classical nuclei (positive Δ(X-X)) to being shorter (negative Δ(X-X)). Thus the QNEs result in longer hydrogen bonds in weak hydrogen bonded systems and shorter hydrogen bonds in relatively strong hydrogen bonded systems. We note that the hydrogen bond strength increases upon going from small to large clusters and from water to HF. The trend reported in Fig. 7.9 is a key finding and in the following we explain why it emerges and discuss the implications it has for H-bonded materials in general.

To understand the reason of this correlation between the impact of the QNEs on the strength of hydrogen bond and the strength of hydrogen bond itself, it is useful to look at the HF clusters. These provide the ideal series because upon increasing the cluster size the hydrogen bond strength increases, and the influence of the QNEs switches from a tendency to lengthen to a tendency to shorten the intermolecular separations (as seen in Ref. [423]). Our analysis is summarized in

Fig. 7.10, where we plot the distance and angle distributions from MD and PIMD simulations for these three HF clusters separately. The left column shows the final results, where one can see that in the dimer the averaged F-F distance is increased by including the QNEs, in the tetramer there is no difference between the averaged quantum and classical F-F distances, while in the pentamer the F-F distance is clearly shortened by including the QNEs. The key to understanding this variation of the heavy-atom distances is in recognizing that there are also related differences between MD and PIMD in the covalent F-H bond lengths (center) and H-bond angles (right). Because of anharmonic quantum fluctuations, these two geometric properties also show systematic changes. First of all, the F-H bonds are longer in the quantum compared to the classical simulations, and this elongation becomes more pronounced as the H-bonds get stronger. Second, the hydrogen bonds are more bent in the quantum than in the classical simulations, and this bending generally becomes less pronounced as the hydrogen bonds get stronger. In order to understand the influence of these variations in structure, analysis of various dimer configurations was performed. This analysis reveals that the covalent bond stretching increases the intermolecular interaction whereas hydrogen bond bending decreases it. Taking the HF dimer as an example, a 0.04 Å increase in the F-H bond length of the donor leads to a 40 meV increase in interaction energy within the dimer, whereas in contrast a 21° reduction in H-bond angle leads to a 16 meV decrease in interaction energy. This analysis provide a qualitative understanding of the trend observed. In short, the F-F distance increases in the dimer as a result of a large decrease in hydrogen bond angle but only a small increase in the covalent F-H bond length. Whilst in the tetramer, the F-H stretching is sufficiently pronounced to compensate for the increase in hydrogen bond bending, leaving the overall F-F distance unchanged and in the pentamer, the F-F distance decreases because the F-H covalent bond stretching dominates over the H-bond bending.

For a rigorous examination of this picture and a quantitative description of this competition for all systems studied, one can further calculate the projection (X-H$^{||}$) of the donor molecules covalent bond along the intermolecular axis (see inset of Fig. 7.11). Since X-H$^{||}$ increases upon intramolecular stretching but decreases upon intermolecular bending, this quantity itself allows the balance between stretching and bending to be evaluated, to a certain extend. The influence of the QNEs is quantified by the ratio of the PIMD and MD projections, *i.e.* $x = (\text{X-H}^{||})^{\text{PIMD}}/(\text{X-H}^{||})^{\text{MD}}$. When this value is clearly greater than one, it indicates that when the QNEs are included, the main influence is on the stretching of the covalent bond. And when this value is clearly smaller than one, it indicates that when the QNEs are included, the main influence is on the bending of the hydrogen bond. When one plots this ratio against the variations in intermolecular separations, $y = \Delta(\text{X-X})$ (which we used to quantify the impact of the QNEs). A striking (almost linear) correlation is observed (Fig. 7.11). For all systems where hydrogen bond bending dominates (x

clearly smaller than 1), the heavy-atom distances are longer in PIMD than in MD ($y > 0$). In cases where covalent bond stretching is dominant (x clearly larger than 1), the heavy-atom distances are shorter in PIMD than in MD ($y < 0$). With the increase of x, quantum fluctuations on the stretching mode become more dominant and the QNEs turn from weakening the hydrogen bonds to strengthening them. Thus the overall influence of the QNEs on the hydrogen bonding interaction quantitatively comes down to this delicate interplay between covalent bond stretching and intermolecular bond bending. One notes that this explanation arrived at here for the general case is consistent with what Manolopoulos and coworkers have elegantly shown for liquid water in Ref. [427].

Given the ubiquity of the hydrogen bonds in the physical, chemical, and biological sciences, there are a number of implications of this finding. Considering that liquid HF is comprised of long polymer chains and rings whereas liquid water is widely considered to be made up of small clusters, these results shed light on why the QNEs strengthen the structure of liquid HF but weaken that of liquid water [338, 420]. More generally, one can use the trend observed in Fig. 7.9 as a simple rule of thumb to estimate the impact of the QNEs on hydrogen bonded systems without performing expensive PIMD simulations. All that is required is an estimate of hydrogen bond strength, which can be obtained from the redshift in the covalent stretching frequency or from other commonly used measures of hydrogen bond strength such as hydrogen bond length. Thus the trend may be particularly useful to biological systems such as α-helixes and β-sheets for which many crystal structures have been determined and where cooperative effects lead to particularly strong H-bonds [428].

In addition to the implications mentioned, this trend also allows one to rationalize the Ubbelohde effect over a broad range of H-bond regimes (Fig. 7.9 c)). Specifically speaking, traditional Ubbelohde ferroelectrics such as potassium dihydrogen phosphate fall in the relatively strong H-bond regime where a positive Ubbelohde effect (*i.e.*, an increase of the X-X distance upon replacing H with D) is observed in experiment and also in recent PIMD studies [419, 429]. And in this context the squaric acid, the solid HF, and the larger HF clusters are expected to exhibit a traditional Ubbelohde effect upon replacing H with D. In contrast, the smaller hydrogen bonded clusters studied here and solid HCl are expected to exhibit a negative Ubbelohde effect (a decrease of the X-X distance upon replacing H with D). Hydrogen bonded materials of intermediate strength such as large water clusters and ice at ambient pressure are predicted to exhibit a negligible Ubbelohde effect because in this regime the QNEs have little influence on the intermolecular separations. Indeed this observation is consistent with experimental and theoretical observations for the ferroelectric hydrogen bonded crystals, ice, and gas-phase dimers [418, 419, 422].

A further prediction stemming from this work is that ice under pressure will exhibit the traditional Ubbelohde effect. However one cautions that at very high

pressure ice possesses such strong hydrogen bonds, with shared symmetric protons [412], that the picture sketched in Fig. 7.11 is not likely to apply. Indeed, this note of caution applies to all ultra-strong hydrogen bonds, where the proton is shared symmetrically by the two heavy atoms already in the classical perspective. In this case, the distinction between a relatively short covalent bond and a relatively long hydrogen bond is lost and bond stretching along the X-X axis does not lead to any strengthening of the intermolecular interactions. The gas-phase Zundel complex, $H_5O_2^+$, is an example of one such ultra-strong hydrogen bond and the calculations in Ref. [322] show an approximately 0.016Å increase in the O-O distance, which is consistent with previous studies [326, 430].

Another class of very strong H-bonded systems are the so-called "low-barrier" H-bonds, e.g., $H_3O_2^-$, $N_2H_7^+$, and $N_2H_5^-$. In these systems there remains a clear distinction between covalent and hydrogen bonds and the picture we have presented still holds. This fact can be seen from our data for $N_2H_5^-$ in Fig. 7.9. We caution, however, that in these very strong H-bonded systems errors associated with the underlying exchange-correlation functional can have a qualitative impact on the results and that the accuracy of the underlying potential energy surface is of critical importance. For example, in $H_3O_2^-$ and $N_2H_7^+$, using the PBE exchange-correlation functional yields a shared symmetric proton already in the classical MD simulations. But earlier studies with the more accurate second-order Møller-Plesset perturbation theory and also the Becke-Lee-Yang-Parr exchange-correlation functional [326, 430, 431], show that protons actually feel a double-well potential and in this case quantum nuclear effects strengthen the hydrogen bond, consistent with the model presented here. In addition to this, since both inter- and intra-molecular vibrations are relevant to the QNEs, this work also highlights the need for flexible anharmonic monomers in force-field simulations of the quantum nuclear effects. Specifically, if this feature is absent, only hydrogen bond bending will be present in the simulation and consequently the inter-molecular interaction will be "artificially" weakened. For more details concerning such discussions and the numerical details of the calculations, please refer to Ref. [322].

7.4.3 Quantum Simulation of the Low-Temperature Metallic Liquid Hydrogen

The third example we show here, in which the *ab initio* PIMD simulation is used to study the fundamental properties of condensed matter, concerns existence of a low-temperature quantum metallic liquid, which exists in high pressure hydrogen.

Concerning the importance for the existence of this low-temperature metallic liquid phase, one can track back to a very famous conjecture about hydrogen under pressure. This conjecture was first proposed by Wigner and Huntington in 1935, it

states that solid molecular hydrogen would dissociate and form an atomic metallic phase at high pressures [432]. Ever since this prediction, the phase diagram of hydrogen has been the focus of intense experimental and theoretical studies in condensed matter and high pressure physics [278, 281, 433, 434, 435, 436].

Due to the advance of many experimental techniques, notably diamond anvil cell approaches, nowadays it is possible to explore hydrogen at pressures up to about 360 GPa [433, 437, 438, 439]. And one notes that new types of diamond anvil cell may be able to access even higher pressures [440]. These experiments, together with numerous theoretical studies, have revealed a remarkably rich and interesting phase diagram comprising regions of stability for a molecular solid, a molecular liquid and an atomic liquid, and within the solid region four distinct phases have been detected [438, 439, 441]. In high-temperature shock-wave experiments, metallic liquid hydrogen has also been observed [442, 443]. It is accepted to be a major component of gas giant planets, such as Jupiter and Saturn [443]. Despite the tremendous and rapid progress, important gaps in our understanding of the phase diagram of high-pressure hydrogen still remain, with arguably the least well-understood issue being the solid to liquid melting transition at very high pressures. Indeed the melting curve is only established experimentally and theoretically up to around 200 GPa [278, 436]. From 65 GPa up to about 200 GPa, the slope of the melting curve is negative (that is, the melting point drops with increasing pressure), which suggests that at yet higher pressures a low temperature liquid state of hydrogen might exist or, as suggested by Ashcroft [444], perhaps even a metallic liquid state at zero K. Further interest in hydrogen at pressures well above 200 GPa stems from other remarkable suggestions, such as superfluidity [435] and superconductivity at room temperature [445, 446], all of which imply that hydrogen at extreme pressures could be one of the most interesting and exotic materials in all of condensed matters.

In Ref. [323], Chen *et al.* used computer simulation techniques to probe the low-temperature phase diagram of hydrogen in the ultra-high 500 to 1,200 GPa regime to try and find this potential low-temperature liquid state of hydrogen. Concerning the proton motion in this condensed phase, *ab initio* PIMD as introduced earlier in this chapter has been used. To compute the melting curve, the solid and liquid phases in coexistence were simulated [278, 447, 448]. This coexistence approach, or otherwise called two-phase simulation method, minimizes hysteresis effects arising from superheating or supercooling during the phase transition. With this combination of approaches they have found a low-temperature metallic atomic liquid phase at pressures of 900 GPa and above, down to the lowest temperature they can simulate reliably of 50 K. The existence of this low-temperature metallic atomic liquid is associated with a negative slope of the melting curve between atomic liquid and solid phases at pressures between 500 and 800 GPa. This low-temperature metallic atomic liquid is strongly quantum in nature, as treating the nuclei as classical par-

ticles using the *ab initio* MD method significantly raises the melting curve of the atomic solid to ∼300K over the whole pressure range. The classical treatment of the nuclei does not reproduce a notable negative slope of the melting curve, and consequently does not predict a low-temperature liquid phase.

For a clear explanation of these results, we go through the details procedures of their study here. One problem which is essential in a theoretical description of the hydrogen phase diagram is that in its solid phase many local minima on the potential energy surface exist. Therefore, in order for the *ab initio* MD and PIMD simulations to make sense, extensive computational searches for low-enthalpy solid structures of hydrogen must be performed. From earlier studies using density function theory methods [15, 449, 450, 451, 452], a metallic phase of $I41/amd$ space group symmetry has been widely reported to be stable from about 500 to 1,200 GPa, when quasi-harmonic proton zero-point motion was included. Accordingly, they have used this phase as the starting point for their finite temperature exploration of the phase diagram and melting curve [323]. With the coexistence method, they have performed a series of two-phase solidCliquid simulations at different temperatures (from 50 to 300 K), which are then used to bracket the melting temperature from above and below. We begin by considering the 500 to 800 GPa pressure regime and show an example of the data they have obtained from the coexistence simulations at 700 GPa in Fig. 7.12. At this pressure one can see that for $T \geq 125$ K, the system transforms into a liquid state, whereas for $T \leq 100$ K, it ends up as solid. To characterize these states, they have used a pair-distribution function and averaged out its angular dependence. The result is a function of interatomic separations, which is denoted by $g(r)$ throughout this section. In a liquid, this is the so-called radial distribution function. As can be seen in Fig. 7.12 d), upon moving from 100 to 125 K the system clearly possesses less structure, indicating that a transition from solid to liquid occurs. These phases were also characterized by the variations in the mean square displacement of the nuclei of the particles over time. As PIMD rigorously provides only thermally averaged information, they have used the partially adiabatic centroid MD (PACMD) approach within the path-integral scheme to obtain real-time quantum dynamical information [397]. Again, as shown in Fig. 7.12 e), the distinction between the solid phase at 100 K and liquid phase at 125 K is clear.

The same coexistence procedure was used to locate the melting point at 500 and 800 GPa, leading to the melting curve shown in Fig. 7.13. The up (down) triangles indicate the highest (lowest) temperatures at which the solid (liquid) phases are stable, bracketing the melting temperatures within a 25 K window. From this we see that the melting temperature is between 150 and 175 K at 500 GPa, and that it drops rapidly with increasing pressure, yielding a melting temperature of only between 75 and 100 K at 800 GPa. Thus, the melting curve has a substantial negative slope ($dP/dT < 0$) in this pressure range. Across this entire pressure range the molten liquid state is atomic, and the solid phase, which grows, is the original

atomic $I41/amd$ phase that was used as the starting structure. Given that molecular phases have been observed at pressures lower than 360 GPa in both experimental and theoretical studies [437, 439], they have suggested that a molecular-to-atomic solid-solid phase transition should occur between 360 GPa and 500 GPa (the lowest pressure they have considered in their simulations of the melting).

The negative slope of the melting curve up to 800 GPa suggests that at even higher pressures a lower-temperature liquid phase might exist. Motivated by this, they also carry out simulations at 900 and 1,200 GPa. However, in this pressure range one needs to consider nuclear exchange effects, which are neglected in the PIMD simulations, but could potentially become significant. Indeed, analysis of their simulations reveals that at these pressures the dispersion of the beads in the path-integral ring polymer becomes comparable to the smallest interatomic separations when the temperature is below $\sim$40 K. This is the so-called quantum degeneracy temperature below which the exchange of nuclei will be important, and consequently simulations with a (standard) PIMD approach are expected to be inaccurate. With this in mind they have performed all simulations in this very high-pressure regime at T$\leq$50 K. Interestingly, they find that at 50 K, at both 900 and 1,200 GPa, the systems are already in the liquid state, revealing that the melting temperature at these pressures is below 50 K. Whether the liquid phase is the 0 K ground state of hydrogen at these pressures is not something one can establish at this stage. However, the large negative slope of the melting curve at lower pressures and the observation of a liquid phase at temperatures as low as 50 K provide strong support for Ashcroft-s low-temperature liquid metallic state of hydrogen [444], and it implies that any room temperature superconductor in this regime would have to be a liquid.

In order to understand the role the QNEs play in inducing the properties discussed, it is instructive to compare the results of the *ab initio* PIMD simulations with those obtained from the *ab initio* MD approach in which the nuclei are approximated by classical point-like particles. To this end, they have performed a second complete set of coexistence simulations with *ab initio* MD across the entire 500 to 1,200 GPa range. The *ab initio* MD melting curve is shown by the red data in the inset of Fig. 7.13, where it can be seen that the melting temperatures obtained from the MD simulations are much higher than those from the fully quantum PIMD simulations. The *ab initio* MD melting temperature is well above 200 K across the pressure range 500-1,200 GPa, and the slope of the melting curve is small. A melting curve with a negative slope was also found above 90 GPa in the *ab initio* MD simulations of hydrogen by Bonev et al. [278] and above 10 GPa in lithium [454]. In Ref. [323], *ab initio* MD simulations with classical nuclei exhibit considerably higher melting temperatures than the *ab initio* PIMD ones at pressures above 500 GPa, which shows that the quantum description of the protons strongly depresses the melting point. The entropy arising from the greater delocalization of the protons in the quantum description has a crucial role in stabilizing the low-temperature liquid.

Before we end our discussion, it is worthwhile to note that serious analysis on the accuracy of the simulations should always be carried out in molecular simulations in general. Taking the low-temperature metallic liquid phase we discussed above as an example, the main conclusion is that the melting line of solid hydrogen has a negative slope and that the quantum fluctuations of the nuclei lead to a low temperature (<50 K) metallic liquid phase at pressures higher than 900 GPa. We use the remaining part of this section to discuss the accuracy of the simulations from which these conclusions are drawn. This analysis includes: i) the accuracy of the electronic structures, and ii) the convergence of the *ab initio* MD and PIMD simulations with respect to the number of beads used in representing the finite-temperature imaginary time path-integral of the nuclei, the simulation cell size and simulation time, as well as the significance of nuclear exchange effects, a factor which is not accounted for in the PIMD method. Besides these, the superconducting properties of the solid atomic phase will also be discussed.

We start with the accuracy of the Brillouin zone integrations and plane-wave basis set cutoff energies used in our MD and PIMD calculations. In the main manuscript of Ref. [323], a Monkhorst-Pack k-point mesh of spacing $2\pi \times 0.05\text{Å}^{-1}$ was used for the Brillouin zone integration and a 500 eV cutoff was used for the expansion of the electronic wave functions. Fig. 7.14 shows the variation of the relative static lattice enthalpies of various relevant structures over the pressure range 500 to 1,200 GPa. These results are in very good agreement with those reported in an even earlier study (Ref. [451]). The molecular $Cmca$ phase is found to be the most stable at 500 GPa, and the phase transition from $Cmca$ to the atomic $I41/amd$ phase occurs at about 500 GPa. The $I41/amd$ phase has the lowest static lattice enthalpy from about 500 GPa to over 1200 GPa.

Then one investigates how well the above k-point mesh spacing and cutoff energy perform when thermal and quantum fluctuations of the nuclei are included in the calculations. For this purpose six snapshots (three from simulations for solids at low temperatures and three from liquid phases) were chosen at random from the PIMD simulations at 700 GPa. The centroid of each atom is used and they have performed single point calculations for the total energy of these structures using a higher energy cut-off (600 eV) and a denser k-point mesh ($8 \times 8 \times 8$, which corresponds to a grid of spacing $2\pi \times 0.025$ Å^{-1} in the Monkhorst-Pack k-point mesh). The differences between the results obtained with these settings and those used in the MD and PIMD simulations (500 eV and a $4 \times 4 \times 4$ k-point mesh) are smaller than 1 meV, see Fig. 7.15 (a). These errors are negligible compared with the several tens of meV energy differences between the internal energy of the liquid and solid phases.

One notes that the PBE exchange-correlation functional was used in MD and PIMD simulations reported. This functional suffers from self-interaction errors which can be significant in systems containing hydrogen. One can investigate the potential role of the self-interaction errors by comparing the total energies obtained

with PBE and PBE0. PBE0 is a hybrid functional containing 25% Hartree-Fock exact exchange [455]. Therefore, the self-interaction error arising from the PBE0 functional is expected to be smaller than that of the PBE functional. In addition to this, comparisons with other functionals such as LDA and optB88-vdW [456, 457] within the van der Waals density functional (vdW-DF) scheme [458, 459] should also give some insights. Based on this consideration, in Fig. 7.15 (b) we compare the relative energies of the six snapshots using LDA, PBE, optB88-vdW and PBE0. LDA and optB88-vdW give very similar results to the PBE ones. PBE0 gives lower total energies for the liquid phase than for the solid, and consequently it favors melting of the solid. It is therefore likely that using a more accurate density functional than PBE would lead to stabilization of the liquid phase at even lower temperatures.

In PIMD simulations, the number of beads used to sample the imaginary time path integral is a very important parameter in the description of the quantum nuclear effects. A series of tests at 700 GPa were therefore performed and the melting temperature was calculated using 1 (MD), 4, 8, 16, 24, 32, 48, and 64 beads to check if the melting temperature converges with respect to the number of beads. The results are shown in Fig. 7.16. We find that 32 beads are required to ensure that the melting temperature is converged within a window of 25 K. In Ref. [323], they have therefore used 32 beads for the main calculations reported in the main manuscript.

The results of the two-phase simulations also depend on the size and shape of the simulation cell. In Fig. 7.17, one checks the dependence of the results on the cell size in the MD simulations. Using a cell containing 200 atoms gives results identical to those from 432 and 576 atoms. In the PIMD simulation reported in Ref. [323], they have also compared results using 200 and 300 atoms, and found that these simulations gave essentially identical results. Therefore, they believe that using a cell containing 200 atoms in the simulations is accurate (at least) for a qualitative description of the phenomena reported.

In the two-phase PIMD simulations, solidification and melting happen on a time scale of 1 ps. To ensure that the systems have equilibrated, Chen *et al.* have run all simulations for 10 ps and calculated the angularly averaged pair-distribution function $g(r)$, as explained above, using different time intervals. They found very good convergence with respect to the simulation time already at 3 ps (Fig. 7.18).

In standard PIMD simulations, the exchange of nuclei is neglected. To estimate if the neglect of nuclear exchange effects has a significant effect on the accuracy of the simulations, Chen *et al.* have also examined the distributions of distances between beads in the same nucleus and between beads in neighboring nuclei. Results at 1,200 GPa (900 GPa) and 50 K are reported in Fig. 7.19, where the distribution of distances between bead 1 and bead $N/2+1$ of the ring polymer in the 32 bead simulation (N=32) was compared with the distribution of H-H distances for the same bead. The distances between bead 1 and bead $N/2+1$ of the ring polymer

give the solid curves and the H-H distances of the same bead give the dashed curves. The absence of any significant overlap between the peaks of these two curves in this highest pressure and lowest temperature simulation suggests that exchange effects are unlikely to be an issue in the simulations reported. As the pressure decreases from 1,200 GPa to 900 GPa, the overlap of the two curves becomes even smaller.

The last property one concerns in the simulations is the superconductivity feature of this hydrogen at this region of the phase diagram. It has been widely reported that metallic hydrogen formed at these pressures could be a high T_c superconductor [445, 446, 460]. Therefore, Chen *et al.* have also calculated T_c for the $I41/amd$ solid phase using the Allen-Dynes equation [461] and the QUANTUM-Espresso code [462]. They found that over the entire pressure range examined (500 to 1,200 GPa) T_c is predicted to be around room temperature or above, which is consistent with previous predictions for $I41/amd$ at these pressures in Ref. [446]. At 500 GPa, for example, the conservative estimate of T_c is 358 K. To understand the physical origin of this high T_c phase we show details of its electronic and vibrational properties at 500 GPa in Fig. 7.20. This reveals a high electronic density of states (DOS) at the Fermi level (Fig. 7.20 (a)), strong electron-phonon coupling (Fig. 7.20 (d)), and consequently a high value of λ (2.15) which leads to a high value of T_c within Bardeen-Cooper-Schrieffer (BCS) theory [463].

These results were obtained using a dense q-point mesh ($8 \times 8 \times 8$). Their convergence with the energy cut-off for the PAW pseudopotential is shown Fig. 7.21. A cut-off energy of 80 Ryd gives good convergence for both T_c and the electron-phonon interaction parameter λ. In Fig. 7.21 (b), we also plot T_c versus μ^* for the LDA and PBE functionals. We found that the LDA and PBE results for T_c are similar, and both of them give T_c values which are much higher than the melting temperature of the solid phase. In Ref. [323], they have used $\mu^* = 0.1$ to obtain the value of $T_c = 358$ K reported. This value of μ^* is close to the value of 0.085 obtained from the Bennemann-Garland formula [464] and larger than the value of 0.089 used in Ref. [446]. From Fig. 7.21 (b), it is clear that T_c decreases with increasing μ^*. Considering the fact that they have chosen a large value of μ^* and that their value of T_c is still much higher than the melting temperature of the solid phase, it is reasonable to suppose that the atomic solid phase under the melting line is superconducting. As the crystal melts well below room temperature their results also rule out a room temperature superconducting phase of solid hydrogen at the pressures considered here and concluded that any room temperature superconductor in this regime would have to be a liquid. For more details concerning this study, please also refer to Ref. [323].

7.5 Summary

In summary, we have discussed some extensions of the molecular simulation methods as introduced in the earlier chapters to descriptions of the QNEs in this chapter. The language we have used is the path-integral representation of the quantum mechanics. Based on this language, the general theory behind the statistical path-integral molecular dynamics and path-integral Monte-Carlo methods was explained, as well as their extensions to the dynamical regime. A combination between the thermodynamic integration and PIMD methods was also presented. And some examples for the practical simulations of these computational methods were shown. These introductions, together with the computational methods for the calculation of the electronic structures and simulations of the molecular dynamics as presented in the earlier chapters, aim to set up a framework of concepts concerning molecular simulations of molecules and condensed matters. We sincerely hope this framework can help those graduate students working on computer simulations of molecules and condensed matters to find the proper recipe to tackle the problems they are interested in.

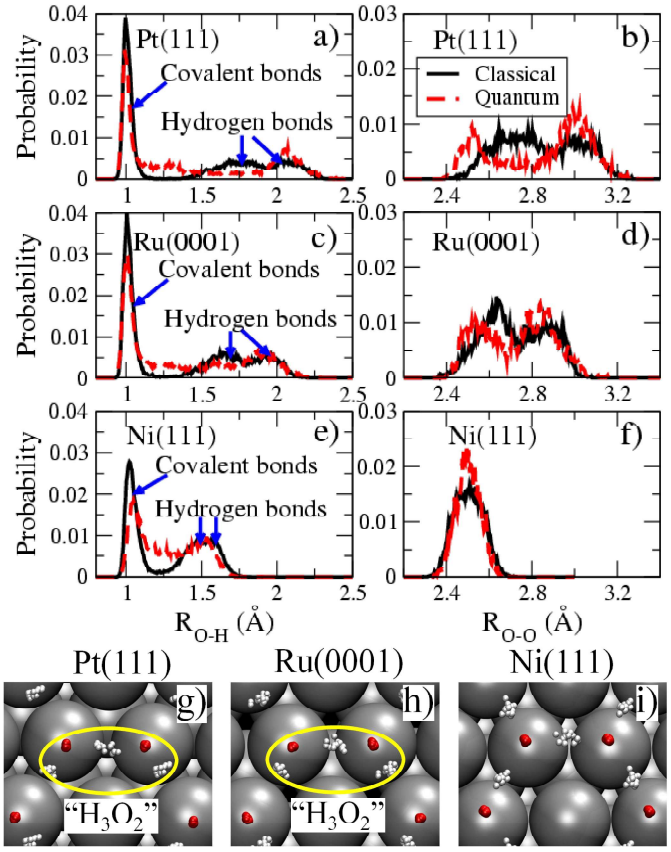

Figure 7.6: Statistical structural information from the *ab initio* MD and PIMD simulations of the water-metal interfaces, using some selected structural properties. More specific, probability distributions of the O-H [(a), (c), (e)] and O-O distances [(b), (d), (f)] on Pt(111), Ru(0001), and Ni(111) are chosen. Results obtained from *ab initio* MD simulations with classical nuclei were labeled "classical" and shown by solid lines in black. Those from the *ab initio* PIMD simulations with quantum nuclei at the statistical level were labeled "quantum" and shown by dashed lines in red. A key difference between the MD and PIMD results is that in the PIMD simulations, a non-negligible distribution of the O-H distance in between the covalent and hydrogen bond peaks was observed. This feature is absent in the MD simulations with classical nuclei and it originates from some spatial configurations of the system during the simulation in which one proton is equally shared by two oxygen atoms. In panels (g) to (i), we show some snapshots for typical spatial configurations of the overlayer on Pt, Ru, and Ni obtained from the PIMD simulations (using 16 beads). On Pt and Ru, at any given snapshot one proton is equally shared by two of the oxygen atoms yielding an intermediate "H_3O_2" complex. On Ni at any given snapshot several protons can simultaneously be shared between the oxygens.

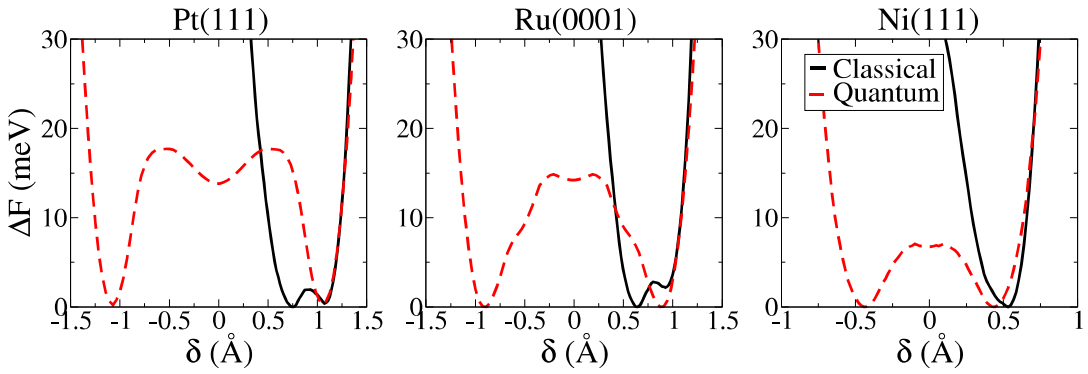

Figure 7.7: Free-energy profile (denoted as ΔF) for the protons along the intermolecular axes within the water-hydroxyl overlayers on Pt (left), Ru (middle), and Ni (right) from the *ab initio* MD and PIMD simulations at 160 K. The MD results were labeled classical and shown by solid lines in black and the PIMD results were labeled quantum and shown by dashed lines in red.

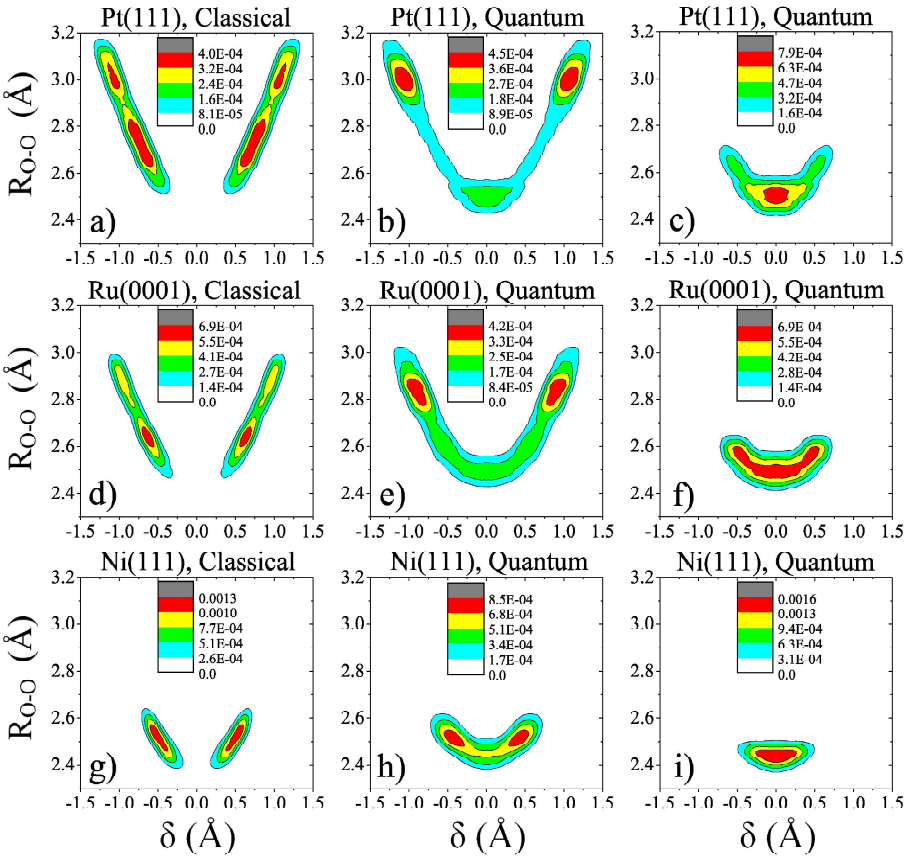

Figure 7.8: Probability distribution in the MD and PIMD simulations as a function of δ and $R_{\mathrm{O-O}}$. Similar to the earlier figures, the MD simulations are labelled as classical and the PIMD simulations are labelled as quantum. The left and middle columns show results obtained from all hydrogen bonds in the overlayer. On the right column, only data from the most active hydrogen bond is chosen in the PIMD simulations. The most active proton is defined as the one with the smallest δ. All MD and PIMD distribution functions have been symmetrized with respect to δ.

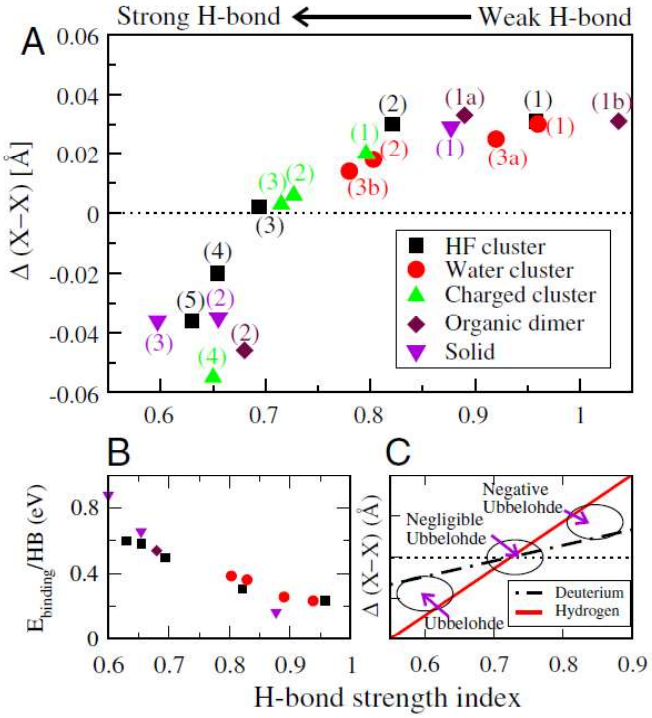

Figure 7.9: Correlation between the impact of the QNEs and the hydrogen bond strength. In panel a), the differences between the shortest heavy-atom distances obtained from the PIMD and MD simulations $(\text{X-X})^{\text{PIMD}}_{\text{average}}$-$(\text{X-X})^{\text{MD}}_{\text{average}}$, denoted by Δ(X-X), is chosen as the y axis. It characterizes the impact of the QNEs on the strength of the hydrogen bonds. This influence is drawn as a function of the hydrogen bond strength. As mentioned in the main manuscript, this hydrogen bond strength is defined as the ratio of the X-H stretching frequency in the hydrogen bonded system to that in the free monomer. In panel b), the correlation between this hydrogen bond strength index and the binding energy per hydrogen bond in the neutral systems is given. In panel c), simplified schematic illustration of the expected isotope (Ubbelohde) effect on the differences in heavy-atom distances. We suggest that three regimes of positive, negligible, and negative Ubbelohde effect depending on the hydrogen bond strength exist. For the HF clusters, labels 1-5 denote the hydrogen bonds in the dimer to the hexamer. For the water clusters, labels 1, 2, 3a, and 3b refer to the hydrogen bonds in the dimer, pentamer, and the long (short) hydrogen bond in the octamer. For the charged clusters, labels 1-4 refer to $H_9O_5^-$, $H_9O_4^+$, $H_7O_4^-$, and $N_2H_5^-$, respectively. For the organic dimers, labels 1a, 1b, and 2 refer to the redshifted and blueshifted hydrogen bond in the formamide and the redshifted hydrogen bond in formic acid. For the solids, labels 1-3 refer to the hydrogen bonds in HCl, HF, and squaric acid. The same labels are applied in Fig. 7.11. For the water cluster in panels b), the octamer is not included since there are two kinds of hydrogen bonds. Results for the trimer and tetramer are added to further test the correlation.

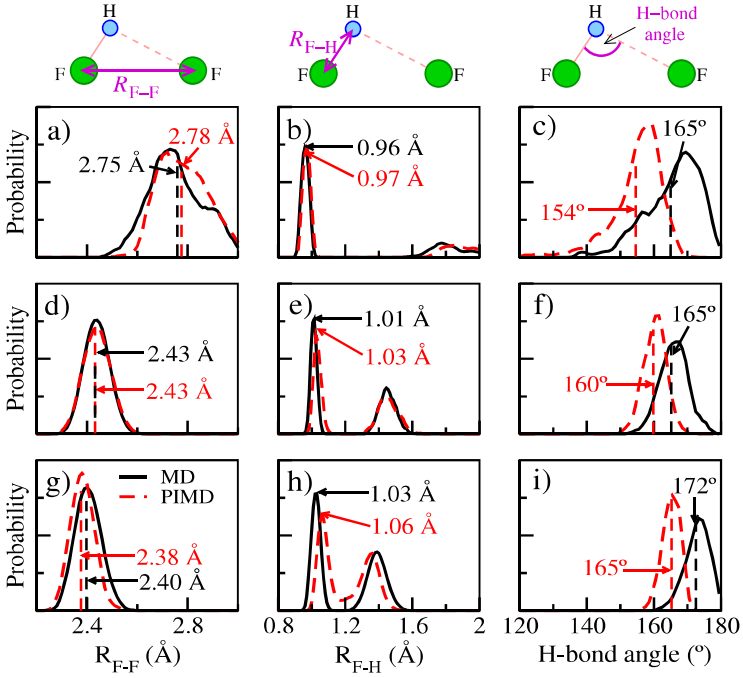

Figure 7.10: HF clusters as examples for detailed analysis of the QNEs. Distributions of the F-F distances (left), the F-H bond lengths (center), and the intermolecular bending (F-H$\cdots$F angle, right) from the MD (solid black lines) and PIMD (dashed red lines) for a selection of systems: the HF dimer (top), the HF tetramer (middle), and the HF pentamer (bottom). The MD and PIMD averages are shown in black and red vertical dashes, respectively.

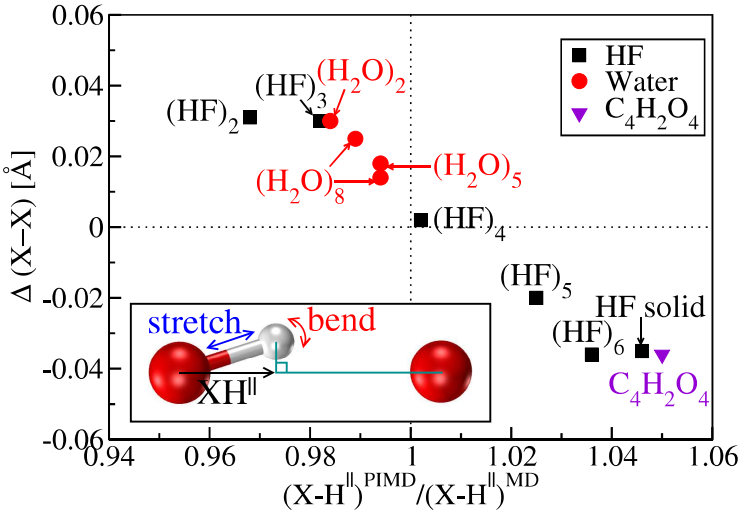

Figure 7.11: A quantification for the competition between the quantum fluctuations on the stretching and bending modes. Differences in average shortest heavy-atom distances between PIMD and MD simulations (Δ(X-X), vertical axis) vs. the ratio of the projection of the donor X-H covalent bond along the intermolecular axis from PIMD and MD simulations (horizontal axis). For the meaning of the labels please refer to the caption of Fig. 7.9. x larger (smaller) than 1 indicates a dominant contribution from the stretching (bending) mode when the QNEs are included. Negative values of Δ(X-X) indicate that quantum nuclear effects decrease the intermolecular separation. An almost linear correlation between the two variables can be observed: When the contribution from stretching becomes more dominant, the QNEs turn from weakening to strengthening the H-bonds. The inset illustrates the geometry used for projecting the donor covalent X-H bond onto the intermolecular axis. The curved red arrow represents the intermolecular bending and the straight blue arrow represents the intramolecular stretching.

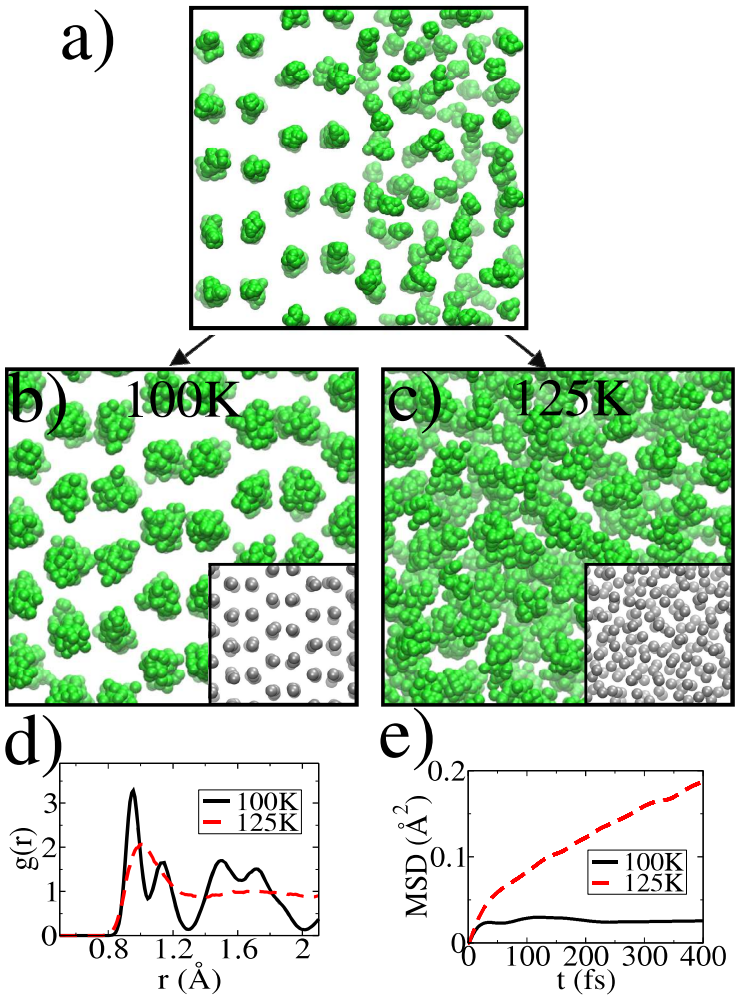

Figure 7.12: *Ab initio* PIMD simulations of solid-liquid coexistence and melting. Snapshots of the PIMD simulations at 700 GPa showing (a) the starting structure, (b) the final state at 100 K and (c) the final state at 125 K. Thirty-two beads (green balls) were used to represent the imaginary-time path integral for each atom. The grey balls in the insets of b) and c) correspond to the centroid of each atom. (d) The angularly averaged pair distribution function $g(r)$ for the same two simulations at 100 and 125 K. At 100 K, the solid state persists (black solid line) as indicated by the relatively sharp peaks. At 125 K (red dashed line), these peaks are much broader and the $g(r)$ is characteristic of a liquid. This is further supported by the data in penal e), where the mean square displacements (MSD) as a function of time from separate adiabatic centroid MD simulations within the path-integral framework are shown. The MSD for the 100 K solid phase saturates rapidly, whereas for the liquid phase at 125 K it rises approximately linearly with time, resulting in a finite diffusion coefficient.

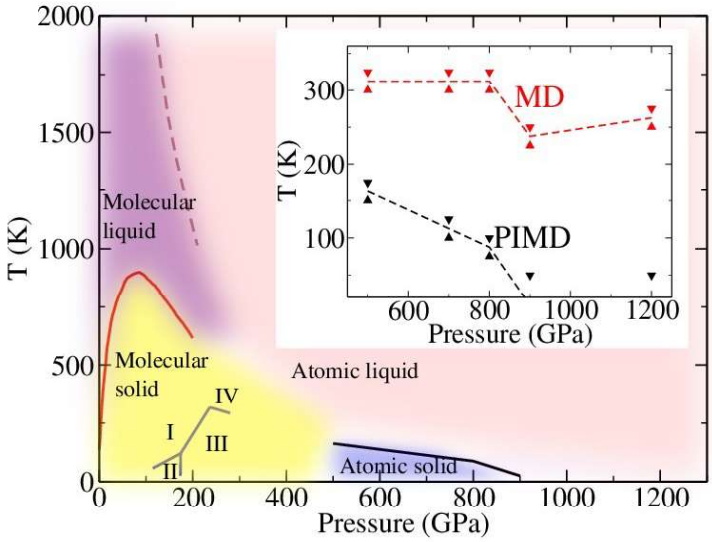

Figure 7.13: Phase diagram of hydrogen and the low-temperature metallic liquid phase. Regions of stability for the molecular solid (yellow), molecular liquid (purple), atomic solid (blue) and atomic liquid (pink) are indicated by the various colours. The dashed line separating the molecular and atomic liquid phases is taken from quantum Monte Carlo calculations [282]. The solid line separating the molecular solid and molecular liquid phases is taken from *ab initio* MD simulations [284], whose negative slope has been confirmed by experiment [436]. The thick black line is the melting curve obtained in this study from the *ab initio* PIMD coexistence simulations. The solid lines separating phases I, II, III and IV are from Refs. [441, 453]. The inset shows how the high-pressure melting curve (dashed lines) are established here. The black and red triangles (inset) correspond to the PIMD and MD results, respectively. The solid up triangles give the highest temperatures for solidification and the solid down triangles show the lowest temperatures for liquefaction. At 900 and 1,200 GPa, the so-called degeneracy temperature is ∼40 K, below which the exchange of nuclei will be important. Accordingly, 50 K was the lowest temperature examined in our PIMD simulations. At this temperature each simulation yields a liquid state, and so the two open triangles at 900 and 1,200 GPa indicate upper bounds for the melting temperature.

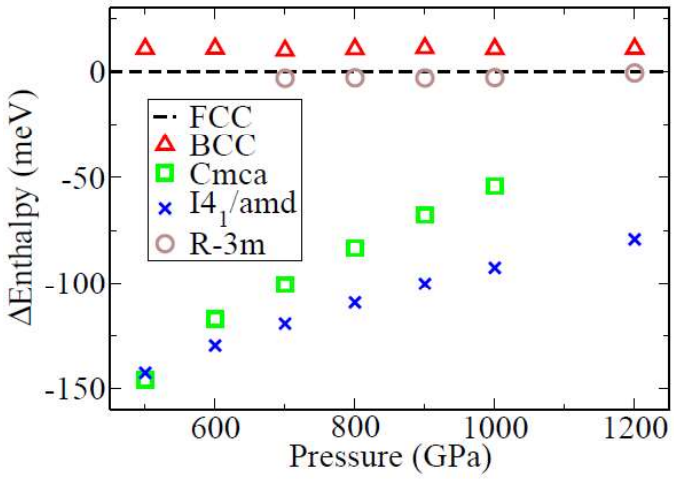

Figure 7.14: Static lattice ground state enthalpies of different crystal structures relative to FCC in solid hydrogen as a function of pressure.

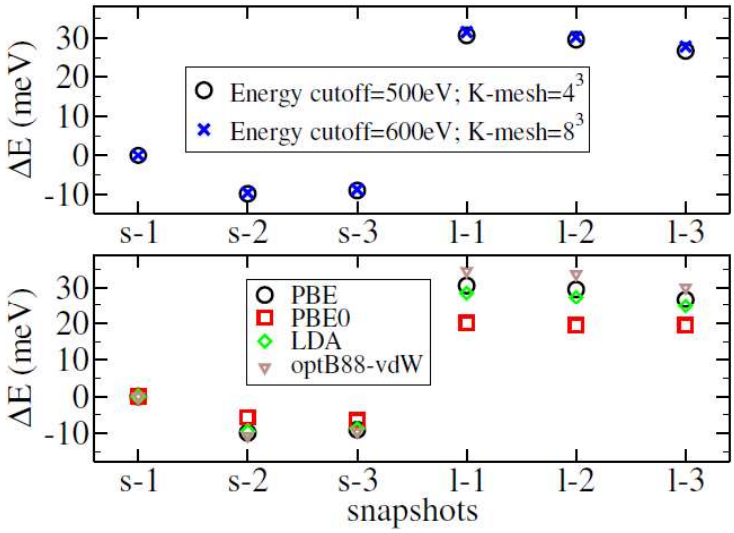

Figure 7.15: Single point total energies of snapshots from the thermalized state of the two-phase PIMD simulations at 700 GPa. The centroid position is used for simplicity. s-1, s-2 and s-3 correspond to snapshots at low temperature (100 K) with hydrogen in the solid $I41/amd$ phase. l-1, l-2 and l-3 correspond to snapshots of the liquid phase at high temperature (150 K).

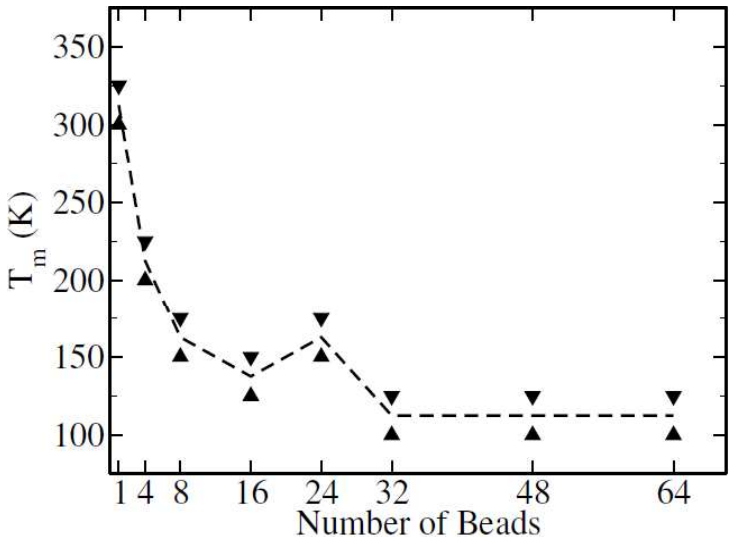

Figure 7.16: Melting temperature calculated at 700 GPa using different numbers of beads. A bead number of one means a MD simulation. The upper and lower limits of the melting temperatures from the two phase simulations are indicated by down and up triangles, respectively. The dashed line indicates the middle of the upper and lower limits.

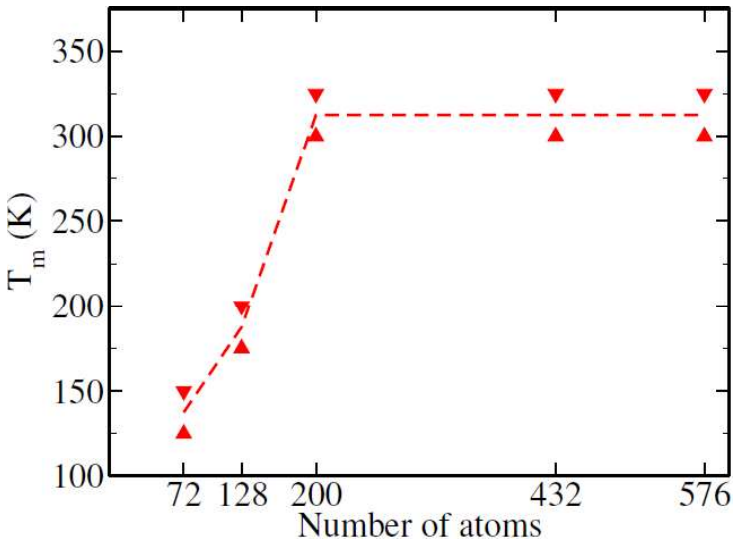

Figure 7.17: Melting temperature calculated at 700 GPa using different number of atoms in the *ab-initio* MD simulations. Upper and lower limit of melting temperature from two phase simulations is plotted with down and up triangles. The dashed line indicates the middle of the upper and lower limit.

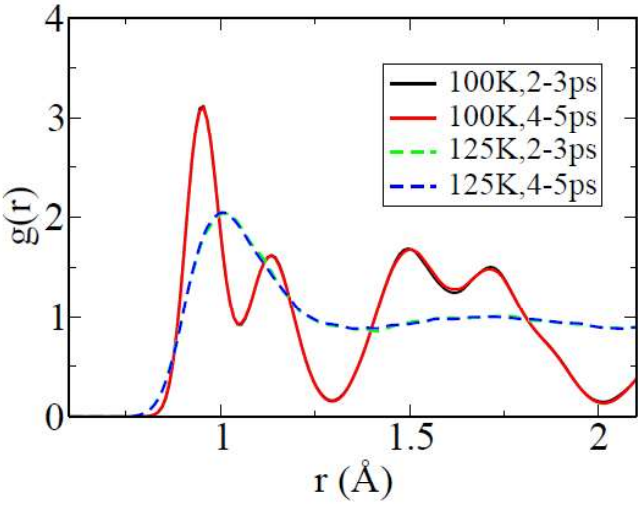

Figure 7.18: The angularly averaged pair-distribution function $g(r)$, as explained above, calculated using different intervals during a two-phase PIMD simulation of hydrogen at 700 GPa and different temperatures. Black (from 2 ps to 3 ps) and red solid (from 4 ps to 5 ps) lines give $g(r)$ from simulation at 100 K when the system solidifies. Green and blue dashed lines are results at 125 K when the hydrogen melts.

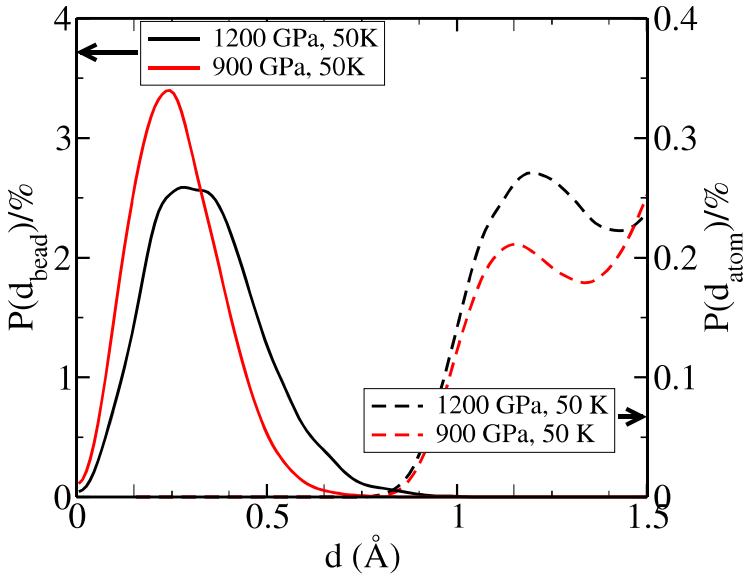

Figure 7.19: Probability distribution of the distances between the first and $N/2+1$ (th) beads in the same atom (solid lines scale on left) and probability distribution of the distances between the first bead in two neighboring atoms of different molecules (dashed lines scale on right). Distributions are reported from a 32 bead two-phase PIMD simulation at 1,200 GPa and 50 K, the highest pressure and lowest temperature case investigated, and for comparison a simulation at 900 GPa and 50 K.

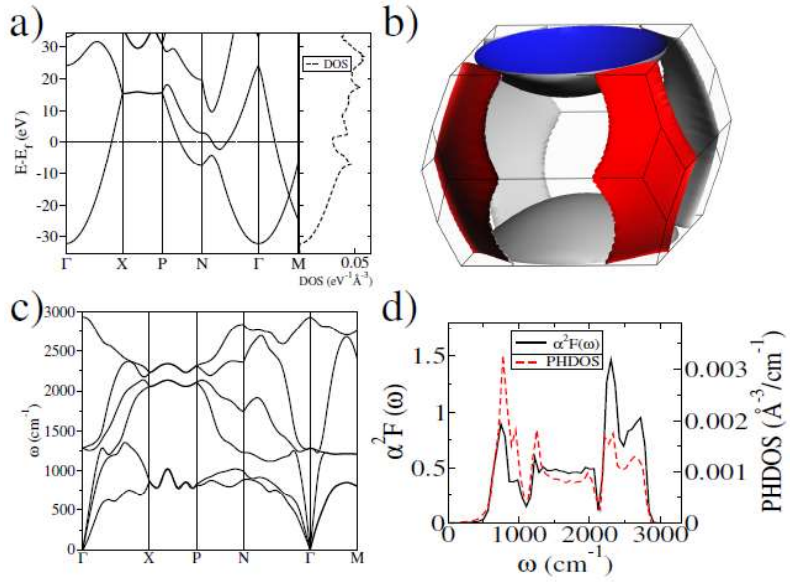

Figure 7.20: Electron and phonon properties of the $I41/amd$ structure of solid hydrogen at 500 GPa, with a volume of 2.28 Å^3 for its primitive cell. a) Electronic band structure and DOS. b) Fermi surface in the Brillouin zone. c) Phonon dispersion curves. d) Phonon DOS (red dashed line) and $\alpha^2F(\omega)$ (black solid line).

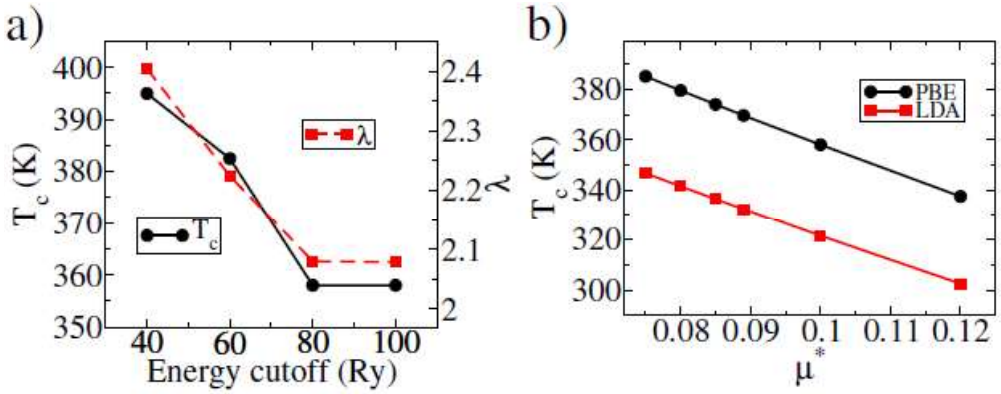

Figure 7.21: Superconductivity of the $I41/amd$ phase at 500 GPa. Panel (a): Superconducting critical temperatures T_c (black circles) and the electron-phonon interaction parameter λ (red squares) as a function of the plane-wave cut-off energy using the PBE functional. Panel (b): Superconducting critical temperatures T_c as a function of the effective Coulomb interaction parameter μ^* using the PBE (black circle) and LDA (red square) functionals.